Nanocrystalline Silicon Solar Cells on Flexible Al Substrates

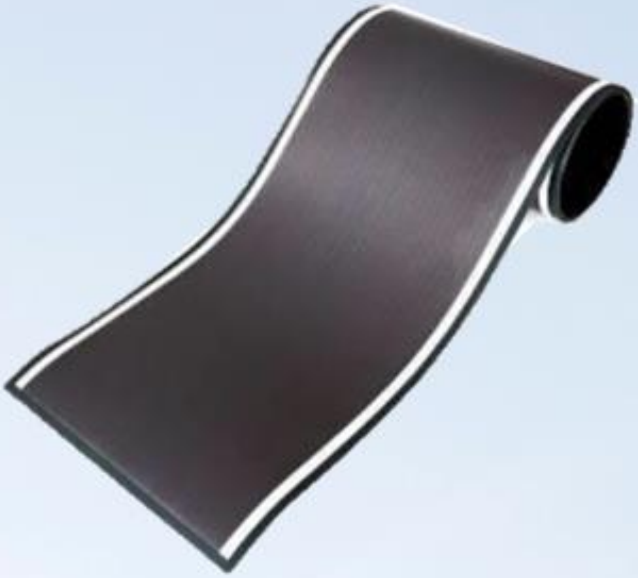

S. B. Nawaratne

May 2020

Nanocrystalline silicon solar cells on flexible Al substrates

The road to FlamingoPV project

By

S. B. Nawaratne

in partial fulfilment of the requirements for the degree of

Master of Science

in Sustainable Energy Technology

at the Delft University of Technology,

to be defended publicly on Thursday, May 28, 2020 at 10:00 AM.

Student Number: 4785126

Thesis committee: Prof. dr. Arno Smets, PVMD, TU Delft
Dr. ir. Rudi Santbergen, PVMD, TU Delft
Dr. ir. Mohamad Niasar, DCE&S, TU Delft
Dr. Gianluca Limodio, PVMD, TU Delft

Cover Image Courtesy: Photo by Who's Denilo ? on Unsplash

Abstract

Thin film solar cell technologies are gaining more favour over first generation PV technologies such as monocrystalline silicon PV modules. This is due to their special characteristics such as lightweight, flexibility and reduced resource consumption. HyET Solar is a Netherlands based company that makes thin film amorphous silicon modules using a novel processing technique. This construction philosophy involves using a temporary Al substrate to deposit the solar cell layers. In the final step a permanent plastic carrier foil is encapsulated, and the Al foil is removed. HyET Solar has partnered with TU Delft under the FlamingoPV project to produce a-Si:H/nc-Si:H tandem solar cells with efficiencies up to 14%.

A starting point for the micromorph cell is a single junction nanocrystalline silicon solar cell on Al foil which has never been attempted at TU Delft. A key concept of cell construction is the use of modulated surface textures (MST) to improve light trapping and growth of high quality nc-Si:H material. MST are optimised on Al foil and used to deposit nc-Si:H layers. The quality of the layers is characterised using various techniques such as Raman spectroscopy, XRD and SEM images. Hydride stretching mode signatures are a non-intrusive way of characterising device grade nc-Si:H layers without undertaking the arduous fabrication process at HyET.

Investigations show the substrate texture features have an influence on the material properties. Results on Al foil show both different and similar trends compared to glass substrates. The silane concentration is an important parameter which influences the nature of deposited material. By tuning this parameter, different signatures of the hydride stretching modes are observed. Initial results suggest that just any seed layer is non-conducive to growth of the nc-Si:H material. Seed layers are deposited using silane concentration grading technique. These graded seeds show excellent microstructure homogeneity and reproducibility. The seed layers also enhance the (220) preferential growth orientation of nanocrystalline grains. The graded seed layers are incorporated into p-i-n cells which will serve as good p-i interface, this resulted in high quality material with good thickness homogeneity and high crystalline fractions over 75%. These cells will expect to perform better in terms of $V_{oc,}$ J_{sc} and FF. Optical simulations show that currents between 25.86 mA/cm^2 and 27.07 mA/cm^2 for 2 μm and 3 μm i-layer thicknesses respectively are achievable using the best MST features combined with HyET's standard cell construction. Further improvements are possible through optimising layer thicknesses and changing the back contact from aluminium to silver.

The nc-Si:H solar cells show high shunt resistance values that are orders of magnitude higher than HyET's modules. This indicates high quality material with limited shunts and cracks which were developed using graded seed layers and MST. When completing the cells at HyET, several challenges were faced due to lack of experience with nc-Si:H solar cells. These include but are not limited to, laser scribing settings and final etching of the Al foil. These issues need to be ironed out at HyET before processing new samples which is out of the control of PVMD. To overcome this bottleneck, an alternate finishing process is researched at TU Delft, despite first results of this alternative approach being unsuccessful, we are confident it can be perfected with more dedicated research.

Acknowledgements

At the time I started my studies at TU Delft, I was not sure about the thesis project I wanted to take. Coming from an electrical engineering background, I always assumed that it will be in the field of Electrical Power. Taking the PV courses opened me to a new world of technologies which was fascinating. I would like to thank firstly, Professor Arno Smets, who is not just a great lecturer but also a nice person to work with, for giving me the opportunity to work on this thesis. I would also like to equally thank my daily supervisor, Dr. Gianluca Limodio, who has been there to listen to my ideas, encourage them and give me the guidance, freedom, and assistance at a moment's notice during the past nine months. Next, I would like to thank fellow master students, Devika Rajagopal and Erik Spaans for collaborating with me on the FlamingoPV project, for sharing their valuable data and ideas which helped me with my own analysis and understanding. A special credit to Martijn Tijssen and all those concerned at EKL for always helping me with the machines and equipment during my cleanroom activities.

I also want to show gratitude to PhD students, Anna Rita for helping me with XRD measurements, Thierry de Vrijer, and his team for sharing valuable information from the DISCO project, and Assistant Professor Rudi Santbergen for assistance with GenPro4. My sincerest thanks go out to HyET Solar, namely, Davide Bartesaghi and Edward Hamers who gave us helpful insights into our results during the routine FlamingoPV meetings, in addition to their unwavering assistance and efforts in completing the cell fabrication and characterisation at HyET Solar.

In addition, there are some other important people I would like to mention, these are; Professor Olindo Isabella for giving me the opportunity to work as a teaching assistant at PV lab, and to Sukanaya, Arturo and Lory who were our pillars of support for PV lab and PIRE courses during our first stint as PV lab TAs.

Finally, I would like to thank all my family and friends who made things enjoyable, and manageable during the last couple of years. I would like to say that undertaking this Masters' degree was a challenge and that it was not easy, since good grades also require certain sacrifices. I hope that with the new knowledge and skills I have gained, I can contribute positively to the working community.

Sajith Nawaratne
Student, Master SET
Delft, May 2020

Table of Contents

List of Figures

List of Tables

Abbreviations

AM	Air mass
APCVD	Atmospheric pressure chemical vapour deposition
AZO	Aluminium doped zinc oxide
BIPV	Building integrated photovoltaics
BoS	Balance of system
BZO	Boron doped zinc oxide
CIGS	Copper indium gallium sulphide
CSS	Close-space sublimation
DOS	Density of states
EDS	Energy-dispersive X-ray spectroscopy
EKL	Else Kooi lab
EVA	Ethylene-vinyl acetate
FLAMINGO	Flexible lightweight advanced materials in next generation of photovoltaics
IR	Infrared
FTO	Fluorine doped tin oxide
FTPS	Fourier-transform photocurrent spectroscopy
FWHM	Full width at half maximum
HRTEM	High resolution transmission electron microscopy
HyET	High yield energy technologies
ITO	Indium tin oxide
LA	Longitudinal acoustic
LCOE	Levelized cost of electricity
MST	Modulated surface textures
MW	Megawatt
MWp	Megawatt peak
PECVD	Plasma enhanced chemical vapour deposition
PV	Photovoltaics
PVMD	Photovoltaic materials and devices
R2R	Roll to roll
RF	Radio frequency
SEM	Scanning electron microscope
SM	Stretching modes
TA	Transverse acoustic
TCO	Transparent conductive oxide
TNO	Toegepast natuurwetenschappelijk onderzoek
TO	Transverse optical
VHF	Very high frequency
VTD	Vapour transport deposition
WP	Work package
XRD	X-ray diffraction

Nomenclature

Ag	Silver	[-]
Al	Aluminium	[-]
a-SiGe:H	Hydrogenated amorphous silicon germanium	[-]
a-Si:H	Hydrogenated amorphous silicon	[-]
c	Speed of light	[m/s]
CdCl	Cadmium chloride	[-]
CdTe	Cadmium teluride	[-]
c-Si	Crystalline silicon	[-]
D	Diffusion coefficient	[m^2/s]
d_i	Intrinsic layer thickness	[µm]
E	Electric field	[V/cm]
$\mathrm{E_c}$	Conduction band energy level	[eV]
$\mathrm{E_{c,mob}}$	Conduction mobility edge	[eV]
$\mathrm{E_v}$	Valence band energy level	[eV]
$\mathrm{E_{v,mob}}$	Valence mobility edge	[eV]
eV	Electron-volt	[-]
F	Flurorine	[-]
FF	Fill factor	[-]
g(E)	Density of states function	[m^{-3}J^{-1}]
$\mathrm{g_v(E)}$	Density of states function in valence band	[m^{-3}J^{-1}]
$\mathrm{g_c(E)}$	Density of states function in conduction band	[m^{-3}J^{-1}]
η	Efficiency	[-]
$\mathrm{H_\alpha}$	Balmer alpha	[-]
HF	Hydrogen fluoride	[-]
I_{mpp}	Current at maximum power point	[A]
i-nc-Si:H	Intrinsic hydrogenated nanocrystalline silicon oxide	[-]
I_{sc}	Short-circuit current	[A]
J_{dark}	Dark current density	[mA/cm^2]
J_{illum}	Illiminated current density	[mA/cm^2]
J_{ph}	Photocurrent density	[mA/cm^2]
$\mathrm{J_{SC}}$	Short-circuit current density	[mA/cm^2]
k_B	Boltzman constant	[J/K]
KOH	Pottasium hydroxide	[-]
kWh	Kilowatt-hour	[-]
L_c	Correlation length	[µm]
L_D	Diffusion length	[µm]
L_n	Drift length of electrons	[µm]
L_p	Drift length of holes	[µm]
λ	Wavelength	[nm]
λ_{laser}	Wavelength of laser	[nm]
λ_{Raman}	Wavelength of reflected light	[nm]
mA	Milliamps	[-]
MHz	Megahertz	[-]
MW	Megawatt	[-]
MWp	Megawatt peak	[-]
n	Idealiy factor	[-]
N_A	Acceptor doping concentration in the p-layer	[cm^{-3}]
NaOH	Sodium hydroxide	[-]

N_D	Donor concentration in the n-layer	[cm^{-3}]
nm	Nanometres	[-]
n-nc-SiO$_x$:H	n-type doped hydrogenated nanocrystalline silicon oxide	[-]
nc-Si:H	Hydrogenated nanocrystalline silicon	[-]
nc-SiO$_x$:H	Hydrogenated nanocrystalline silicon oxide	[-]
N_{db}	Dangling bond density	[cm^{-3}]
n_f	Density of free electrons	[cm^{-3}]
n_i	Intrinsic carrier concentration	[cm^{-3}]
p_f	Density of free holes	[cm^{-3}]
P_{mpp}	Power at maximum power point	[W]
p-nc-SiO$_x$:H	p-type doped hydrogenated nanocrystalline silicon oxide	[-]
q	Elementary charge	[C]
R$_L$	Load resistance	[Ω]
R$_p$	Parallel resistance	[Ω]
R$_s$	Series resistance	[Ω]
S_c	Silane concentration	[%]
sccm	Standard cubic centimetres per minute	[-]
$S_{c,Initial}$	Initial silane concentration	[%]
$S_{c,Final}$	Final silane concenration	[%]
SnO$_2$:F	Fluorine doped tin oxide	[-]
σ$_d$	Dark conductivity	[S/cm]
σ_n^0	Capture cross-section of electrons	[m^2]
σ_p^0	Capture cross-section of holes	[m^2]
σ_{rms}	Root mean square roughness	[nm]
τ	Carrier lifetime	[s]
T	Temperature	[K]
τ^0	Lifetime of holes and electrons	[s]
τ_n^0	Lifetime of electrons	[s]
τ_p^0	Lifetime of holes	[s]
μ	Mobility	[cm^{2}V^{-1}s^{-1}]
μm	Micrometres	[-]
μ^0	Band mobility of holes and electrons	[cm^{2}V^{-1}s^{-1}]
μ_n^0	Band mobility of electrons	[cm^{2}V^{-1}s^{-1}]
μ_p^0	Band mobility of holes	[cm^{2}V^{-1}s^{-1}]
V	Voltage	[V]
v	Speed of wave	[m/s]
V_{bi}	Built-in voltage	[V]
$\bar{v}_{laser}$	Wavenumber of laser	[cm^{-1}]
V_{mpp}	Voltage at maximum power point	[V]
V$_{oc}$	Open-ciruit voltage	[V]
$\bar{v}_{Raman}$	Wavenumber of reflected light	[cm^{-1}]
$v_{th,n}$	Thermal velocity of electrons	[cm/s]
$v_{th,p}$	Thermal velocity of holes	[cm/s]
wt.	Weight	[g]
X$_c$	Crystalline fraction	[%]
ZnO	Zinc oxide	[-]
ZnO:Al	Aluminium doped zinc oxide	[-]

1. Introduction

The global market for photovoltaic technology is on the rise. In 2017, a total capacity of 99.1 GW was installed around the world, which was the same as the total installed capacity up to 2012 [1]. The cost of utility scale solar PV has been rapidly falling since 2010, the levelized cost of electricity (LCOE) in 2018 for the same is 0.085 USD/kWh, allowing PV technologies to compete directly with fossil fuel technologies for energy production [2]. The reduction in costs is partly due to the improvements in the low cost-high yield processing of monocrystalline silicon solar modules that are now dominating the solar PV market. Figure 1 shows the current technologies of PV that are commercially available in the market.

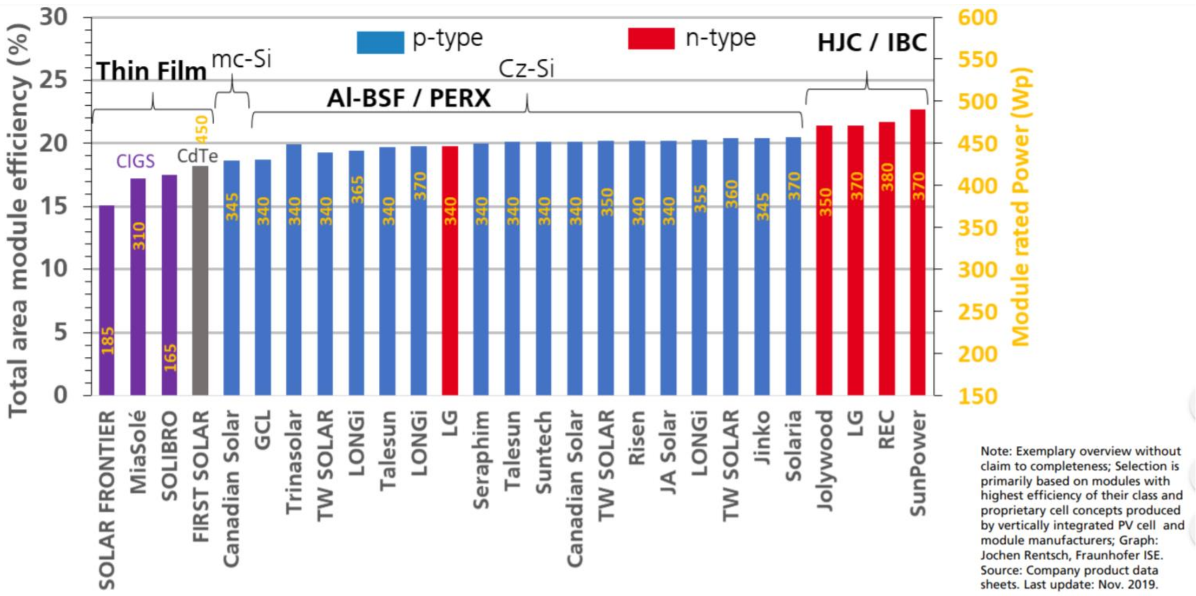

Note: Exemplary overview without claim to completeness; Selection is primarily based on modules with highest efficiency of their class and proprietary cell concepts produced by vertically integrated PV cell and module manufacturers; Graph: Jochen Rentsch, Fraunhofer ISE. Source: Company product data sheets. Last update: Nov. 2019.

***Figure 1**: Prominent commercially available thin film modules and their manufacturers. Adapted from [3].*

1.1 Thin-film solar cells

The main idea behind thin film solar cells is to achieve a reduction in material usage by having very thin layers. Unlike first generation solar cells which have thickness of 100 to 200 µm, thin film materials are in the order of several micrometres; typically, less than 5 µm [4]. The resulting modules consume less material to produce, are lightweight and can be flexible depending on construction philosophy.

Although majority of thin film technologies have lower efficiencies than silicon solar cells, their inherent characteristics allow for advantages over first generation PV technologies [3]. Firstly, thin film devices are made using cheaper and faster processes such as plasma enhanced chemical vapour deposition (PECVD). Secondly, due their aesthetically pleasing nature combined with flexibility, they can be used in special applications such as building integrated photovoltaics (BIPV), for example, use in building facades, windows, roofs, and other large-scale applications such as floating PV farms. Thirdly, thin film PV is less vulnerable to external environmental conditions compared to silicon-based PV modules. The monolithic connected nature of cells allows for more resilience towards shading, leading to less use of bypass diodes. In addition, they have lower performance drop at high temperatures. Finally, the balance of systems (BoS) costs can be kept lower for the same amount of installed capacity as silicon modules by saving on mounting systems and installation costs [5].

1.2 Current technologies of thin film

The most common thin film technologies to date are a-Si:H, cadmium telluride (CdTe) and copper indium gallium selenide (CIGS). All 3 materials have a direct bandgap and absorption coefficients in the order of 10^5 cm^{-1} which allow for thin film applications as shown in Figure 2.

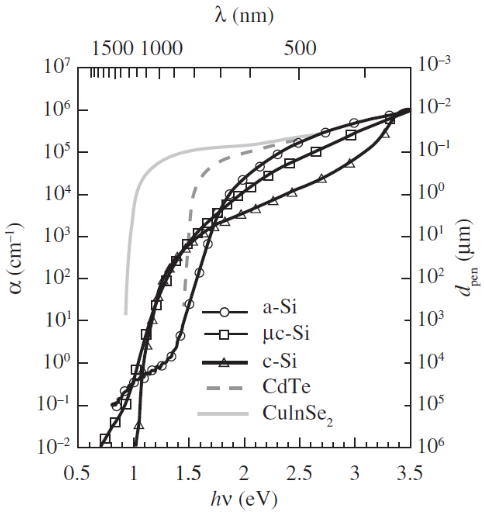

***Figure 2**: Absorption coefficient (α), penetration depth (d_{pen}), as a function of wavelength (λ) and photon energy (hν) of incident light for different thin film materials. Adapted from [6].*

Amorphous silicon seems very promising due to its relatively high absorption coefficient requiring intrinsic layer thicknesses of between 200 nm and 250 nm with the addition of light trapping techniques. They are typically transparent to photons with energies below 1.7 eV and are strong absorbers above 2 eV. As a result, they can produce high open-circuit voltages. However, a:Si:H layers suffer from the Staebler-Wronski effect, where final efficiencies are reduced to 85-90% of initial efficiency due to light induced degradation in the active layers [7]; this effect is still not yet fully understood. They are also widely used in tandem solar cells to reduce spectral utilization losses and achieve higher efficiencies. Common examples include the micromorph tandem cell; a-Si:H/nc-Si:H with efficiencies up to 12.7% and triple junctions such as a-Si:H/nc-Si:H/nc-Si:H with efficiencies up to 14% [8]. At PVMD, quadruple junctions are being developed with a-SiGe:H and c-Si as bottom cells to achieve high V_{oc} and efficiencies.

CIGS solar cells use chalcogen anions from Group 6 of the periodic table. It contains a mixture of copper, indium, gallium, and selenium. By changing the chemical composition, the material can be made to be p or n-type. The solar cell is usually grown on soda lime substrate using 3 stage evaporation. Molybdenum is used as a back contact, followed by the p and n-type CIGS layers. A n-type CdS layer is used to lattice match the n-type CIGS layer to the TCO. The cell structure is shown in Figure 3. Following further developments in processing techniques, Solar Frontier has produced a 1 cm^2 CIGS cell with record efficiency of 23.35% [9].

CdTe is a II-V semiconductor with a zinc blende crystal structure. It can be made either p-type or n-type by doping using impurities. CdTe is deposited in superstrate form on glass substrate. The absorber layer is deposited using close space sublimation (CSS) or vapour transport deposition (VTD). The as deposited CdTe usually has many point defects, extended defects, and un-passivated grain boundaries, which can be reduced by treatment with cadmium chloride (CdCl). A typical CdTe solar cell is shown in Figure 3, the CdS buffer layer is used between the tin oxide window layer and the absorber to reduce series resistance and surface recombination. A molybdenum back contact is used after a buffer layer to improve charge collection. It should be noted that Cd and Te are both rare materials and that Cd is toxic to humans.

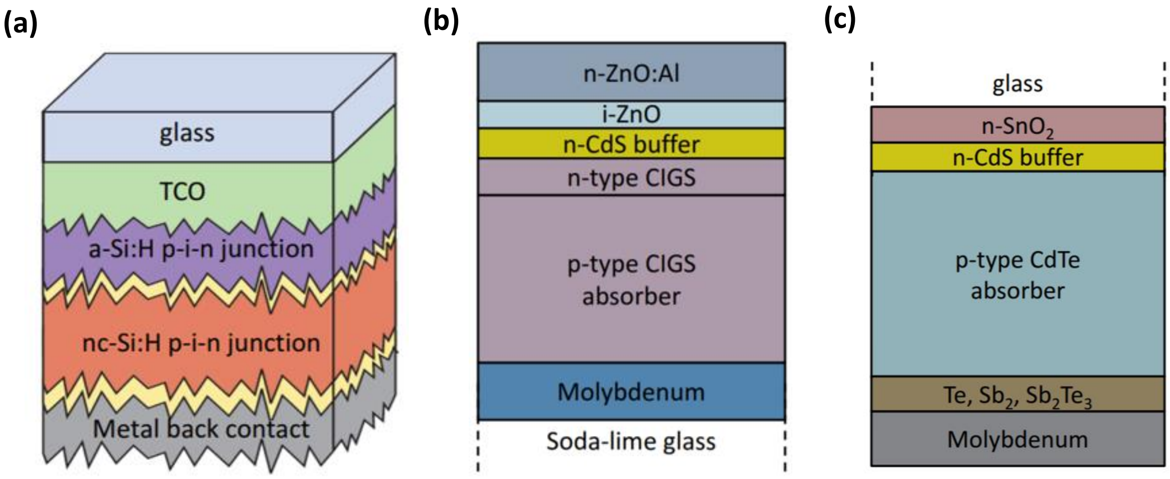

***Figure 3**: Illustrations of some common thin film solar cell stacks (a) Micromorph tandem solar cell, (b) CIGS solar cell, (c) CdTe solar cell. Adapted from [10].*

CIGS and CdTe have the ability to compete with c-Si modules in terms of efficiency. However, global market share of a-Si:H modules is now less than 1%. Despite its challenges, the a-Si:H modules remain viable to a niche market, especially in countries with diffuse light conditions and/or high temperatures, where their output will be less affected. HyET Solar is such a company that caters to this niche market. Its long-term aim is to create a triple junction a-Si:H/nc-Si:H/nc-Si:H module with efficiencies up to 14% using a unique technique that uses an Al foil as a temporary substrate. The inexpensive temporary substrate can be used in large scale roll to roll processing steps and removed in the final step to produce the PV module. This allows HyET to employ a high yield process which is also cost effective.

1.3 FlamingoPV (Flexible lightweight advanced materials in next generation of photovoltaics) project

FlamingoPV is a project undertaken by TU Delft in collaboration with HyET Solar. HyET Solar is a company based in Netherlands that already produces and sells amorphous silicon modules with efficiencies of 7% to a niche market. HyET solar has a unique roll to roll production process whereby it uses Al foil as a temporary substrate to deposit the solar cell layers. They currently have a production capacity of 1 MW/year with plans to expand within and outside the Netherlands. TU Delft, on the other hand has excellent facilities for growing a-Si (amorphous silicon) and nc-Si (nanocrystalline silicon) solar cells at lab scale level at the Else Kooi Laboratory (EKL) under the direction of the PVMD group. A world record initial efficiency of 14.8% was achieved for a-Si/μc-Si tandem cell with an area of 1.1 cm^2 developed at TU Delft. This makes TU Delft a perfect partner for providing the knowledge base behind the development of this type of solar cells.

The aim of FlamingoPV is to increase the efficiency of the PV modules produced at HyET by undertaking lab scale research at TU Delft and then transferring those findings to their largescale roll to roll process. Additionally, there is a need to expand the production scale to 37.5 MWp/year and then to 300 MWp/year in the long term. This undertaking is currently limited by the existing PECVD tool. The deliverables of the project are classified under the following work packages [11]:

WP1 - Lab-scale flexible a-Si:H/nc-Si:H solar cells (5 cm^2) and modules (5x5 cm^2) with stabilized efficiencies of 13%.

WP2 - Roll to roll produced modules of dimensions 30x30 cm^2 with aperture area stabilized efficiency of 12% with 80% production yield.

WP3 - Modules with operating lifetime of over 35 years while maintaining performance above 80% of the initial value.

WP4 - Design of a bottom cell PECVD tool with capital expenditure less than 2 million euro per MWp.

WP5 - Lab-scale flexible triple junction a-Si:H/nc-Si:H/nc-Si:H solar cells (5 cm^2) and modules (5x5 cm^2) with stabilized efficiencies of 14%.

The work reflected in this thesis report falls under the category of WP1, which is in the early phases of FlamingoPV. The lab scale work is undertaken by master students under the supervision of Dr. Gianluca Limodio and Professor Arno Smets. The WP1 involves focusing on optimizing various aspects of the cell, discussed below.

The first one is the Al foil, which is used as a substrate for growing the cell layers. The 10x10 cm^2 Al foils are supplied by HyET solar to TU Delft for carrying out experiments. The aim is to use novel modulated surface texturing (MST) technique to increase cell performance to improve light trapping and enhance growth of high-quality silicon layers. The MST are created by micro-texturing the Al foil using a printing mould or by etching with different chemicals. In the next step, the transparent conductive oxide (TCO) is deposited which adopts the micro-sized features of the substrate. In addition, the TCO is naturally nanotextured at the surface. This combination of nano-sized and micro-sized features forms the modulated surface textures.

The second is the implementation of a double p-layer. The p-layer has many functions, such as; (i) to act as a hole collecting layer and a barrier for electrons, (ii) to be highly transparent to reduce parasitic absorption losses, (iii) facilitate electron-hole recombination at the TCO/p-layer without any electrical losses and, (iv) facilitate refractive index grading to reduce reflection losses at the surface. Since HyET employs only a single p-layer at present, there is a compromise between all the above functions, therefore introducing a second p-layer would allow use of dedicated functions and improved performance. A combination of silicon carbide and silicon oxide is being experimented as double p-layers.

The third is the improvement in the back contact. The conventional back layers consist of n-doped nc-SiO_x:H, ZnO and Al layer. It has been shown from previous studies at TU Delft that switching to Ag as a back contact will lead to improved back reflectance and thus require a thinner i-layer for the bottom nc-Si:H cell. After this stage, the optimization of the thicknesses of the i-layer, n-layer, back TCO and back contact is again necessary.

The final task of WP1 is the successful integration of the above features into the a-Si:H/nc-Si:H tandem solar cell and optimization of the top and bottom cell to achieve the targeted stabilized efficiency of 13%.

1.4 Roll to roll (R2R) process at HyET Solar

HyET uses a unique R2R production process for creating thin, lightweight, and flexible PV modules as shown in Figure 4. The technology was developed by the Helianthos consortium consisting of Akzo Nobel, Delft University, Eindhoven University, Utrecht University and TNO [12]. The company was then bought by HyET Solar to undertake further development and expansion.

The use of Al foil as a temporary substrate facilitates the roll to roll process, whereby the foil passes through several deposition chambers with controlled parameters and the active layers are homogeneously deposited. This process is mostly automated and can be used to create a large number of modules by simply feeding in new Al rolls.

Figure 4*: A look at HyET's finished a-Si:H module which is commercially available [13].*

Figure 5 depicts the entire R2R process. In Step 1, the front TCO is deposited by atmospheric pressure chemical vapor deposition (APCVD) at high temperatures between 500°C and 550°C. The Al foil is designed to withstand these high temperatures which facilitate high deposition rates of up to 100 nm/s with homogenous deposition. The resulting TCO has high opto-electrical properties. Fluorine doped tin oxide (SnO_2:F) is preferred as the TCO compared to aluminium doped zinc oxide (ZnO:Al) because it can better withstand corrosion from moisture and acids. This is because unlike crystalline silicon modules which are encapsulated by glass, these thin film modules are covered by a thin polymer (plastic) encapsulant that is more susceptible to outside environment. After depositing the TCO, the active p-i-n layers are deposited in superstrate form using RF PECVD of 13.5 MHz and substrate temperature of 200°C [14].

In Step 2, laser scribes are done to define the cell area, labelled P1s and P2s. This is followed by insertion of a TCO fill ink at P1s in Step 3 to insulate the active layers. In Step 4, a lift-off ink is dispensed at P3f, the purpose of which is to reduce the number of laser scribes in the overall process. In step 5, the back contact comprising of ZnO:Al/Al is sputtered in a roll to roll DC magnetron sputter system [14]. In step 6, the filler ink is removed to isolate the back contacts. In step 7, the plastic carrier foil is laminated on to back contact side using an adhesive and mechanical press, this is followed by wet chemical etching of the temporary Al foil substrate. The plastic foil now becomes the permanent carrier in the R2R process. In the final step, a polymer encapsulation is made at the top, followed by creation of the busbar connections to create the final product.

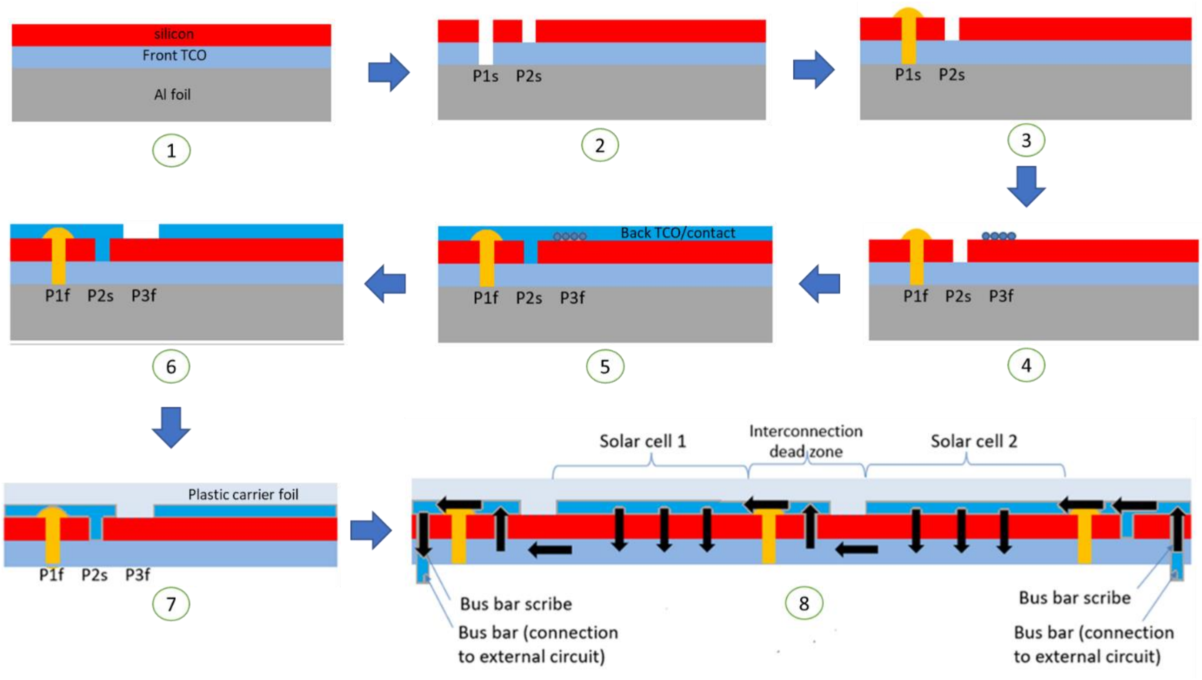

***Figure 5**: Main steps involved in roll to roll production process implemented at HyET Solar. Adapted from [15].*

2 Aim and outline of thesis

The goal of this thesis is to grow nanocrystalline silicon material on a flexible Al substrate for the first time. This paves the way towards the application of this research in HyET Solar's large-scale roll to roll process for fabricating future tandem and triple junction solar cells as per WP1 of the FlamingoPV project. Before moving on to the tandem solar cells, first it is important to understand and characterise the growth on single junction nc-Si:H solar cells. Some of the important research questions that will be answered are:

- Is it possible to apply the concept of modulated surface textures to Al foils similar to using glass substrates?
- What factors influence the growth of nc-Si:H material on Al foil using MST, and to what extent are they similar to glass substrates?
- What are the factors which influence the growth of high quality nc-Si:H material on Al foils, and how can they be characterised without going through the arduous fabrication process at HyET Solar?
- How will the fabrication of nc-Si:H solar cells differ from the a-Si:H solar cells which HyET Solar is currently accustomed to?
- Is it possible to make p-i-n nc-Si:H solar cells using temporary flexible Al foils with efficiencies comparable to that on glass substrates?

It should be noted that since we are growing nc-Si:H solar cells on Al foil for the first time, this thesis report can be viewed as a journey of discovery in which we are trying to best understand the nature of the material so that it can be reproduced and transferred to the large scale roll to roll process at HyET.

The report starts with a brief introduction to thin film technologies and an overview of the unique roll to roll processing technique at HyET Solar and novel concept of using temporary Al foils to grow thin film silicon solar cells. Chapter 3 focuses on the theory of thin film solar cells, specifically p-i-n type nc-Si:H cells which have slightly different underlying principles compared to conventional p-n junction crystalline silicon cells. It also discusses the nature of nanocrystalline material and its suitability for thin film solar cells. In addition, some key concepts used in this thesis are discussed. In Chapter 4, the experimental methods are discussed in detail. These are basically the apparatus and equipment that is used to deposit the layers, and characterisation tools available to determine and analyse the nature of the material. In addition to how the tools work, some theory that is relevant to the analysis is also discussed. Chapter 5 is split into two sections; the first section involves work undertaken at TU Delft. This entails all the experiments carried out from the initial growth and characterisation to perfecting the high quality nc-Si:H on Al foil. The latter half of the chapter focuses on analysis of the cells completed at HyET, namely, the laser scribing, lamination and removing of the Al foil. Chapter 6 summarises and concludes the findings of this thesis and finally, Chapter 7 hints at some interesting and exciting propositions for further improving nc-Si:H solar cells.

3 Theory of thin film solar cells

The fundamental principle behind the operation of all solar cells remain the same. Solar cells consist of photoactive layers which absorb sunlight to produce electricity. The solar spectrum consists of photons with wavelengths between 250 nm and 2500 nm corresponding to photon energies approximately between 5 eV and 0.5 eV. The solar spectrum used for solar cell testing is AM1.5G which means “air mass 1.5 global”. This signifies that the solar irradiation travels 1.5 times the optical length of the earth’s atmosphere compared to if light was incident from the zenith (AM1), or in other words an angle 48.2° from the zenith as depicted in Figure 6.

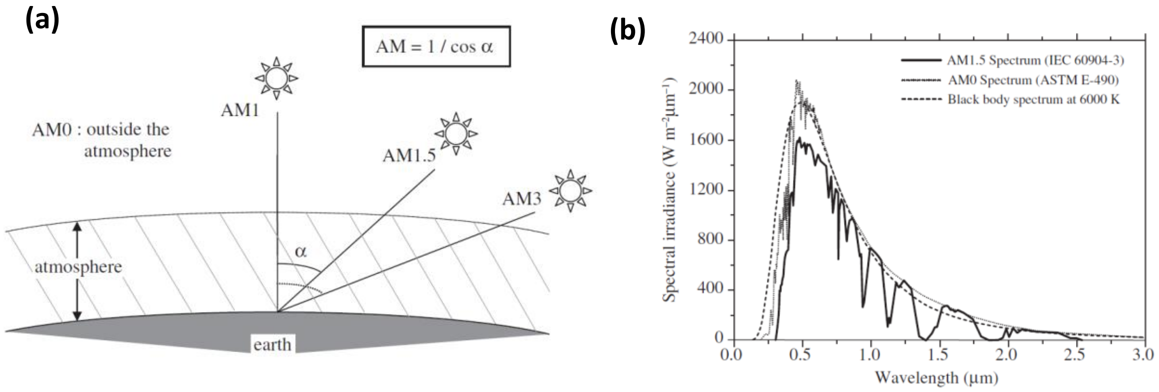

***Figure 6**: (a) Illustration of incidence angles of AM0, AM1, AM1.5 spectrum, (b) The spectrum is defined as the variation of spectral power density with wavelength. Adapted from [6].*

3.1 Working principle of a thin film solar cell

The material of the photoactive layer is usually a semiconductor with a defined bandgap. The bandgap is the difference in energy levels between the conduction and the valence band, measured in eV. It is the energy that an incident photon should possess to create an electron-hole pair. This is depicted in Figure 7(a) where the electron jumps from valence band to conduction band, thereby creating a hole where the electron used to occupy. The movement of electrons also create a movement of holes, which is defined as current. However, the energy of the electrons do not last forever and they quickly recombine with the hole (in Figure 7(c)).

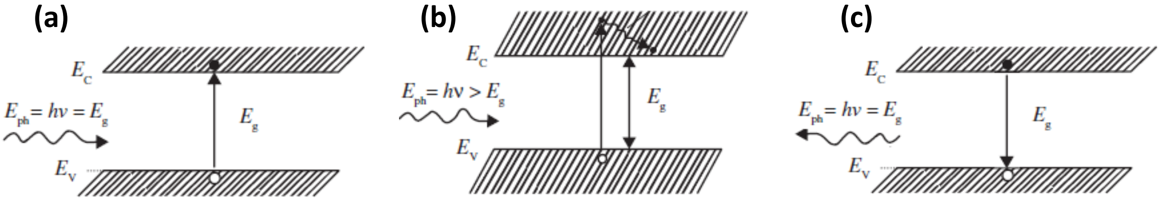

***Figure 7**:Charge carrier generation and recombination, E_c refers to conduction band and E_v refers to valence band, (a) Photon energy equal to bandgap is absorbed to create an electron-hole pair, (b) Photon energy greater than bandgap results in excess energy that is released as heat, (c) Radiative recombination; if electrons and holes are not separated they recombine to release a photon. Adapted from [6].*

The distance charge carriers can travel before recombining is a function of the carrier lifetime and carrier mobility. The carrier lifetime (τ) is the time that the charge carrier is free to move around before recombining, and mobility (μ) is a measure of how easy it is for the charge carries to move around inside a semiconductor. A summary of mobilities in silicon materials is shown in Table 1.

***Table 1**: Mobility values for silicon based solar cells given in cm^2/Vs [6].*

Mobility	c-Si	a-Si:H	nc-Si:H
Electrons	1360	1 to 10	1 to 10
Holes	450	0.2 to 2	0.3 to 3

For crystalline silicon materials, the diffusion length (L_D) is defined, which is calculated independently for holes or electrons using $L_D = \sqrt{\tau \times D}$, where τ is the minority carrier lifetime and D is the diffusion coefficient (which is a function of mobility). It is the distance a charge carrier can travel before recombining. Therefore, the solar cell thicknesses are limited to below the diffusion lengths.

In c-Si solar cells, a p-n junction is created by doping, for example an n-type wafer can be p-type doped using ion implantation. At the junction, a built-in electric field is formed due to abrupt changing of doping concentrations. The p and n regions absorb light to produce excess electrons and holes, respectively. The excess carriers diffuse towards the junction, where they are separated by the electric field. The electrons are collected at the n-side and holes are collected at the p-side.

In thin film silicon solar cells, because of higher defect densities in doped layers, the diffusion length is insufficient to ensure charge carrier collection even at thicknesses of 1 µm. It can be seen from Table 1 that the hole and electron mobilities in thin film silicon is 4 orders of magnitude lower than crystalline silicon. To overcome this, an intrinsic or impurity-free layer (i-layer) is sandwiched between very thin p and n doped layers. This results in an electric field (E) that extends across the i-layer. The i-layer acts as the photogeneration layer and charge carriers are separated due to the electric field within the i-layer. The main transport mechanism in thin film silicon is therefore drift, the drift length of electrons (L_n) and holes (L_p) is given by:

$$L_n = \mu_n^0 \times \tau_n^0 \times E \text{ and } L_p = \mu_p^0 \times \tau_p^0 \times E \tag{3.1}$$

$where$

$\mu_n^0, \mu_p^0 - band\ mobility\ of\ electrons\ and\ holes\ respectively$
$\tau_n^0, \tau_p^0 - lifetime\ of\ electrons\ and\ holes\ respectively$

It has been shown that $\mu_n^0 \tau_n^0 = \mu_p^0 \tau_p^0$ for a-Si:H and nc-Si:H layers [6]. Therefore, the drift lengths become:

$$L_n = L_p = \mu^0 \times \tau^0 \times E \tag{3.2}$$

For charge carriers to be separated, the drift lengths must be greater than the i-layer thickness at short circuit and maximum power conditions [6]. The drift length and the electric field are difficult to measure; but are dependent on the quality of the i-layer and density of dangling bonds. The dangling bond density can be measured using Fourier transform photocurrent spectroscopy (FTPS). Therefore, by having a high-quality intrinsic layer with minimum impurities, a high enough drift length can be maintained in the final cell.

The distribution of the electric field inside a p-i-n nc-Si:H solar cell can be found if the distribution of the doping concentration is known, albeit impossible [6]. Figure 8 shows how the electric field is formed in a p-i-n cell. Figure 8(b) shows a simplified doping distribution in the p and n layer. It is important to note that doping in nc-Si:H is unclear due to non-homogeneous material properties due to an amorphous/nanocrystalline mixed phase growth which is not well quantified [6].

Once the p-i-n stack is complete, the excess holes in the p-type diffuse to the n-type and the excess electrons from n-type move towards p-type due to the diffusion gradients. This creates a region depleted of charge carriers with a net negative charge in the p-type and a net positive charge in the n-type. The depletion region increases until the force of the electric field counters the diffusion process. The depletion region of the p-i-n junctions extend to edges of the p and n layer since they are very thin in the order of nanometres [6]. This is unlike in c-Si p-n junctions where the depletion region forms a very small fraction of the doped layer thickness.

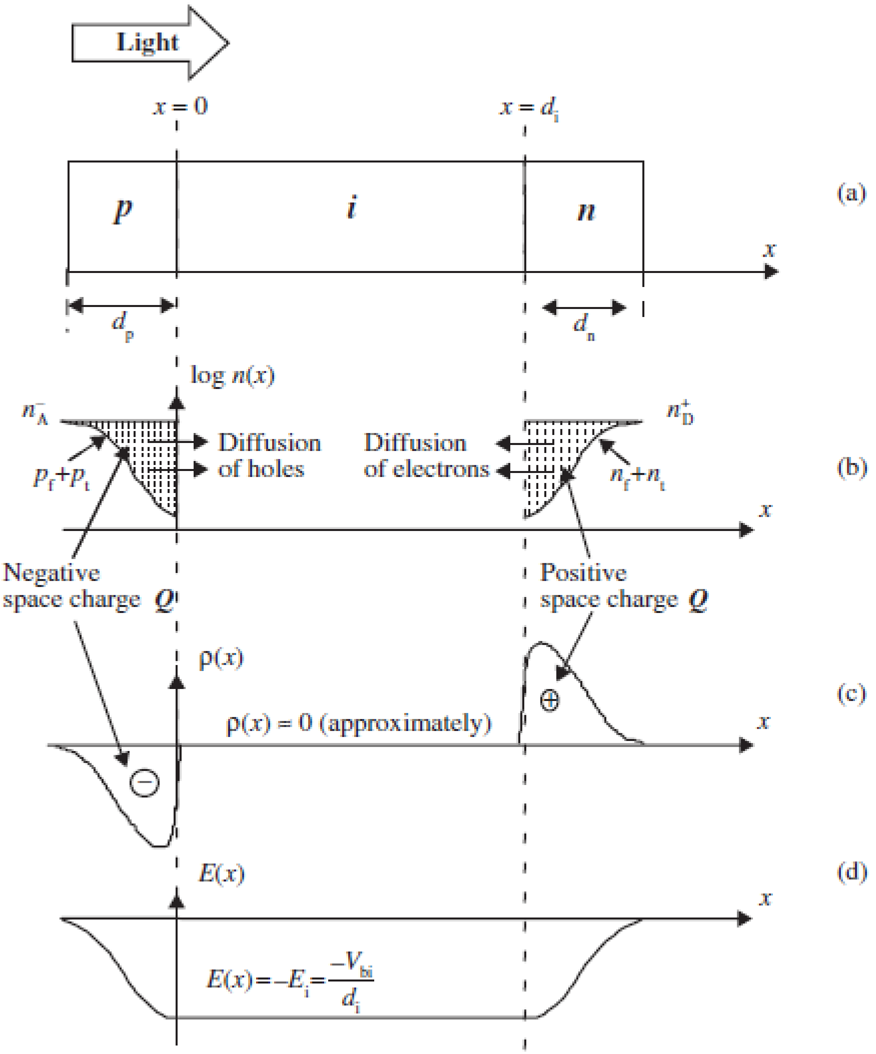

Figure 8: Formation of electric field in p-i-n solar cell. Adapted from [6].

The electric field distribution is shown in Figure 8(d), it is given by; $E = \frac{V_{bi}}{d_i}$, where V_{bi} is the built-in voltage and d_i is the intrinsic layer thickness. If we assume that that the doping concentration in the p and n layer are constant and given by N_A and N_D respectively, then the built-in voltage is given by:

$$V_{bi} = \frac{k_B T}{q} ln\left(\frac{N_A N_D}{n_i^2}\right) \tag{3.3}$$

This can be used to estimate the maximum electric field strength in the p-i-n cell. It is important to note that the p and n layer thicknesses should be sufficiently large enough that the depletion width can be accommodated. p-layers are required to be thin as possible to reduce parasitic absorption, however, a thickness below the minimum value could cause the electric field and the V_{oc} to suffer [6].

3.2 Substrate-p, p-i and i-n interfaces

Th quality of the p-i interface is critical to maintain a high-quality solar cell. While deposition using PECVD, the ions in the plasma bombard the surface of p-layer setting boron atoms free to diffuse into the i-layer. The boron atoms act as impurities and increase defects. The same will happen when depositing the p-layer on the TCO/Al substrate as they contain foreign elements such as Al or F. Al being an p-type dopant will influence the effective acceptor concentration in the p-layer. When depositing the n-layer, phosphorous back diffusion may occur into the i-layer again increasing the number of defects.

The impurities act as dangling bonds or recombination centres for photogenerated charge carriers, which lead to a reduction in the photogenerated current and lower the solar cell performance. The impact of the p-i and i-n interface is more critical on nc-Si:H cells because it is important to have a good initial growth of nano-crystallites following an amorphous incubation layer; having impurities in this layer can deteriorate the growth and reduce the quality of this interface. Secondly, hydrogen is also involved in the formation of nc-Si:H, the existence of multiple hydrogen bonds with a single silicon lead to further degradation of the layers as discussed in section 4.5 and 4.6. Defective p and n layers result in a higher recombination where the excess minority carrier concentrations are reduced. This means that the splitting of the quasi fermi energy levels is lowered, which also leads to a lower V_{oc}.

In summary, the depositions need to be carefully controlled by using suitable parameters for frequency, power, pressure, and gas flows in the PECVD chamber to make sure that the plasma bombardment is not aggressive.

3.3 Recombination mechanisms

Recombination in the intrinsic layer is mainly due to defects caused by dangling bonds. The dangling bonds trap either holes or electrons and remain as recombination centres. This type of recombination is called Shockley-Read-Hall recombination and given by:

$$R = \frac{n_f}{\tau_n^0} + \frac{p_f}{\tau_p^0} \tag{3.4}$$

Where $n_f \; and \; p_f$ are the density of free electrons and free holes and $\tau_n^0 \; and \; \tau_p^0$ are the capture times by dangling bonds for electrons and holes respectively, given by:

$$\tau_n^0 = \frac{1}{v_{th,n}\sigma_n^0 N_{db}} \; and \; \tau_p^0 = \frac{1}{v_{th,p}\sigma_p^0 N_{db}} \tag{3.5}$$

Where $v_{th,n(p)}$ – thermal velocity of electrons (holes), $\sigma_{n(p)}^0$ – capture cross section of electrons (holes) and N_{db} is the dangling bond density.

The thermal velocity of electrons is about 1 to 3 times higher than for holes and therefore more likely to be captured, and the capture cross section determines the effectiveness of the dangling bond to trap the charge carrier. Figure 9 shows the distribution of dangling bonds with position in a p-i-n cell, a bad p-i interface can lead to high unwanted recombination.

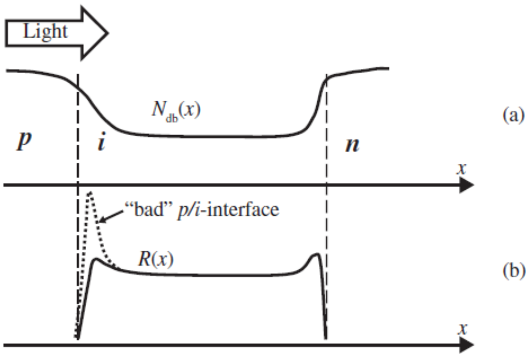

Figure 9*: (a) The distribution of dangling bonds in the p-i-n cell, the density is highest at the interfaces, (b) The effect of a bad p-i interface on recombination. Adapted from [6].*

3.4 The p-i-n junction under illumination

A classical p-n junction solar cell is characterized by the equation:

$$J_{illum} = J_{ph} - J_{dark} \tag{3.6}$$

Where

$$J_{dark} = J_0 \left[exp\left(\frac{qV}{nk_BT} \right) - 1 \right] \tag{3.7}$$

corresponds to the current in a diode under no illumination, and J_0 is the reverse saturation current density, n is the diode ideality factor and V is the applied voltage.

Under illumination, a photogenerated current J_{ph} is superimposed in opposite direction to the diode current as shown by the J-V curve in Figure 10 below.

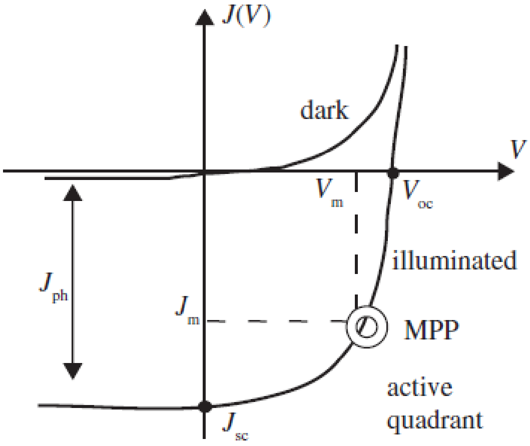

Figure 10*: The illuminated J-V characteristics are superimposed on the dark J-V characteristics. Adapted from [6].*

The equivalent circuit for the solar cell is shown in Figure 11. The series resistance is denoted by R_s and shunt resistance by R_p. The series resistance is due to bulk resistance against flow of current inside the semiconductor and metal contacts, and due to semiconductor-metal interfaces.

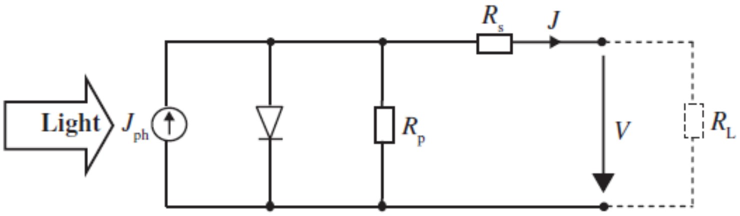

Figure 11: Equivalent circuit for a p-n junction solar cell

The shunt resistance is due to current leakage across edges of the material, aggravated by defects and impurities in the junction [7]. It is important to keep R_s low and R_p high to maintain a high-quality solar cell.

The general equation 3.6, does not necessarily apply to the p-i-n junction due to the existence of an i-layer. The recombination in the i-layer acts as a current sink, reducing the overall photogenerated current. An increase in photogenerated current is due to an increase of minority carriers which will result in a higher recombination rate according to equation 3.4. Taking this into account, the equation 3.6 becomes:

$$J_{illum} = J_{ph} - J_{dark} - J_{rec} \tag{3.8}$$

The recombination current in the i-layer (J_{rec}) can be calculated in a simple approximation using the equation below:

$$J_{rec} = J_{ph} \frac{d_i}{l_{drift}} \tag{3.9}$$

where,

$$l_{drift} = \mu^0 \tau^0 E \tag{3.10}$$

and

$$E = (V_{bi} - V)/d_i \tag{3.11}$$

In equation 3.11, it is assumed that the electric field is constant throughout the entire i-layer but in reality, it is not the case. From equation 3.10 and 3.11 we see that with increasing voltage (V), the value of E and l_{drift} decreases. According to equation 3.9, J_{rec} becomes a larger fraction of J_{ph}. Due to this phenomenon, the J-V curve for p-i-n cells look as in Figure 12 where all the curves at different light intensities intersect at a common point, unlike in the case of c-Si solar cells.

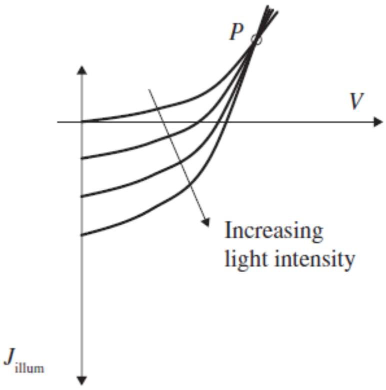

Figure 12*: J-V characteristics of a typical p-i-n cell illuminated with four different intensities show a common intersection point. This phenomenon is typically observed in p-i-n or n-i-p based thin film silicon solar cells. Adapted from [6].*

The equivalent circuit of a nc-Si:H, p-i-n cell is shown in Figure 13, where the effect of the additional recombination effect is shown by J_{rec}. For nc-Si:H cell, the diode can be characterized by an ideality factor (n) between 1.5 and 1.8 where recombination is dominant in the i-layer and between 1.5 and 1.6 for recombination dominant at the p-i and i-n interfaces [6].

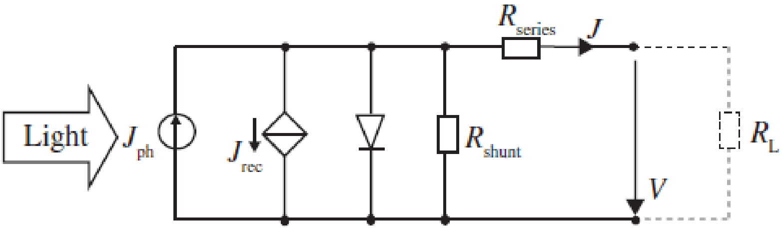

Figure 13*: Complete equivalent circuit of a p-i-n or n-i-p thin film silicon solar cell. Adapted from [6].*

3.5 Material properties of nanocrystalline silicon solar cells

To understand the nature of nanocrystalline silicon and amorphous silicon, first we must look at the structure of crystalline silicon (c-Si). c-Si can be either mono-crystalline or multi-crystalline depending on the arrangement of Si atoms in the lattice structure. Mono-crystalline silicon consists of a repeating structure whereby each Si atom is bonded to four other atoms in a tetrahedral structure. The mono-c-Si is grown using Czochralski or float-zone process whereby high-quality Si wafers can be produced. Cheaper but lower quality wafers can be produced using a casting process to form multi-crystalline silicon where grain boundaries are prominent in its structure. The grain boundaries result in dislocations in the lattice structure leading to increased defects and poor performance in the open-circuit voltage. One of the main advantages of mono c-Si over multi c-Si is higher efficiencies and lower temperature coefficient of power; allowing it to perform better in hot climates.

The c-Si forms an indirect bandgap of 1.12 eV, because both a change in momentum and energy is required to excite an electron from the valence band to conduction band. Because of this, c-Si has a low absorption coefficient for incident photons from around 400 nm and upwards [7]. A consequence of a low absorption coefficient is the need to allow the light to penetrate further into the Si wafer so that photons are absorbed to produce electron-hole pairs. Therefore, in theory a thick wafer of at least 230 µm is required to absorb 90% of the incident light [7]. However, in practice this thickness can be reduced by introducing texturing features to increase the optical path length of light inside the wafer.

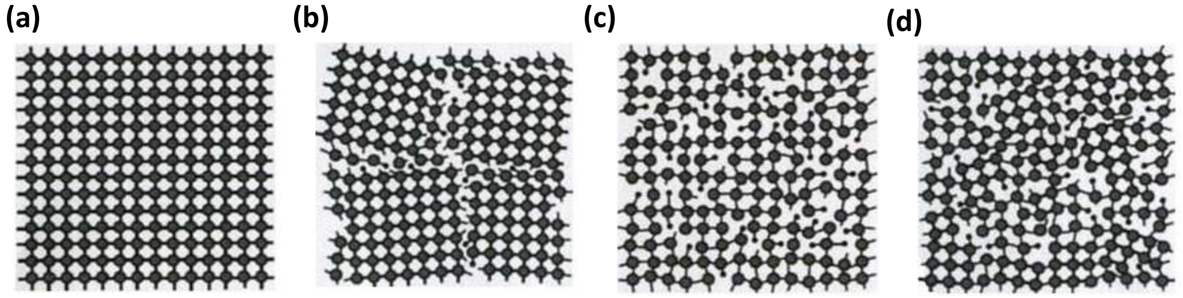

Figure 14: Arrangement of silicon atoms in (a) monocrystalline silicon, where each Si atom is bonded to four other Si atoms, (b) multicrystalline where grain boudaries disrupt the perfect tectrahedral arrangement (c) amorphous silicon which exhibits a disordered Si-Si bonding with many dangling bonds pasivated by hydrogen, (d) nanocrystalline silicon exhibits a mixed phase of nano-sized crystalline grains passivated by hydrogen and amorphous silicon at the grain boudaries. Adapted from [16].

Another approach to growing silicon is by using a mixture of gasses consisting of hydrogen (H_2) and silane (SiH_4). The gasses are dissociated into free radicals in a plasma chamber, which are then deposited on a substrate. This process is called plasma enhanced chemical vapor deposition (PECVD) and is explained in more detail in section 4.1. Unlike in the Czochralski or float-zone process, the Si atoms are not deposited in a perfect tetrahedral structure. The bond lengths and bond angles vary and not all Si atoms are bonded to each other. This structure is defined as amorphous silicon, they exhibit no long-range order (disordered) structure with many dangling bonds or defects. The defects need to be passivated using hydrogen before being used in solar cell applications (a-Si:H). Even with passivation, there is still a large number of defects compared to mono- or multi c-Si.

The density of states (DOS) is a measure of the density of allowed energy levels for electrons in the conduction band and holes in the valence band. The DOS are present only in the conduction band and valence band of c-Si and non-existent in the band gap. In a-Si:H, due to the defects such as divacancies, multi-vacancies and nanosized voids[7], trap states exist in the band gap and as a result the DOS extend into bandgap. These are called band tails or Urbach tails as shown in Figure 15. In addition, the momentum is poorly defined which makes a-Si:H a direct bandgap material between 1.6 and 1.8 eV depending on the hydrogen content. As a consequence, the absorption coefficient for a-Si:H is orders of magnitude higher than for c-Si when comparing as shown in Figure 2.

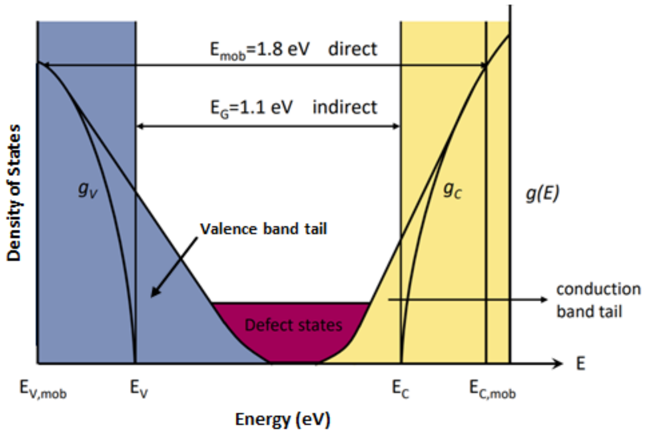

Figure 15: Crystalline silicon exhibits density of states only within the band gaps, whereas for amorphous silicon, the density of states extended into the band gap due to various defects. The bandgap is defined by the mobility gap in a-Si:H. Adapted from [10].

By increasing the hydrogen to silane ratio (H_2/ [SiH_4 + H_2]) in the PECVD chamber, the amorphous material transitions into microcrystalline silicon following an incubation layer as shown in Figure 16.

The microcrystalline is characterized by nano-sized crystallites, grain boundaries and amorphous tissue. The crystallites are formed during the nucleation phase and continue to grow in a columnar orientation until a saturated crystalline fraction is reached. This fraction increases with increased hydrogen ratio and is also related to the quality of the nc-Si:H. The incubation phase and crystallization phases are important in forming the optoelectronic properties of the material [17]. In nc-Si:H, both the amorphous tissue and crystalline part contribute to optical absorption and it is unclear how the transport mechanism takes place, i.e. through the amorphous tissue or through the interconnection of crystallites, or both.

Grain boundaries are detrimental to performance of nc-Si:H solar cells. Too many grain boundaries allow impurities such as oxygen to infiltrate acting as an n-type dopant, thus making the material more n-type at higher crystalline fractions [17]. Grain boundaries act as potential barriers for electrons as they move between two crystalline grains through amorphous tissue. The width of this amorphous tissue is inversely proportional to the crystalline fraction [17]. If the grain boundary thicknesses are below 3 nm then the electrons can tunnel through. Additionally, the formation of grain boundaries can be influenced by substrate textures and can be accelerated though use of seeded layers [18].

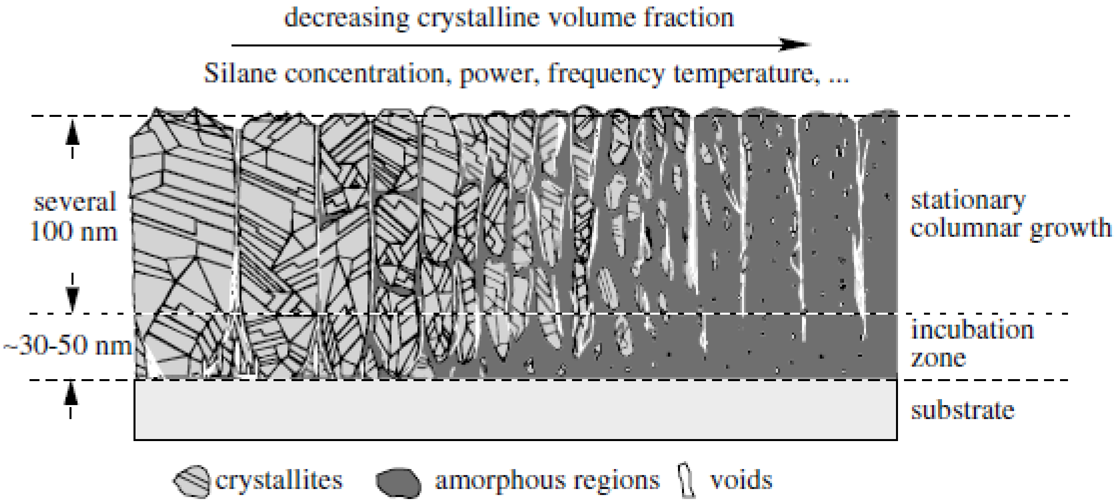

Figure 16: Transition of amorphous silicon into crystalline silicon following an incubation layer. Material properties and growth depends on deposition parameters. Adapted from [6].

The size of crystal grains also play an important role in performance of the cell [19]. Large grain sizes result in higher V_{oc}, but the grain sizes in nc-Si:H is limited by its nature to 10-50 nm, and therefore limits the final V_{oc}. High quality nc-Si:H is characterized by homogeneous crystalline grains of certain size, relatively low grain-boundary recombination, the right amount of amorphous tissue (crystalline fraction) passivating any cracks. This type of material can be grown by tuning the deposition conditions and is substrate dependent [6].

The typical bandgap of nc-Si:H is between 1.1-1.3 eV[10], which means it absorbs light below a wavelength of 1127 nm. This allows potential short circuit currents as high as 33 mA/cm^2 with absorber layers of 10 µm thick[20], however, this thickness is not practical for thin film solar cells. A further drawback of nc-Si:H solar cells is the low V_{oc}, limited not only by the current but also by the increased recombination effects in the material compared to crystalline silicon solar cells. Short-circuit current values above 28 mA/cm^2 have been achieved for 2 µm and 3 µm thick absorber layers by changing deposition conditions, introducing light trapping, and using novel processing techniques. The highest efficiency for single junction microcrystalline solar cells achieved to date is 11.8% (V_{OC} = 0.548 V, J_{SC} = 29.4mA/cm^2, FF = 0.731) [21].

3.6 Layers in a microcrystalline solar cell

A typical a-Si:H or nc-Si:H solar cell share the same structure. Figure 17 shows a typical single junction nc-Si:H cell deposited on Al foil using the same construction philosophy applied to HyET's a-Si:H cells. The light enters through a top encapsulation which is usually glass/EVA or polymer that is used to protect the cell from the outside environment (not shown here). This is followed by a transparent conductive oxide (TCO). The TCO is used for lateral conductivity of charge carriers in monolithic thin film PV devices. To facilitate this, the TCO should have very low series resistance. As the light travels through the TCO it should not absorb light intended for the absorber layer, therefore it must be optically transparent in the operating wavelength range of the photoactive layers. Commonly used TCO materials are aluminium doped zinc oxide (AZO), fluorine doped tin oxide (FTO), boron doped zinc oxide (BZO) and indium tin oxide (ITO). As explained earlier, HyET incorporates FTO and AZO as the front and rear TCO, respectively. For experiments conducted at TU Delft, AZO is deposited as the front TCO with a thickness of 700 nm, this is partly because EKL does not have the facility to deposit FTO.

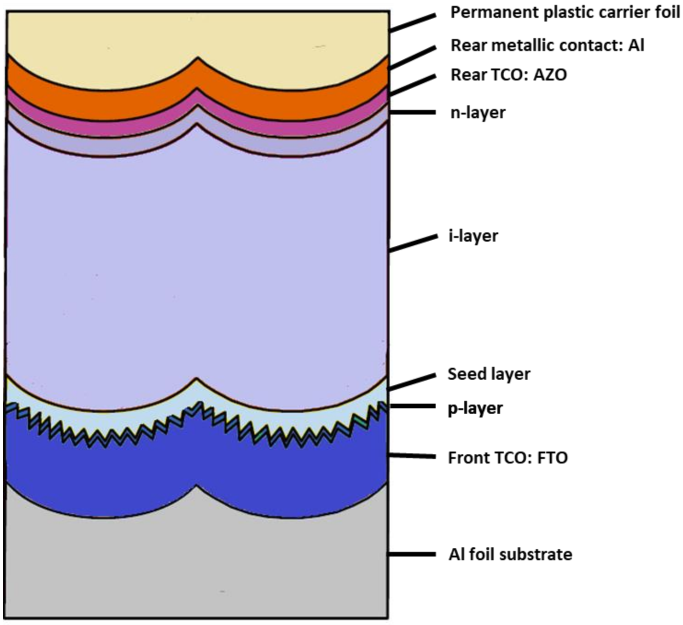

***Figure 17**: The different layers in a nc-Si:H solar cell deposited on Al foil substrate. Permanent carrier is laminated at the end before the temporary substrate is etched away. Adapted from [22].*

After the front TCO, a p-layer is introduced, which is usually p-doped nanocrystalline silicon oxide (p-nc-SiO_x:H). The layer is intended to be highly transparent to reduce parasitic absorption. This is achieved by its high bandgap and small thickness in the order of tens of nanometres. Another reason for a very thin p-layer is that it has high defect density and almost no photogenerated current within the layer is collected due to recombination. The main purpose of the p-layer is to generate the electric field and act as a hole collecting layer.

Next is the intrinsic nc-Si:H layer or the absorber layer. Typical nc-Si:H solar cells have i-layer thicknesses varying between 1 to 3 µm depending on light trapping technique used. The i-layer is free of impurities to ensure that charge carriers can drift through it without recombining. The absorption coefficient of nc-Si:H is lower than a-Si:H, which is why it requires a thickness of 10 times that of a-Si:H.

The i-layer is followed by an n-doped nanocrystalline silicon oxide (n-nc-SiO_x:H), this layer should have similar properties to the p-layer and acts as the electron collecting layer. The p and n layer thicknesses can be optimized to improve light coupling into the i-layer at the p-i and the n-i interface. The n-layer is followed by the rear TCO which serves a similar function to the top TCO. Based on the construction philosophy the rear TCO is omitted and a metallic back contact is used which also acts as a good back reflector. In the case of HyET, an 80nm thick AZO followed by 300 nm thick Al is deposited as a back contact.

3.7 Superstrate (p-i-n), substrate (n-i-p) configurations

The solar cell layers can be deposited in a superstrate configuration, conventionally this is done on glass which acts as the top encapsulant. The substrate must also be transparent as light enters the cell through the same. In superstrate configurations it is important to maintain a good p-i interface such that good quality nc-Si:H can be grown immediately. Usually, a buffer or seed layer is needed to improve the interface, and in some cases, this is incorporated into a highly crystalline p-layer. Another reason for having a good p-i interface is to facilitate hole collection. Holes usually have a lower mobility and carrier lifetime compared to electrons, resulting in quick recombination. Most of the high energy photons are absorbed near to the p-i interface to produce charge carriers so the holes must be able to drift towards the TCO layer without recombining. If the p-i interface is defect rich most holes will recombine before collection, leading to a loss in output. A drawback of the superstrate deposition can be that the substrate textures can have a negative influence on the p-i interface and quality of the subsequent layers.

In substrate configuration, the n layer is grown first, followed by the i and p layers. As the substrate will form the back of the cell, an opaque material can be used such as plastic or metal which serves as a back reflector or contact. Here, there is less need to focus on the n-i interface and more flexibility is provided towards optimizing the p-i interface which is not influenced by substrate morphologies or the nucleation/incubation phase [23].

Taking the above into account, HyET introduces a more unique approach using a temporary superstrate configuration. The main reasons for using this is its cost-effectiveness and ease of application in their largescale roll to roll production process. Furthermore, Al foil facilitates the growth of a high quality, homogeneous FTO (front TCO layer) on the same. Figure 17 shows the solar cell stack deposited in superstrate on the Al foil. Figure 18 shows the completed cell after the temporary Al substrate is removed and top is encapsulated.

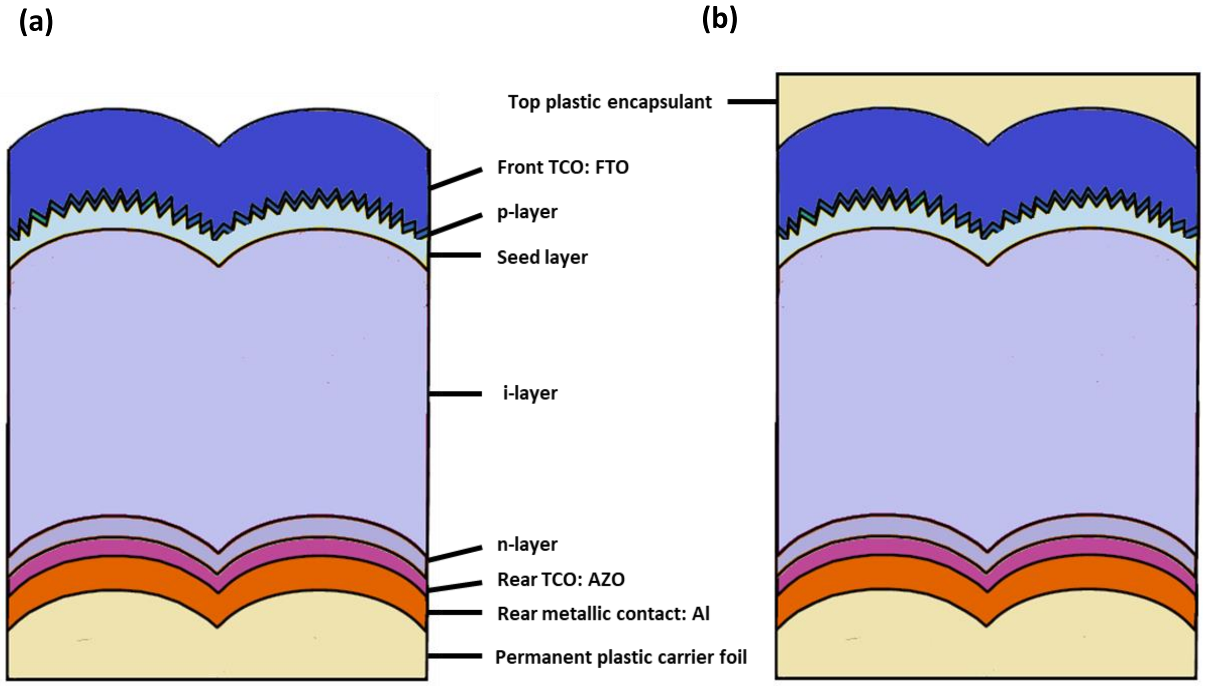

***Figure 18**: (Left) Shows the solar cell stack after the temporary Al foil has been removed, (Right) The same solar cell stack is completed with the top plastic encapsulant. Adapted from [22].*

3.8 Light trapping, modulated surface texturing and appearance of cracks

Light trapping is an important aspect of thin films, because it contributes to further reducing the thickness of thin film solar cells while achieving the same or higher short-circuit currents. In p-i-n cells it is achieved by texturing the glass substrate, the TCO layer adopts the surface morphology of the substrate and subsequently the other p-i-n layers adopt the morphology at each succeeding interface. The sharp nano-sized features at the TCO/p-layer interface cause Rayleigh scattering inside the absorber layer. This increases the optical path length of the light inside the i-layer so that more of it can be absorbed, thus enabling a reduction in thickness. For n-i-p cells, the same can be achieved by texturing the back metallic contact.

However, there should be a compromise between sharpness of surface features and the extent of light trapping required. It has been found that too sharp features on the substrate are detrimental to the growth of nc-Si:H. This results in cracks and voids along troughs of the v-shaped features. Cracks are found in regions close to the substrate and are linked to internal stress in the film during the onset of growth [18]. The cracks act as shunt paths in the solar cell resulting in low shunt resistance and high reverse saturation current leading to a poorly performing solar cell. An example is shown in figure below, the crack is shown in a white line; the crack seems to form at the valley and propagates upwards.

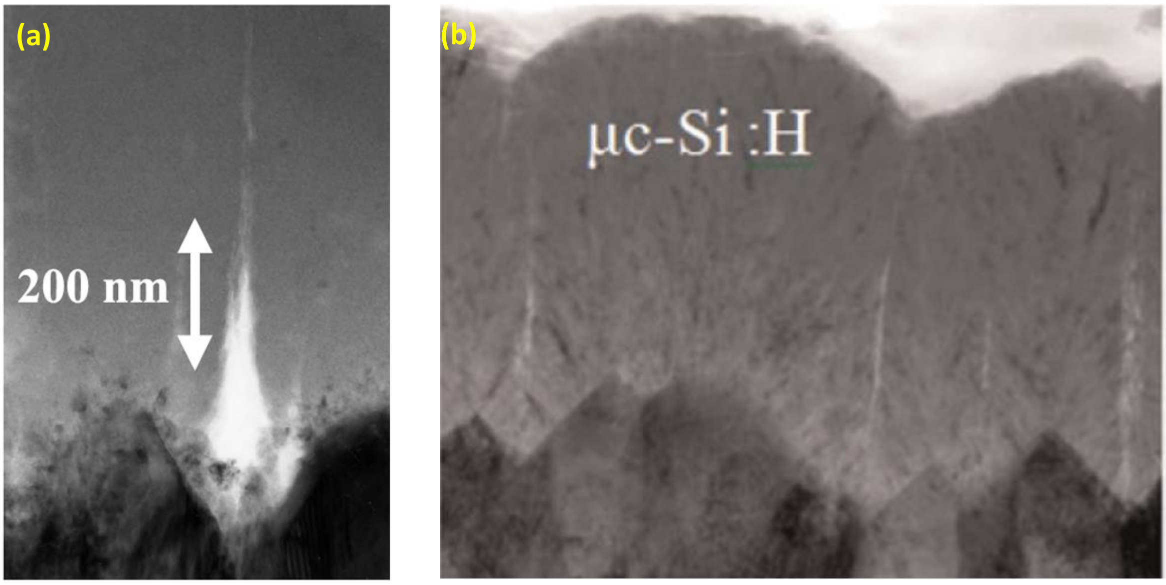

Figure 19: The formation of cracks in (a) the valleys of the substrate[24], (b) Cracks propagate upwards from the sharp features of front TCO [25].

To reduce the effect of cracks and maintain a good level of light trapping, the so-called modulated surface texturing (MST) is used. MST uses a combination of micro-sized and nano-sized features that result in different light scattering mechanisms to couple more light into the active layers [26]. This concept is illustrated in Figure 20.

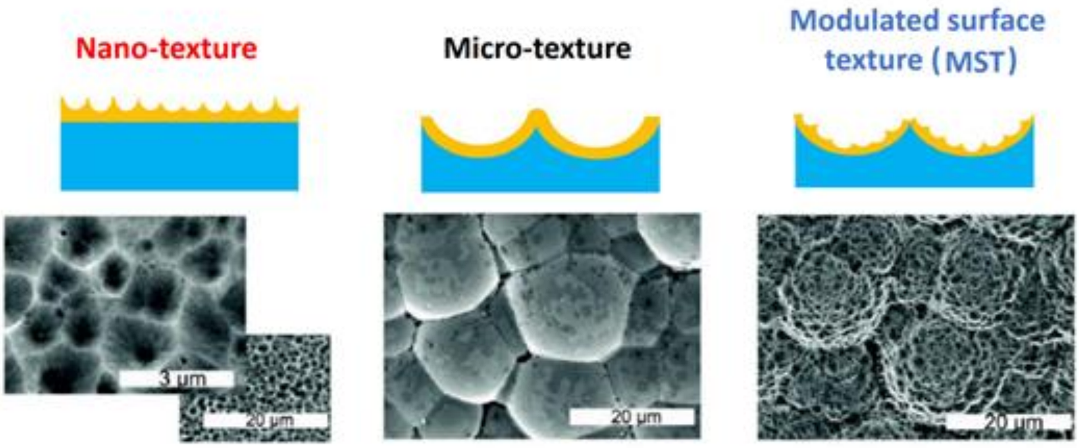

Figure 20: The combination of nano-sized features grown on micro-sized features result in the creation of modulated surface features. Adapted from [10].

Another advantage of using micro-sized u-shape craters is to reduce the formation of cracks. This allows the columnar growth of crystallites perpendicular to a relatively flat surface (large radius of curvature) leading to less collisions between crystallites and resulting in less grain boundaries and voids [27]. When compared to a rough substrate, MST can achieve a good compromise between high quality nc-Si:H and effective light trapping.

The concept of MST on glass has already been shown to provide high quality nc-Si:H solar cells with an efficiency of 10.2% at an i-layer thickness of 3 μm [22]. The growth of a naturally nano-textured TCO on the micro-textured substrate creates the characteristic of MST. The same can be applied to work done in this thesis, where different MST can be prepared on Al foil substrates. This is achieved by wet chemical etching the Al foil in different solutions to create micro-sized features depending on external factors such as concentration and temperature of etchant, and etching time.

4 Experimental Methods

This chapter presents an explanation of the various tools available at EKL and PVMD to fabricate the cells layers and characterise them. In addition, some theory that is relevant to the analysis is also discussed.

4.1 Plasma enhanced chemical vapor deposition

Plasma enhanced chemical vapour deposition or PECVD is the main process used for depositing amorphous and nanocrystalline silicon. A PECVD tool works by creating a plasma consisting of ionized source gases. The source gases are silane (SiH_4) and hydrogen (H_2) for creating intrinsic i-layers. Diborane (B_2H_6) is mixed to create p-doped layers and phosphine (PH_3) is mixed to create n-doped layers, additionally a mixture of carbon dioxide (CO_2) and methane (CH_4) is used to create n or p doped nanocrystalline SiO_x:H layers.

The plasma in the intrinsic nc-Si:H deposition chamber is created by a VHF field between two parallel electrodes. The free radicals and ions that are formed in the plasma are accelerated towards the substrate, whereby they interact on its surface and get deposited to form the layers. The internal reactions inside the PECVD chamber, although complex and difficult to model, can be controlled by external parameters such as ***chamber pressure, temperature, gas flow rates, discharge excitation frequency and power*** [28]. The material grown in PECVD tool can be tuned by varying these parameters, although discharge excitation frequency is fixed to 40.6 MHz for the VHF generator and 13.56 MHz for the RF generator.

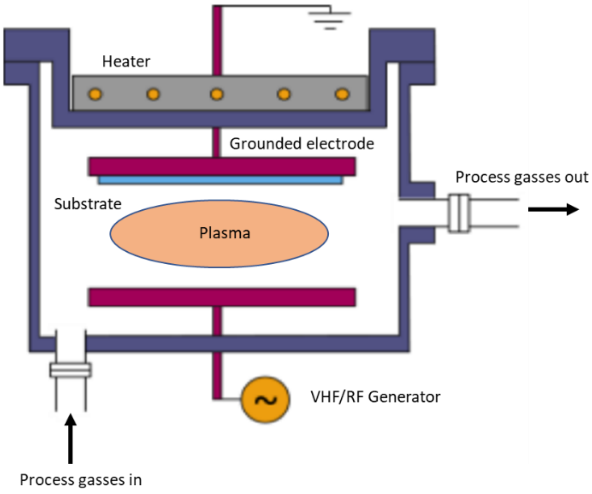

***Figure 21**: Schematic diagram of a PECVD chamber. The AMIGO at EKL contains 5 such PECVD chambers. Adapted from [29].*

There are several advantages of using higher excitation frequencies, firstly it leads to higher dissociation rates resulting in higher electron densities and ion flux densities for a smaller excitation power when compared to RF. This also leads to higher deposition rates as more reactions take place at the substrate. The peak ion energy in the plasma also reduces at higher frequencies meaning the bombardment of ions on the substrate surface is less aggressive, leading to better quality material growth on the substrate surface. Additionally, the lower electron temperature is able to more effectively generate atomic hydrogen which yields better growth of nanocrystalline at low powers [30].

The PECVD tool used at EKL for the experiments carried out under this thesis project is known as the AMIGO. The AMIGO consists of 6 chambers, namely, DPC 1 to DPC6. DPC1 is used for p-doped layers, DPC2 is used for n-doped layers, DPC3 for intrinsic a-Si:H layers, DPC4 for intrinsic nc-Si:H layers, DPC 5 is used for a-SiGe:H and DPC6 for RF magnetron sputtering which is used to deposit ZnO:Al. The AMIGO has a load lock which allows up to five samples to be inserted or retrieved at one time at atmospheric pressure, while the rest of the tool is kept at vacuum level.

The AMIGO can be operated manually by adjusting the external parameters or automatically using a recipe. The recipe is a line by line file which specifies all the actions and parameters of the machine. This includes the actions of the robot arm to move the samples between chambers before and after depositions. It allows the user to set the time for each process line such that process flows can stabilize before the VHF/RF generator is switched on and the plasma is ignited. An important aspect of the AMIGO is the tuning of the load and tune capacitors to match the load impedance of the chamber such that maximum RF power can be delivered to the gases in the chamber [31]. The load and tune values can be dependent on power, pressure, and flows; therefore, they need to be optimized when working with new parameters. If not optimised, the machine reads a high reflected power. This indicates that the process gasses are not supplied with the required power to maintain the plasma and result in little or no deposition.

By using carefully optimized and controlled parameters, we can expect layers with different characteristics to grow on the substrate. Using several characterization methods, we can understand the nature of the depositions and link them to the deposition parameters. This allows the outcome to be reproduced. Some of the important parameters are discussed below:

Gas flow rates: The gas flow rates control the volume of gas being supplied into the PECVD chamber per unit time, it is usually given in sccm (standard cubic centimetres per minute). In DPC4, only the hydrogen and silane flow rates are specified. An important parameter is the silane concentration (S_c), which influences the growth of the material. The silane concentration is given by:

$$S_c = \frac{[SiH_4]}{[SiH_4] + [H_2]} * 100\% \tag{4.1}$$

At higher silane concentrations, the amount of silane with respect to hydrogen is high, this results in amorphous material being formed on the substrate. By varying the S_c, its effect on the growth of nc-Si:H on Al foil substrate can be observed. This can be used to further optimise the material properties.

Deposition power: The plasma excitation power is the power delivered by the VHF/RF field to create and sustain the plasma. At high powers, the dissociation rate of ions in the plasma increases and the material builds up more quickly on the substrate, a disadvantage is that the high ion bombardment can destroy the substrate surface. An advantage of using higher frequencies is that it requires less power to create an electron ion pair [17].

Deposition pressure: Increasing the chamber pressure can lead to a decrease in ion energy, and thus result in less aggressive growth on the substrate, however this also results in a thick incubation layer as there is less energy for formation of H_α (Balmer alpha resulting from H_2 dissociation) resulting in less hydrogen available for crystallization [17]. Different values of pressure can lead to different characteristics in solar cells due to altered material growth. The deposition pressure for i-layer deposition is kept constant at 4 mbar in all experiments unless stated otherwise.

Substrate temperature: This is known to have an effect on the growth of material [18]. The deposition of doped and intrinsic layers is done at a substrate temperature of 180°C throughout this thesis.

4.2 RF Magnetron sputtering

RF magnetron sputtering is carried out in DPC6 of the AMIGO. It is used to deposit the front TCO that is namely, aluminium doped zinc oxide (ZnO:Al). Sputtering is the main choice for depositing many other dielectric layers for thin-film applications [32]. Sputtering is carried out at a radio frequency of 13.56 MHz. Similar to a PECVD chamber, it consists of two electrodes. The target material is held at one electrode; this is the material that is to be deposited on the substrate. The substrate is held at the grounded electrode, which is the aluminium foil substrate.

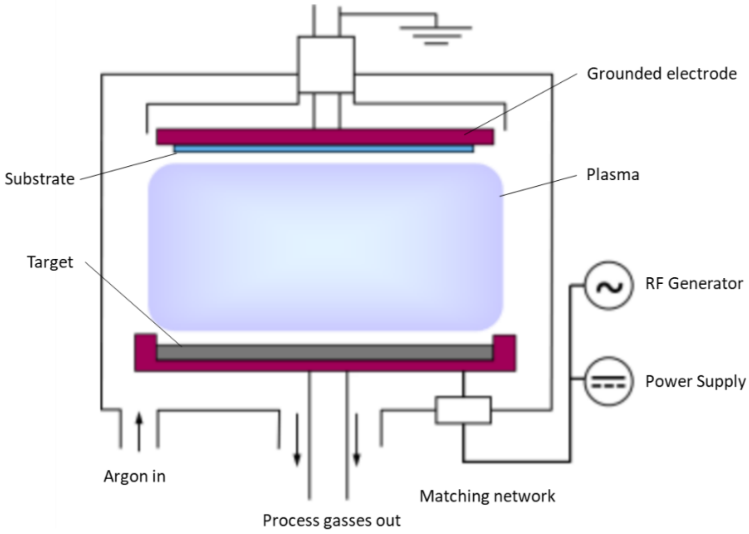

Figure 22:Schematic diagram of RF magnetron sputtering chamber in the AMIGO. Adapted from [29].

The target consists of a ZnO powder and Al_2O_3 powder with 99.9% purity mixed with ratios of 98:2 wt. %. The plasma is created by an alternating RF field applied between the cathode and the anode. The sputtering gas which is used to create the plasma is argon due to its inert properties. The surface of the target is bombarded by high energy ions from the plasma which create atoms that are sprayed towards the substrate. These atoms then interact with the Al foil surface where they are deposited. RF magnetron sputtering uses magnets behind the cathode to trap electrons, so that they do not bombard the substrate, which leads to higher mean free path for the target atoms resulting in a higher yield [33]. The alternating RF field also helps prevent the charge build up by constantly cleaning the target material.

It should be noted that the sputtered atoms are sprayed in all directions and will reach the substrate after random motion. In the AMIGO, the substrate is heated up to about 180^{o}C, this process takes up to about 30 mins and the sputtering process takes approx. 80 mins. The deposition rates are lower compared for intrinsic nc-Si:H layers.

4.3 Evaporation

The evaporation tool is used to deposit the aluminium back contact. Although the back contact is exclusively deposited at HyET to make the final cell, sometimes it is required to make individual cells on lab scale for dark I-V measurement, for this purpose the EKL based tool is used. The Al back contact is deposited after the back TCO layer. Evaporation is the best tool for depositing the back contact in thin films as opposed to screen printing or electroplating. This process is quite similar to HyET's back contact sputtering process, which allows for a fair comparison between lab scale and industrial scale efficiencies.

The evaporation tool works by heating aluminium pellets which are located in a crucible. The metal is heated until it is vaporised, whereby it travels upwards to the inverted substrate. The metal is deposited and condenses to form the contact. The process in undertaken in high vacuum which increases the mean free path. This is the average distance a vapor molecule can travel without colliding with another gas molecule [34]. Collisions are not desired as it would change the direction of travel and affect the uniformity of the deposition. Another reason for having a high vacuum is to remove impurities from the chamber.

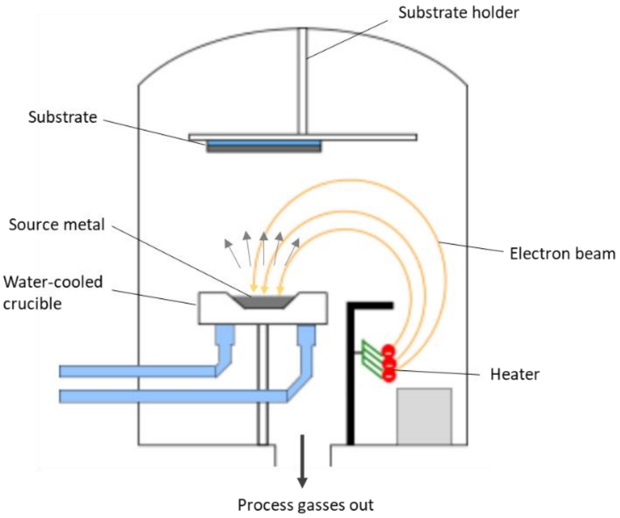

***Figure 23**: Schematic diagram of the PROVAC chamber which shows e-beam evaporation. Adapted from [29].*

There are two main heating sources, the first is the filament evaporation that consists of an electrical resistive heating element. This is a tungsten boat that accommodate the metal pellets. The second is called Electron Beam. The E-beam is created by a hot filament that releases electrons. These electrons are directed by a magnetic field to the crucible containing the material, which then heats up to form the vapor. The crucible itself is water cooled to prevent its destruction [35]. The evaporation tool at PVMD called "PROVAC" consists of both heating sources. The first one is used for silver (Ag), whereas the second is used for metals with higher melting points such as chromium (Cr). Even though aluminium has a lower melting point, the E-beam is used, this is to prevent the Al alloying with the tungsten boat. Additionally, the tool allows the control of deposition rates and thickness to achieve the desired the layer properties.

4.4 Raman Spectroscopy

An important tool used to characterize the depositions is a Raman spectrometer. It is named after C.V. Raman who discovered the Raman scattering effect. As mentioned earlier, the crystalline fraction is an important indicator of the quality of deposited nanocrystalline silicon films. Raman spectroscopy has much broader applications for studying the structure of materials by relying on a specific signature or fingerprint that can be used to distinguish different materials. This signature can also help distinguish between good and bad quality material. The advantage of using Raman is that it is relatively quick and non-destructive. However, in the case of using aluminium foils it is not the case since the depositions are bent due to inbuilt stresses. This gives some difficulty as the foils need to be kept flat whilst the measurement is taking place. This can result in damage to the films.

The Raman scattering effect is due to a phenomenon whereby molecules or atoms in a structure create a shift in the frequency of the incident absorbed light when it is scattered back into the surroundings. This shift is due to the vibrational energy of the bonds between atoms in the structure, also known as phonons. The scattering can be of two types:

- Elastic scattering or Rayleigh scattering whereby the scattered light has the same wavelength or frequency as the incident light.
- Inelastic scattering where the scattered light has a different wavelength compared to the incident light.

The shift in frequency depends on how the chemical bonds interact with the incident light. Reflected light which has more energy than the incident light is called stokes peaks and that which has less energy than incident light is called anti-stokes peaks.

A Raman spectrometer usually shows the shift in frequency as a wavenumber (cm^{-1}). The wavenumber is calculated as shown below:

$$\bar{v} = \frac{v}{c} = \frac{1}{\lambda} \tag{4.2}$$

$$\Delta\bar{v} = \bar{v}_{laser} - \bar{v}_{Raman} = \frac{10^7}{\lambda_{laser}(nm)} - \frac{10^7}{\lambda_{Raman}\,(nm)} \tag{4.3}$$

The wavenumber shift is calculated relative to that of the incident light. The $\bar{v}_{laser}$ value is a constant for a fixed laser wavelength. At PVMD, the spectrometer contains a green laser (514 nm) corresponds to a wavenumber of 19450 cm^{-1} and red laser (633 nm) corresponds to a wavenumber of 15800 cm^{-1}. The shift is shown relatively such that $\bar{v}_{laser}$ point is zero. The use of having two lasers is to probe deeper into the layers, the green laser can probe the surface of the sample or towards the end of the deposition, whereas the red laser can probe deeper thus examining the layers towards the beginning of the growth. This becomes important when investigating whether material properties are homogenous throughout the thickness of the material.

Interpreting the Raman spectra of nc-Si:H or a-Si:H is a simple yet daunting task. The Raman shift of crystalline silicon is centred at 520 cm^{-1} with a sharp gaussian distribution as shown in Figure 24, which is mainly due to its single optical phonon mode that is also related to its uniform, crystalline structure [36]. Amorphous silicon on the other hand has a variety of phonon modes and thus exhibits a peak at 480 cm^{-1} with broad tails extending to either side. Nanocrystalline silicon also features a peak at 520 cm^{-1}, but with a tail that extends towards lower wavenumbers; this is indicative of a crystalline phase as well as amorphous tissue or defects within the bulk of the nanocrystalline structure.

The Raman spectrometer is easy to use, it consists of a stage to load the sample and a microscope which allows the user to focus the view on a very small point on the sample up to 100x magnification. Once the view is in focus, the user is able to switch between the red and green laser from the software and also physically change between lenses dedicated for each laser. This is followed by adjusting the intensity of the laser beam and focusing it on a small area of the sample. The following settings are usually used for the measurement:

- **Spectrum range**: The range of the wavenumber shift that the apparatus measures usually between 200 cm^{-1} and 1000 cm^{-1}.
- **Exposure time:** The time for which the scattered light is exposed to the sensor; increasing this value improves the quality of the spectrum but also increases measurement time. This value is usually set at 100 s.
- **Laser power:** The laser power is usually set at 5% for both amorphous and nanocrystalline silicon, increasing the power might cause further crystallization and result in altered results.

Increasing laser power also increases the maximum counts in the spectrum as more power is scattered back from the sample.

- **Number of accumulations:** The number of times that the spectrometer repeats the experiment to remove any noise. This is usually set to 1, as increased accumulations, drastically slow down the measurements.

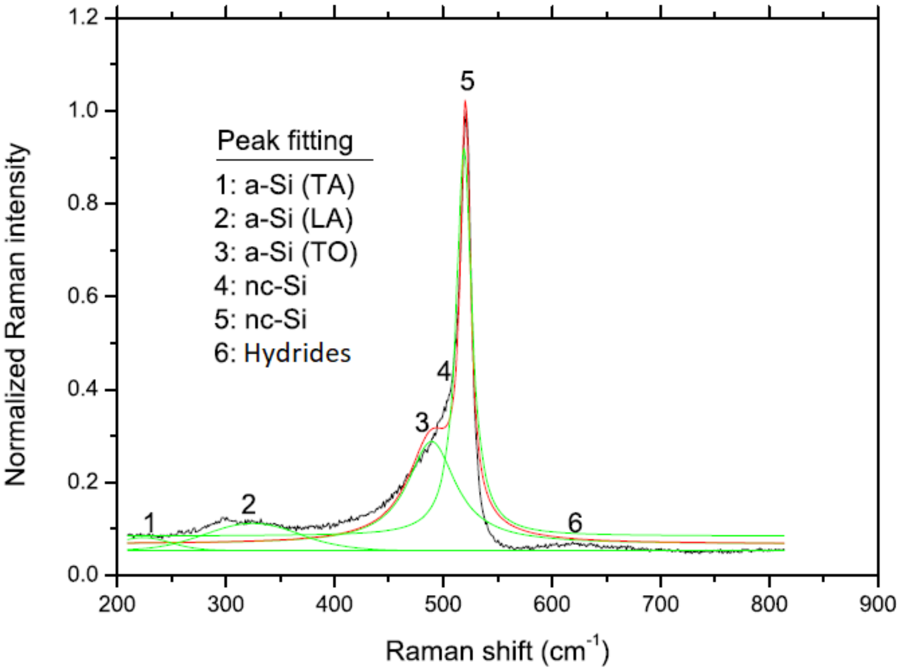

Figure 24*: The different peak fitting Gaussians used to fit the raman spectrum and obtain the crystalline fraction. Adapted from [18].*

The daunting part of the analysis is calculating the Raman crystalline fraction. Several literatures have been published on extracting the crystalline fraction from the Raman spectra. Although they vary, the principle remains the same, where the aim is to fit several Gaussian peaks into the spectra such that the individual contributions of the phonon modes can be extracted. The individual spectra are characterized by Gaussian or Lorentzian peaks centred around certain wavenumbers. Firstly, the amorphous contribution is calculated by considering the phonon modes at the transverse acoustic (TA) peak of 220 cm^{-1}, longitudinal acoustic (LA) peak of 330 cm^{-1} and transverse optical (TO) peak of 480 cm^{-1} [18]. The crystalline contribution is found by fitting the peaks at 520 cm^{-1} which is the main peak and 510 cm^{-1} (varies based on literature) which is the peak representative of defective crystallites with very small grain size [37]. The Si-H wagging mode (hydrides) can also be found around 650 cm^{-1} [36].

The crystalline fraction can then be calculated by using the following formula:

$$Crystalline\ fraction\ (\%) = \frac{I_{520} + I_{510}}{I_{520} + I_{510} + I_{480}} \times 100 \tag{4.4}$$

Where $I_{520}, I_{510}\ and\ I_{480}$ are the areas integrated under the gaussians at the wavenumbers 520 cm^{-1}, 510 cm^{-1} and 480 cm^{-1} respectively. The limitation of the above equation is that it does not give actual crystalline ratio as a fraction of the whole material, but only that relative to the amorphous portion of the material. Therefore, it can be used only as an indicator for comparing between different samples when using the same approach. It should be noted that other methods of calculating crystalline fraction can yield different values, therefore, one should be weary of using crystalline fraction as an indicator of the solar cell quality, especially when comparing with high efficiency solar cells stated in literature [36]. For this thesis, a MATLAB script is used to calculate the crystalline fraction as per the method described in equation 4.4 above.

4.5 Raman Spectrum in the extended range (Hydride stretching mode signatures)

Another important application of Raman spectroscopy is measuring the spectra at higher wavenumbers, typically between 1800 cm^{-1} and 2300 cm^{-1}. Information about the structure of the material can be derived by analysing the shape of this spectra, including the peaks corresponding to several wavenumbers, as is with the case of the normal spectra explained in the previous section. It should be noted that for this experiment, we increase the exposure time from 100 s to 300 s to improve the signal to noise ratio.

The extended range focuses mainly on the stretching modes (SMs) of hydrides; these are the bonds between silicon and hydrogen atoms. Since each silicon can make up to four bonds, these can be either monohydrides (Si-H), dihydrides (Si-H$_2$) or trihydrides (Si-H$_3$). According to literature, this spectra can also be fitted using gaussian peaks at certain wavenumbers corresponding to different SMs [38]. The stretching modes are representative of hydrides in amorphous tissue, the nc-Si:H bulk and the hydrides that are passivating the crystalline grain boundary surfaces. One major finding of the extended range is that twin sharp peaks around 2100 cm^{-1} are representative of porous material as shown in Figure 25. When exposed to air or water, the grain boundaries easily oxidize and over time the twin peaks disappear as the Si-H$_x$ bonds disappear. At the same time a new peak appears at 2250 cm^{-1} which can be attributed to the formation of O-Si-H$_x$ bonds. This peak, however, is only more visible when using IR (infrared) spectroscopy, but in the case of Raman, only a small shoulder will be observed.

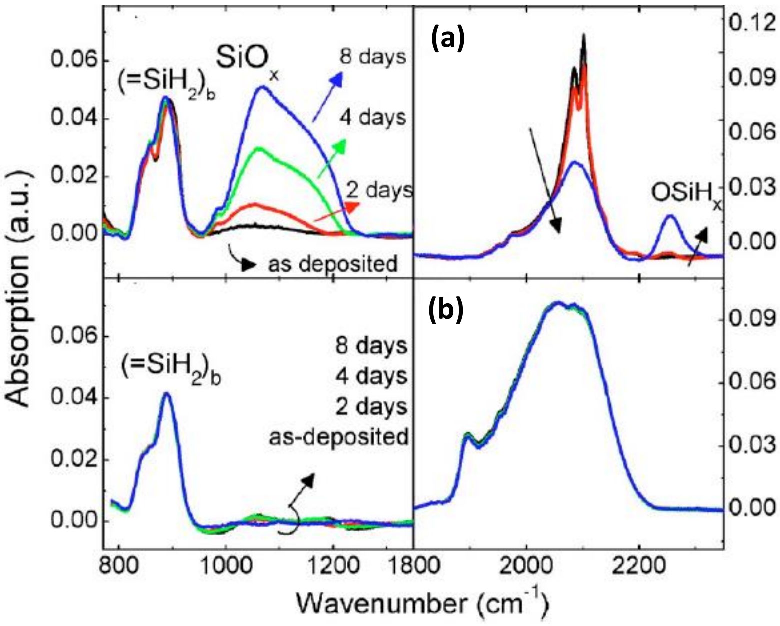

Figure 25: The hydride stretching modes for two different nc-Si:H depositions (a) Sharp peaks result in post-deposition oxidation after 8 days, (b) Good signature results in no post-deposition after 8 days and high efficiencies of 9.1%. Adapted from [38].

Therefore, we know that for good quality solar cells, with well passivated non-porous grain boundaries, the signature in the extended range should not include the sharp twin peaks. In addition, several studies have been undertaken to obtain an optimum signature which is characterized by having a denser bulk material and reducing the defective Si-H$_x$ bonds at grain boundary surfaces. Material with such good signatures (Figure 25(b)) have been reported to show no post-deposition oxidation and no reduction in the red-light response, as well as produce high efficiencies in solar cell applications.

The signature in the extended range is reported to change with varying silane concentration (or hydrogen dilution ratio). Therefore, by undertaking various experiments, we are able to match the signature of nc-Si:H material on aluminium foils to those reported in literature to achieve a high efficiency solar cell. The optimum signatures are shown in Figure 26(a); it corresponds mainly to curves D, E and F. The Raman spectrum is slightly distorted compared to IR spectroscopy, however, there is a shoulder at 1900 cm^{-1}, and two broad peaks at around 2030 cm^{-1} and 2100 cm^{-1} and is almost flat between 2200 cm^{-1} and 2300 cm^{-1}. The early part of the thesis project involves the optimisation of the deposition to match the signature before proceeding to cell fabrication at HyET Solar. The advantage of this method is that it is easy to analyse and understand, especially with a substrate that is not glass. No complex fitting procedures were needed as we are concerned only with reproducing the spectra of the optimum signature.

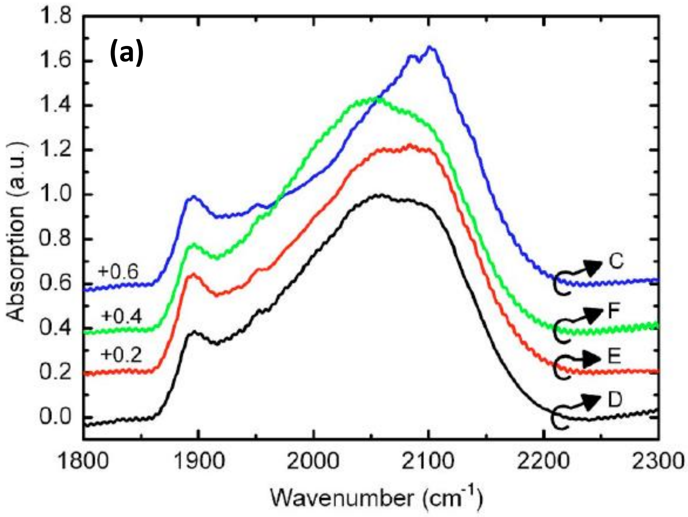

(b)

	X_c (%)	η (%)
C	80	5.7
D	73	7.0
E	69	6.8
F	70	6.9

***Figure 26**: Various depositions C D, E and F done on corning glass while varying the hydrogen flow rate. (a) This results in different signatures in the extended range corresponding to different streching modes in the bulk material. (b) The crystalline fractions and efficiencies for profiles C,D,E and F [38].*

4.6 X-ray diffraction (XRD)

X-ray diffraction (XRD) is another useful tool for understanding the material structure of the nanocrystalline silicon depositions. XRD is based on the constructive interference of monochromatic x-rays which are directed at a crystalline material. The lattice spacings in crystalline materials act as diffraction gratings for x-rays and create constructive interference when Bragg's law is satisfied according to $n\lambda = 2d \sin \theta$, where n is an integer, λ is incident wavelength, d is the lattice spacing and θ is the glancing angle.

By examining the reflected light at all angles, the counts for the different 2θ values corresponding to different crystalline lattice structures can be observed. The intensity at different 2θ values correspond to the presence of the crystalline orientations within the material. The main aim of using XRD in nc-Si:H depositions is to identify the different Si planes that exist within the structure and examine which have the highest contribution to high efficiency solar cells. This enables to create a fingerprint for high quality material similar to the signature in the extended range of the Raman spectroscopy.

Nanocrystalline silicon growth can be observed on the (111), (200) and (311) planes. For instance, studies have shown that nc-Si:H growth prefers the (111) plane and the effect of using seed layers prior to i-layer deposition increases the intensity of the (111) plane, while that of (220) and (311) planes are unaffected. This shows that seeding improves the crystal growth in the (111) plane [18]**.** Another factor that affects the intensity of these peaks is the crystalline fraction; as this fraction increases, there are more crystalline grains in the bulk leading to higher peaks.

Another important use of XRD is estimating the crystallite size from the From the Full Width at Half Maximum (FWHM) of the peaks by using Scherrer formula. Studies show grain sizes for nc-Si:H vary from 4 nm up to 30 nm. The grain size usually smaller at early stages of deposition and becomes larger farther up the substrate [18]. The grain size is also reported to increase with decreasing silane concentration or increasing hydrogen dilution as per the theory of nc-Si:H formation explained section 3.5. Grain sizes can also be determined by information from High Resolution Transmission Electron Microscopy (HRTEM); however, the analysis of grain sizes will not be part of the scope of this thesis.

It has been reported that nano-crystallites showing the (111) orientation result from random nucleation and representative of defective poly-hydride networks $(Si–H_2)_n$ at the grain boundary. On the other hand, the (220) plane-oriented crystals are found to be less defective with mono-hydride bonding, which is bond-centred hydrogen (Si-H-Si) in a platelet like configuration at the grain boundary. The growth of nc-Si:H along the (220) plane facilitates charge carriers to conduct perpendicular to the substrate in stacked devices such as solar cells and interact with fewer grain boundaries than in the (111) plane, and in addition allows the a-Si:H to further passivate the grain boundary surfaces. This results in lower recombination of charge carriers leading to higher V_{oc} and fill factor in solar cells. The conditions for preferential growth in the (220) plane is facilitated by frequencies higher than the conventional RF of 13.56 MHz [30].

4.7 Current-Voltage (I-V) Characteristics

The aim of a solar cell is to produce power or energy per unit time which can be used in the form of electricity. The output of solar cells is measured at standard test conditions (STC), where the cell is illuminated with the AM1.5G spectrum at an ambient temperature of 25°C (Figure 6(b)). At PVMD, a WACOM Class AAA, solar simulator is used for the same. It uses a xenon and halogen lamp to recreate the AM1.5 spectrum; the xenon lamp produces the blue part of the spectrum between 350nm to 600 nm and the halogen lamp produces the red part of the spectrum between 600 nm to 1500 nm. It is impossible for the simulator to recreate the exact AM1.5G spectrum, however its AAA class guarantees a good level of accuracy.

The I-V curve can also be measured in dark conditions (unilluminated), the purpose of measuring the dark I-V curve would be to check whether the solar cell exhibits a p-n diode behaviour in the case of a working cell, or resistive behaviour in the case of a defunct one. Prior to the measurement, a calibration of the spectrum is undertaken using two reference stages. The “test” cell is then loaded onto the stage and the probes are made to contact the cell. The voltage range for the measurement and the cell area is specified and the measurement is started. The load resistance is varied while the cell is illuminated, and the curve is displayed.

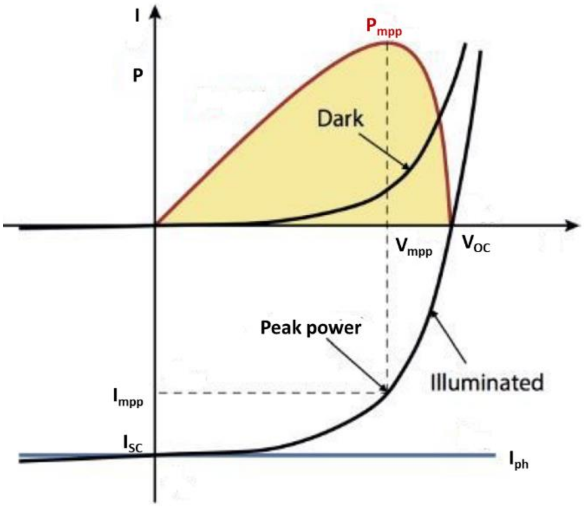

Figure 27*: The Dark I-V and Illuminated I-V characteristics can be measured under the AM1.5G spectrum using a solar simulator. Adapted from [7].*

Some important parameters from the curve is the open-circuit voltage (V_{oc}), short-circuit current (I_{SC}), maximum power point (P_{mpp}), and I_{mpp} and V_{mpp} which correspond to the current and voltage at maximum power point.

The fill factor (FF) is calculate as:

$$FF = \frac{V_{mpp} * \ I_{mpp}}{V_{oc} * \ I_{sc}} \tag{4.5}$$

The efficiency of the solar cell is calculated as:

$$\mu = \frac{V_{mpp} * \ I_{mpp}}{1000 \ W/m^2} = \frac{V_{oc} * \ I_{sc} * FF}{1000 \ W/m^2} \tag{4.6}$$

Two more important output parameters are the series resistance (R_s) and the shunt resistance (R_p) which are found from the slope of the I-V curve. The origin and effects of these resistances were discussed in the section 3.4 and therefore, these values can give us an idea of the defects in the cell and what needs to be improved.

4.8 Reflectance and Transmittance

Reflectance (R) and transmittance (T) measurements are done using the same equipment. In this case since the substrate is not transparent, the transmittance measurement cannot be done.

The sample with nc-Si:H deposition is placed at one end of the spectrophotometer. The user specifies the range of wavelength and the resolution over which the measurement is made. Usually the range is between 300 nm and 1200 nm, and a resolution of 5 nm is used to achieve a good compromise between speed and accuracy. A light is produced at one end which travels through a double monochromator which filters out a certain wavelength. The light hits the sample and is reflected around the integrating sphere as is shown in Figure 28. A detector in the integrating sphere is able to measure all the light that is reflected or scattered around inside it. The reflectance as a function of wavelength is displayed on the software.

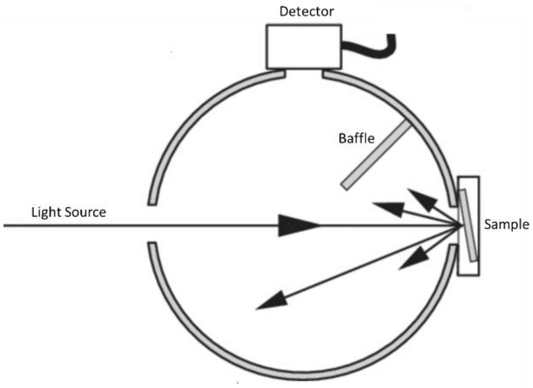

***Figure 28**: Schematic diagram of the integrating sphere inside the spectrophotometer for reflectance measurements. Adapted from [39].*

Several optical properties of nc-Si:H films can be determined from the reflectance (R) curve such as the absorptance, absorption coefficient and thickness. The absorptance (A) can be found using A = 1-R, at each wavelength. For example, HyET Solar uses the interference peaks in the R curve to estimate the thickness of the deposition. Additionally, the R gives information on the reflective properties of the substrate which is in turn related to the root mean square (RMS) roughness of the substrate [27]. The latter is most important since the thesis involves the creation of modulated surface texturing (MST) to achieve good light trapping properties. Therefore, the reflectance curves will be an indicator for surface roughness of the finished cells after the temporary Al foil is etched away.

4.9 AFM (Atomic Force Microscopy)

AFM is used to produce an image of the surface morphology of the Al foil substrates. Since different etching recipes lead to different surface morphologies, it is important to use AFM to understand their effect on surface features. AFM is a powerful tool capable of scanning surfaces with nanometre level accuracy. It uses a cantilever with a very sharp tip to probe over a surface. As the tip moves along the surface, the atomic force between the surface and the cantilever causes it to move closer to the surface, as this happens the repulsive force due to atoms become stronger and the cantilever is deflected from the surface. A laser beam is used to detect the cantilever deflections. By using a position sensitive photodiode (PSPD), the AFM tool is able to put together a high-resolution image of the area of sample under investigation [40].

Several indictors which can be calculated from AFM images are the root mean square (RMS) roughness (σ_{rms}), the correlation length (L_c) and the aspect ratio. The σ_{rms} is a measure of the roughness of the substrate with respect to an ideally flat substrate, a higher σ_{rms} value would indicate more prominent and frequent sharp features on the surface. It is calculated using the equation below:

$$\sigma_{rms} = \sqrt{\frac{1}{N}\sum_{i=1}^{N}(z_i - \bar{z})^2} \tag{4.7}$$

Where N is the number of data points, z_i is the height at the ith position and $\bar{z}$ is the average surface level.

The σ_{rms} on its own can be deceiving because it measures only the vertical height differences. The correlation length (L_c) is used as a measure of the horizontal roughness. This is done by picking two arbitrary points on the surface with a distance “r” between them. The square difference of the two heights is recorded as H(r). The value of r is varied until H(r) just becomes independent of r; this value of r corresponds to the correlation length [41]. In this case the correlation length corresponds to the diameter of the micro-sized craters. Another important parameter is the aspect ratio, which is the ratio between the σ_{rms} and L_c $(aspect\ ratio = \frac{\sigma_{\mathrm{rms}}}{L_c})$. The aspect ratio is an important parameter when it comes to quantifying and comparing different MSTs [22].

4.10 Scanning Electron Microscopy (SEM)

The SEM is a useful tool for observing deposited layers in very close detail. In order to measure features in the order of nanometres which are smaller than the wavelength of light, an SEM makes use of a stream of electrons which are emitted from a source. The electrons are directed by electromagnets towards the surface where they bounce off to produce secondary electrons. The secondary electrons are detected by a screen to produce an image [42]. The sample is held in vacuum while the measurement takes place. By using the complimentary software and settings, the user is able to take close up images of the surfaces at micrometre or nanometre levels, as well as make measurements of feature sizes. It also has different stages, e.g. one for making surface images and another for cross-sections with limited tilt angles.

SEM can also be used as an alternative to AFM for observing the surface morphology, however it is less informative than the latter w.r.t surface detail. The cross-section images can be used to verify the deposition of different layers and the quality. In addition, it is used to estimate the deposition thicknesses.

The SEM is quick and easy to use; however, it is a destructive method as a piece of the sample needs to be cut for it to be analysed. Non-destructive tools to measure thickness such as ellipsometry cannot be applied to nc-Si:H on textured Al foil, therefore, we are limited to SEM in our analysis. It should also be noted that observing cross-sections under SEM for Al foil depositions is not so straightforward, as there is no defined way of cutting the sample such that cross-sections are intact unlike for glass substrates. The samples were cut using a guillotine paper cutter. Finding a proper cross-section under the SEM can be a laborious task as the thick Al foil smears over most of the nc-Si:H during the cutting process. However, by careful observation, some active layers can be observed to be protruding at certain locations which provide an excellent detailed view of the nc-Si:H layers.

4.11 GenPro4 for optical simulations of nc-Si:H solar cells

This section is concerned with modelling the optical properties of the nc-Si:H solar cell layers. MST is used to enable growth of high-quality nc-Si:H while maintaining light trapping properties. Light trapping is achieved by using a combination of scattering effects which are attributed to the nano-textured features of the TCO which are superimposed on the micro-textured features imprinted by the Al foil substrate. The optical simulations are used to understand the optical gain (or losses) in the solar cell due to reflection, transmission, and absorption (parasitic or otherwise).

GenPro4 is a simulation tool developed by TU Delft, which makes use of ray and wave optics to simulate the optical model for thin film solar cells. The software is run using a MATLAB code. It is simple to use, yet powerful enough to provide accurate results. The solar cell layers are defined either as layers or, interfaces which are located between two layers. Interface layers are modelled as coatings to simulate interference effects of light between the layers. The surface morphology can also be modelled at the interfaces. This is done by loading a matrix containing AFM data of substrate textures. This allows us to implement a realistic version of MST in the optical model of the solar cell.

The output of GenPro4 is a graph of absorptance versus wavelength. The optical gain(losses) at each layer are interpreted as implied photocurrent density (mA/cm^2). The optical gain of the solar cell can be determined by looking at the absorber layers that contribute to photocurrent, namely the i-layer. Other layers which do not contribute to photocurrent generation such as the p and n-layer in nc-Si:H cells will be considered as optical losses. It should be noted that GenPro4 does not model electrical losses such as recombination, therefore the results will not be indicative of actual solar cell performance. However, in this thesis it will be used as a basis for comparison between different MSTs to investigate their effectiveness in light trapping and implied photocurrent.

4.12 Suitability of other characterization techniques

PVMD has an array of other tools that can be used to test the solar cells, such as ellipsometry, photoconductance lifetime tester, dark conductivity, and activation energy measurement. As explained previously, ellipsometry can be used only with non-textured substrates such as flat glass. Here, an optical model is used to calculate the refractive index and extinction coefficient and output the thickness of the deposited film. This process is non-destructive. The photoconductance lifetime tester is used to measure the minority carrier lifetime in crystalline silicon solar cells. This is a measure of the recombination in the solar cell and is used to estimate the implied V_{oc}. This is used mainly for optimizing passivation techniques for crystalline silicon solar cells. The apparatus is not applicable to nc-Si:H cells since minority carrier lifetimes are far too low.

The activation energy is a measure of the energy difference between the valence band and the fermi level in a p-doped material and the energy difference between conduction band and the fermi level in an n-doped material. It can be useful for measuring the performance of doped layers. The activation energy is calculated from the dark conductivity (σ_d); which is a measure of the electrical properties of the nc-Si:H under no illumination. However, the σ_d experiment cannot be applied to the nc-Si:H on the temporary Al foil due to the conductive nature of the substrate. The mobility gap can also be determined from the activation energy, this refers to the energy gap between states that contribute to charge transport as shown in Figure 15. It should be noted that due to the combination of varying size of nc-Si:H grains surrounded by amorphous tissue, the mobility gap is less defined compared to a-Si[43], therefore, this measurements will not be applicable in the scope of this thesis.

5 Results and Discussion

This section concerns with details of experiments undertaken under this thesis, the results and conclusions which are drawn from the same. For the sake of clarity, the experiments have been classified into “Work undertaken at TU Delft” and “Work undertaken at HyET Solar”.

5.1 Work undertaken at TU Delft

This section is based on the experiments undertaken at TU Delft using the tools available at EKL and PVMD.

5.1.1 Creation of substrate textures

As explained in section 3.8, the creation of MST is important for enhancing light trapping while enabling growth of high quality nc-Si:H. The same principle for creating micro-textures on glass substrates can be applied to the Al foil. Substrate textures can be created using various techniques such as:

1. Photolithography; can be used to create honeycomb like craters which has been known to yield the world record efficiency for a single junction nc-Si:H solar cell [21].
2. Hot embossing and imprinting [6].
3. Wet chemical etching of substrate.

The second and third options are mostly applicable for metallic substrates, however, the current process at HyET is most suited for the third. HyET uses sodium hydroxide (NaOH) wet etching in their roll to roll process. A concentration of 0.1M (mol/L) at a temperature of 35°C is used. This recipe does not produce the required feature sizes of MST in terms of RMS roughness and correlation length. This is shown in Figure 29 below, the craters represented by white circles are too small in size and unevenly distributed. When the TCO layer is deposited on the almost flat substrate, it does not facilitate growth of high quality nc-Si:H that is free of cracks as evidenced by the high contrast white lines Figure 30.

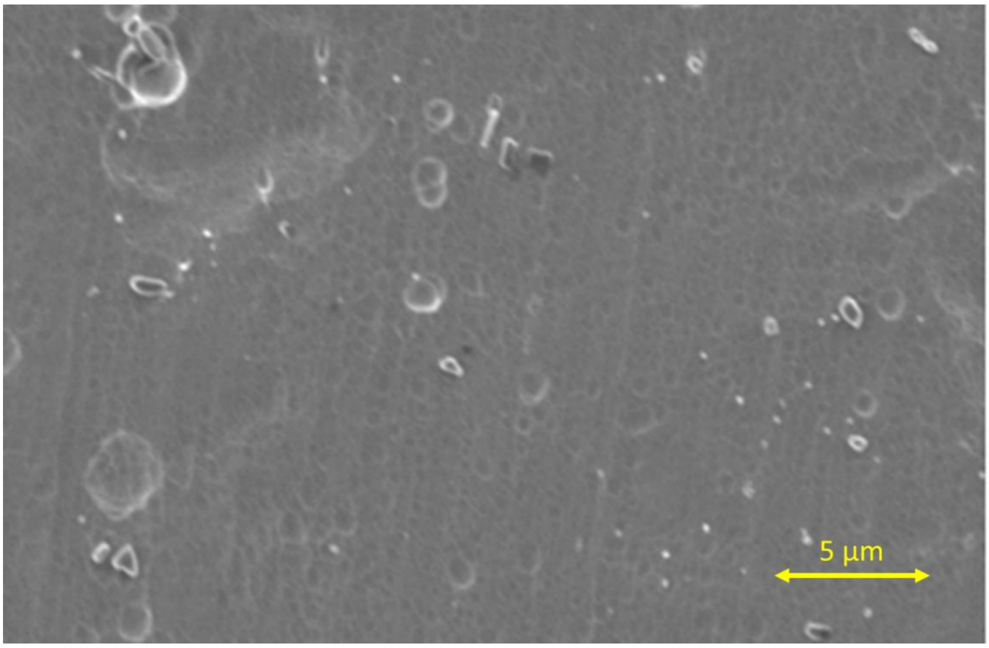

Figure 29*: The SEM images of the factory baseline etching shows almost no surface features which confirms poor texturing properties of the same [44].*

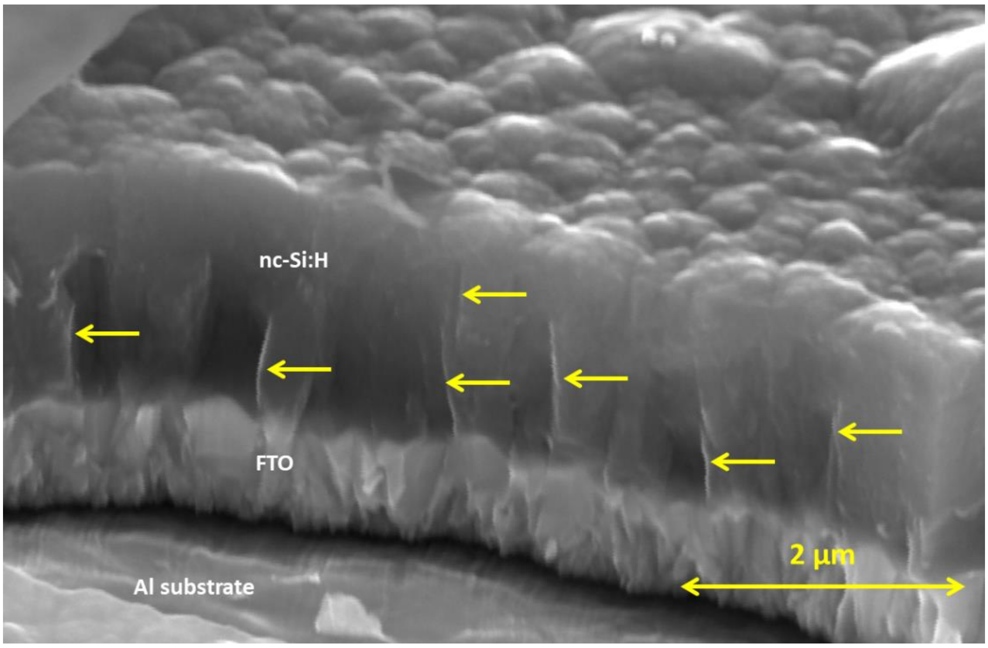

Figure 30: SEM image of nc-Si:H grown on HyET's factory baseline pretreatment results in many cracks. This is mainly due to the flat nature of the substrate.

At TU delft, MST on glass was prepared using wet chemical etching. A good MST is characterized by an aspect ratio between 0.14 to 0.16, with σ_{rms} between 200 to 600 nm and L_c between 1 to 4 µm [22]. This process can be easily tested on Al foil at lab scale and transferred to HyET's existing roll to roll processing. Although the process for Al foil etching varies slightly from that of glass, the principle remains the same. Six different etching experiments are defined as a starting point based on previous research with glass. They are listed below:

1. ITO is first deposited as a sacrificial layer on the bare Al foil. The ITO acts as a catalyst for etching and influences the texture features.
2. AZO is deposited as a sacrificial layer, similar to the ITO it may catalyse the substrate features.
3. Bare aluminium is used without any sacrificial layer.

In all 3 types of substrates, the samples are etched with two different etching recipes:

a. **ER1:** A 1:2:10 volumetric ratio of hydrogen fluoride (HF), hydrogen peroxide (H_2O_2) and water (H_2O) is used. This is prepared by mixing 100 ml HF, 200 ml H_2O_2 and 1000 ml of H_2O. The etching is done at 35°C for 3 minutes.

b. **ER2:** A 1.52M potassium hydroxide solution is prepared by mixing 85g of KOH in 1000ml of water. This temperature is similar to that used in HyET's factory baseline pre-treatment. The etching is done at 35°C for 3 minutes. The substrate is then cleaned with 1% H_3PO_4 at 70°C for 4 minutes to remove unwanted residues or by-product from the reaction.

An overview of the definition of etching experiments in shown in Figure 31.

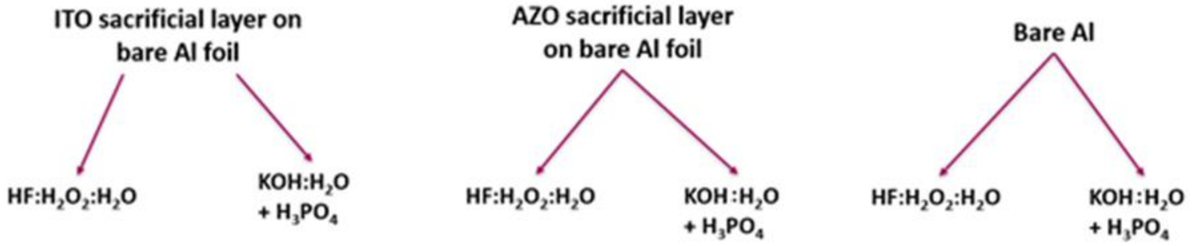

***Figure 31**: Definition of experiments for a combination of different substrates and etching recipes.*

Based on the results of the experiments carried out in Figure 31, it is found that ITO and AZO sacrificial layers are not contributing to the etching on the aluminium foil as it were on glass. Therefore, it is not justified to use AZO and ITO since it is an additional processing step for HyET which leads to longer processing time and higher costs.

Etching bare Al or Al with sacrificial layers with HF resulted in non-uniform and discontinuous craters as shown in Figure 32(a). The surface features also corresponded more to pyramids rather than U-shaped craters which are detrimental to nc-Si:H growth. Another drawback of HF is that it is a very dangerous acid and can present complications when introduced in HyET's R2R process. Etching with KOH produces uniformly distributed micro-sized craters as shown in Figure 32(b). This type of craters fits the criteria for good MST.

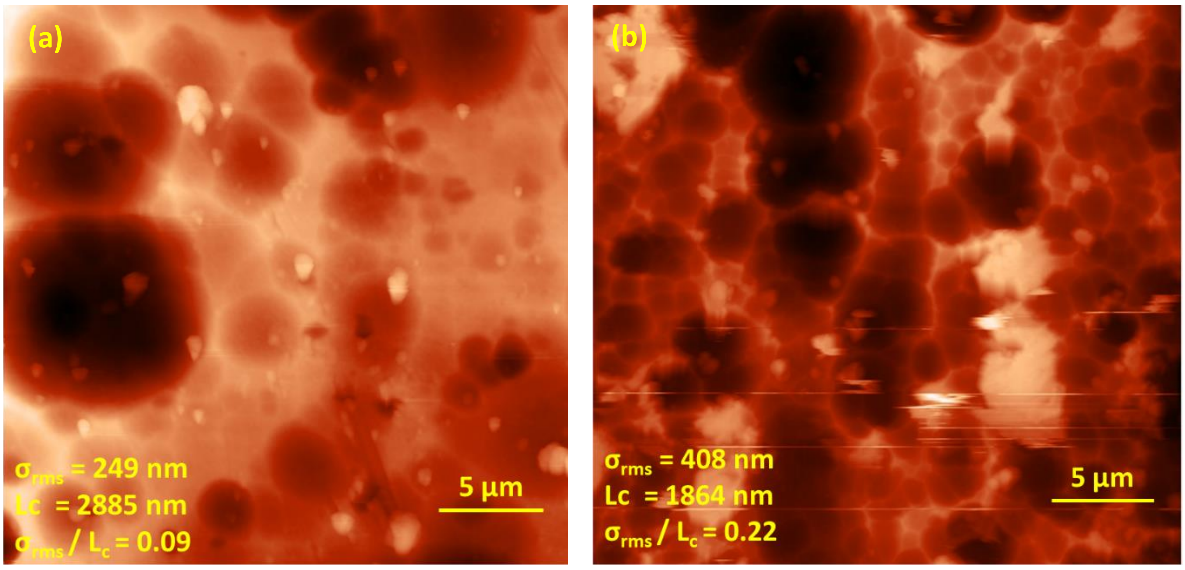

***Figure 32**: The surface features with HF etching at room temperature shows uneven and nonuniformly distributed craters with Lc = 2.885 µm, σ_{rms} = 249 nm and σ_{rms} /Lc = 0.09, (b) The surface features with KOH etching shows uniformly distributed craters with Lc = 1.864 µm, σ_{rms} = 408 nm and σ_{rms} /Lc = 0.22 [44].*

Based on these findings, etching with KOH is the best alternative because it results in uniformly distributed craters with better aspect ratios compared to HF. It is found that etching with KOH at 35°C yields too small crater sizes which are still not conducive to growth of high-quality nc-Si:H. Therefore, further etching experiments with KOH while varying the temperature and concentration is done to further optimize surface features. The best surface features are obtained with a concentration of 1.78M (100 g/L) at a temp. of 70°C for 2 minutes. Etching for more than 2 minutes makes surface features larger but makes the substrate thinner. This makes the foil more vulnerable to mechanical failure during the roll to roll process.

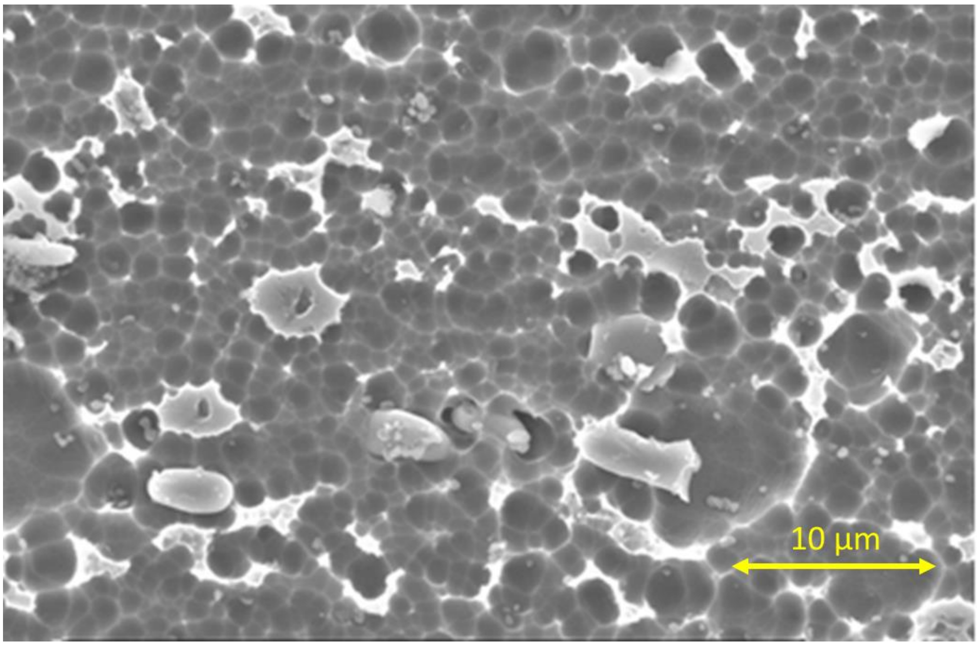

Figure 33: *The etching of bare Al with 1.52 M KOH at 35oC yields too small craters that is detrimental to the growth of good quality nc-Si:H [44].*

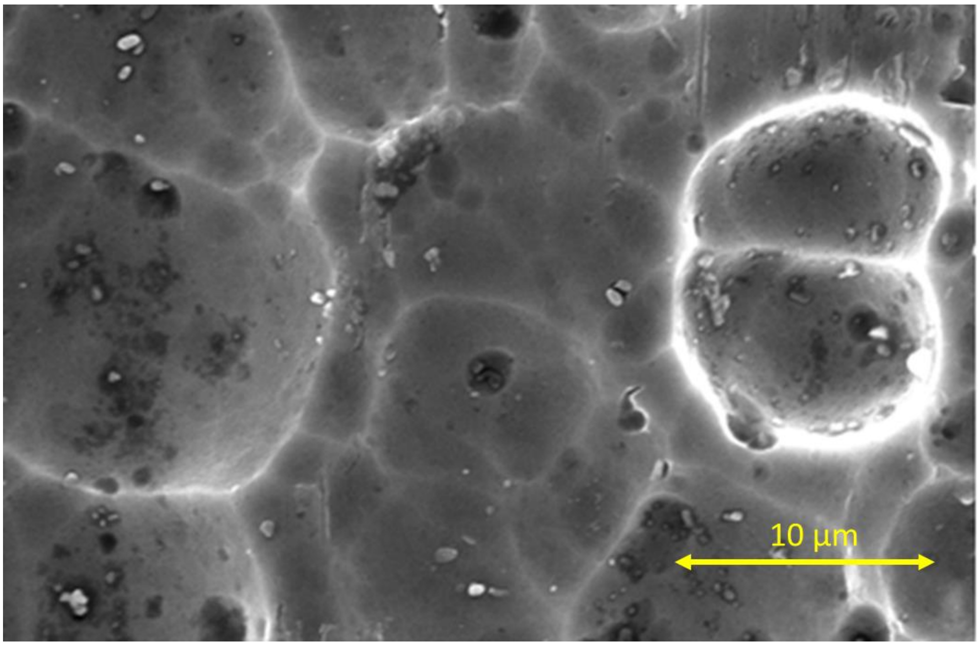

Figure 34: *Etching with 1.78M KOH at 70^{o}C for 2 minutes with shows better micro-sized craters which are suitable for growth of nc-Si:H [45].*

Surface features for the best etching recipe with KOH corresponding to Figure 34 result in approximate $L_c \approx 4$ µm, $\sigma_{rms} \approx 500$ nm, aspect ratio (σ_{rms}/L_c) ≈ 0.13 and average thickness of foil ≈ 80 µm. These values are in agreement with MST developed on glass for high quality nc-Si:H cells [22].

At HyET, the etching that is done to create the substrate textures is called the pre-treatment step. It is worth noting that HyET is currently using 0.1M NaOH at 35°C as their baseline pre-treatment. The drawback of etching with NaOH is that it is more aggressive as the substrate thickness reduces quicker compared to KOH for similar features [46]. The second is that etching with NaOH is less controllable with external factors compared to KOH [47]. Moving to the new pre-treatment with the best KOH recipe would bring advantages such as better light trapping and improved efficiency of modules.

However, this would also come at an additional cost to HyET. The alternative is to modify their existing etching recipe with NaOH by using higher temperature and concentration to produce better surface features. For these reasons, a new recipe with NaOH is implemented at HyET. This, however, is limited by the equipment in the R2R process. The factors which limit the R2R process are; (i) the speed of the machines which influence the etching time (time for which the moving foil is exposed to the etching solution), (ii) the final thickness of the foil after etching which should be above 95 µm, and (iii) the increased cost of implementing the new pre-treatment recipe which depends primarily on the new concentration of NaOH, and temperature. Based on these constraints, an etching recipe of 1.42M NaOH, at 50°C, for a time of 1.8 minutes is implemented at HyET. The morphology of surface features obtained at HyET with the new pre-treatment is shown in Figure 35. The new features are not as good as that exhibited by the best etching recipe with KOH, however, compared to the factory baseline (Figure 29) it is a great improvement.

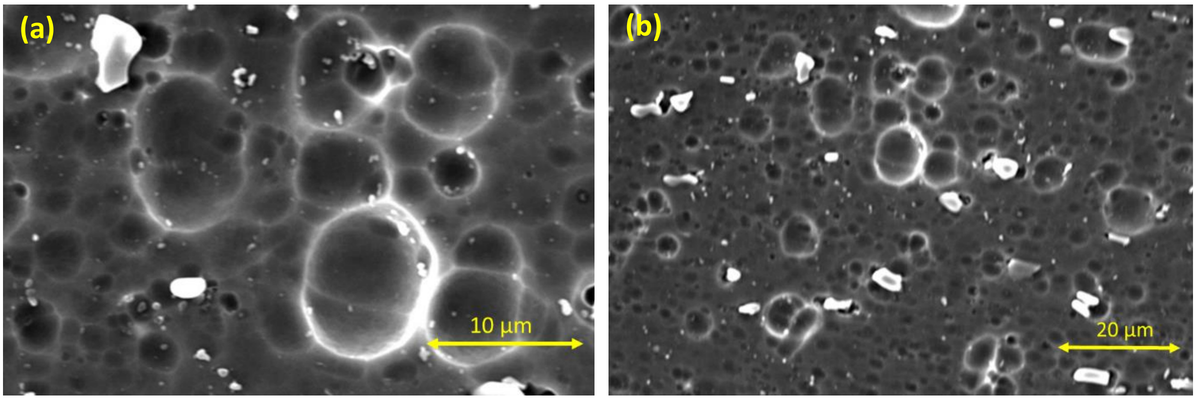

***Figure 35**: SEM images of new etching recipe implemented at HyET, (a) Craters formed are not uniformly distributed, (b) Same sample viewed under a wider area shows the etching is not uniform all over the sample when compared to best etching recipe with KOH [48].*

5.1.2 Growth of nanocrystalline silicon on MST based Al foil substrates

It should be noted that at this point, nc-Si:H has not been grown on Al foil substrates using MST. The end goal of the experiments is to finish the cells at HyET solar and test the I-V characteristics for important parameters such as $I_{sc}, V_{oc}, I_{mpp}, V_{mpp}, FF\ and\ \eta$. To provide a suitable starting point for the nc-Si:H depositions, a baseline recipe for growing the same on glass is used. The main aim is to develop a recipe for growing high quality nc-Si:H on Al foil.

The deposition parameters for the baseline nc-Si:H recipe on glass is shown below. The front TCO layer, which is AZO is deposited for 5400 s resulting in a thickness of approx. 700 nm. The p-nc-SiO$_x$:H and n-nc-SiO$_x$:H layers have a deposition time of 1800 s and 2740 s which results in a 48 nm p-layer and 98 nm n-layer, respectively. The i-layer consists of a seed layer deposited for 500 s with a silane concentration (S$_c$) of 1%, yielding a highly crystalline layer of thickness around 25 nm. For the main i-layer, a S$_c$ of 2.83% is used and deposition time of 5000 s corresponding to a thickness of approx. 2.3 µm. The estimated thicknesses are based on ellipsometry data for similar deposition parameters on glass and may differ on the Al foil. Aside from substrate effects, this can be due effects such as differences in the DC bias voltage of the Al foil and glass substrate inside the plasma chamber. The DC bias voltage determines the energy with which ions can bombard the substrate surface, thereby resulting in different growth characteristics [28].

***Table 2**: Deposition conditions ZnO:Al (Front TCO) layer for baseline recipe.*

	Pressure (mbar)	**Temperature (^oC)**	**Power (W)**	**Power per substrate area (W/cm^2)**	**Ar (sccm)**
AZO layer	2.6	300	300	3	20

***Table 3**: Deposition conditions for p- and n-layer for baseline recipe.*

	Pressure (mbar)	**Temperature (^oC)**	**Power (W)**	**Power per substrate area (W/cm^2)**	**SiH_4 (sccm)**	**H_2 (sccm)**	**B_2H_6 (sccm)**	**PH_3 (sccm)**	**CO_2/CH_4 (sccm)**
p-SiO_x-layer	2.2	300	12	0.12	0.8	170	10		1.6
n-SiO_x-layer	1.5	300	11	0.11	1	100		1.2	1.6

***Table 4**: Deposition conditions for seed layer and intrinsic layer for baseline recipe.*

	Pressure (mbar)	**Temperature (^oC)**	**Power (W)**	**Power per substrate area (W/cm^2)**	**SiH_4 (sccm)**	**H_2 (sccm)**
i-layer seed	4	180	40	0.4	1.2	120
i-layer	4	180	40	0.4	3.5	120

It is important to realise that the substrate type and morphology play a role in the growth of the nc-Si:H[18] and therefore, the deposition conditions may need to be varied from the baseline described above to produce the best quality nc-Si:H on Al foil.

5.1.3 Effect of different substrate morphologies on the properties of nc-Si:H

As explained in section 5.1.1, several textures were prepared using different etching solutions. The best micro-sized textures were achieved when etching bare Al substrate with 1.78M KOH at 70 °C for 2 mins. This is chosen solely based on the surface features and not on the quality of nc-Si:H grown on the substrate. Therefore, it is important to understand how different MSTs influence the growth of nc-Si:H. To analyse this, Raman spectroscopy is used to measure the spectra and determine crystalline fraction of layers deposited on different MSTs using the baseline deposition recipe described in section 5.1.2. The different etching recipes are used to create MSTs. Note that the MST is produced when the front TCO is grown on the textured substrate as shown in Figure 20. Since the TCO is the same, different MST are produced by varying the substrate textures. They are described below:

MST 1 – ITO sacrificial layer on Al substrate etched with 1:2:10 volumetric ratio of $HF:H_2O_2:H_2O$ at room temperature for 3 mins (ER1).

MST 2 – AZO sacrificial layer on Al substrate etched with 1.52M KOH at 35°C for 3 mins (ER2). The substrate is then cleaned with 1% H_3PO_4 at 70°C for 4 minutes to remove unwanted residues/by-products from the reaction.

MST 3 – AZO sacrificial layer on Al substrate etched similar to MST 2 but using 1.78M instead of 1.52M KOH. The substrate is then cleaned with 1% H_3PO_4 at 70°C for 4 minutes.

MST 4 – Bare Al etched with 1.78M KOH at a temp. of 70°C for 2 minutes. The substrate is then cleaned with 1% H_3PO_4 at 70°C for 4 minutes. This recipe produces best MST to date.

MST 5 – Bare Al etched with 1.78M KOH at a temp. of 70°C for 2 minutes. The substrate is not cleaned. The purpose of this experiment is to understand the effect of not removing the residues.

Table 5*: A description of the micro-sized surface textures prepared on different MST.*

	Description of features
MST 1	Large and small non-uniformly distributed craters
MST 2	Small uniformly distributed craters
MST 3	Small uniformly distributed craters
MST 4	Large uniformly distributed craters
MST 5	Large uniformly distributed craters

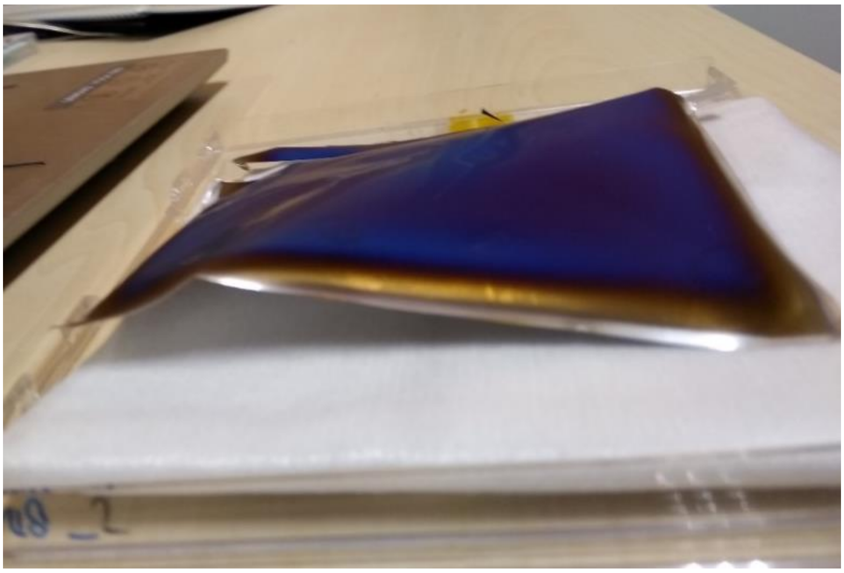

Figure 36*: First Substrate/TCO/p-i-n cell deposited in superstrate form on Al foil substrate.*

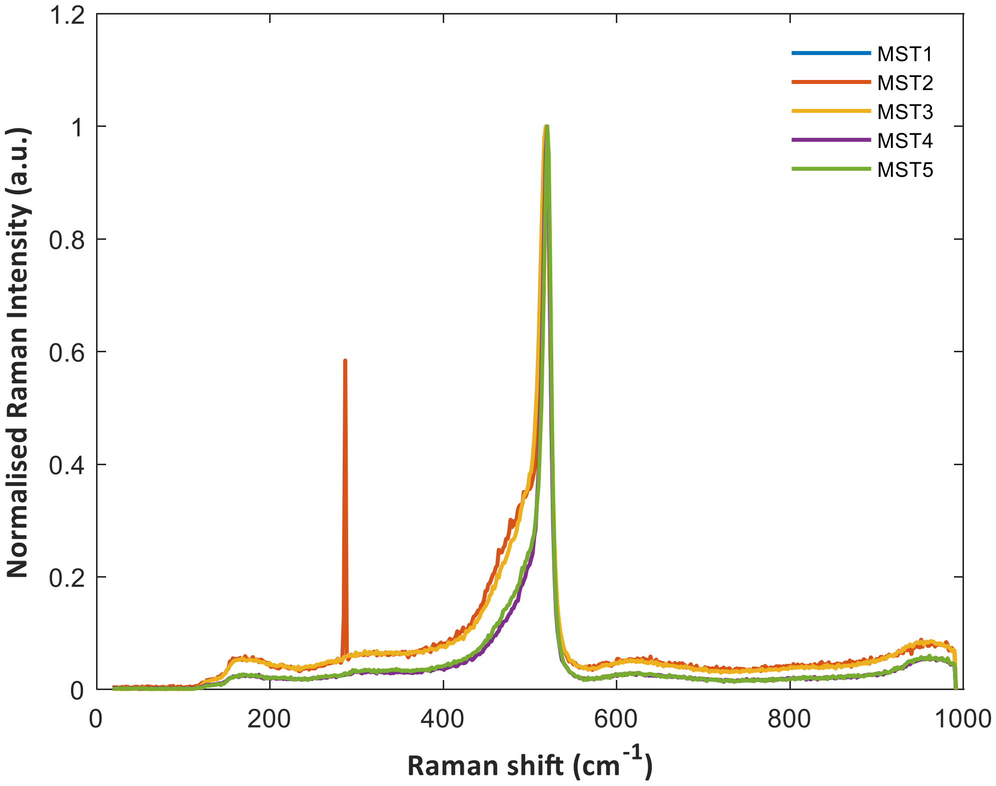

Figure 37*: Raman spectra of nc-Si:H grown on different substrate surface textures.*

From Figure 37 it can be observed that nc-Si:H material can be successfully grown on MST prepared on Al foil by using a standard deposition recipe on glass. It can also be observed from Figure 38 that the crystallinity is sensitive to the substrate textures. For MST 2 and MST 3, the amorphous shoulder is slightly higher compared to the others. This can be attributed to smaller craters formed on the substrate at 35°C which are less conducive to growth of nc-Si:H. This extends the amorphous incubation layer during the growth resulting in more amorphous tissue in the material. It also suggests that the standard seed layer must be altered on MST 2 and MST 3 to grow material with a higher crystalline fraction to decouple these substrate effects [18]. With MST 1, 4 and 5, high crystallinities are observed (MST 4 and 5 exhibit the best surface textures), cleaning the samples of residues after etching did not affect the crystalline fraction as much compared to the uncleaned sample.

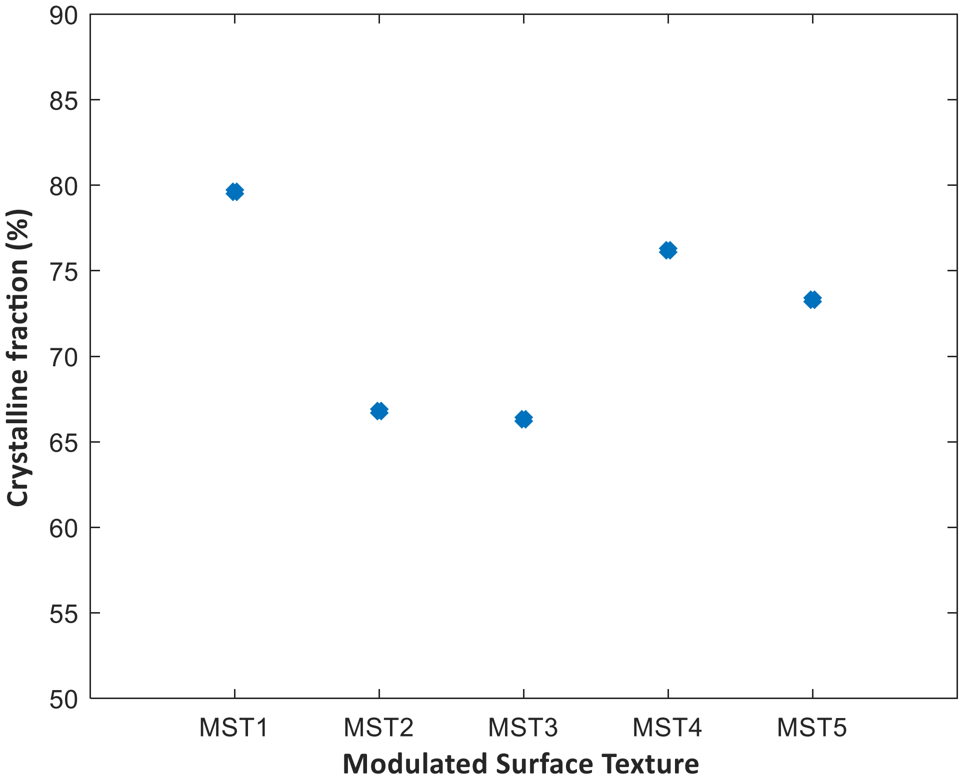

Figure 38*: Crystalline fractions for different MSTs. Similar deposition conditions for each cell were used with i-layer deposition time of 5000 s and expected thickness of 2.3 µm.*

The above experiment confirms that the etching recipe which gives best surface features (MST 4) also produce highly crystalline films that are desirable for nc-Si:H solar cells. This provides additional reasoning to proceed with MST 4.

5.1.4 Effect of residues and deposition time on crystallinity.

The etching process results in unwanted by-products or residues. To better understand the effect of cleaning the samples, a series of nc-Si:H cells are deposited on cleaned substrates prepared using MST 4. Similar deposition conditions to section 5.1.1 are used. Only the deposition time of the i-layer is varied from 5000 s to 15000 s. An uncleaned sample (MST 5) is also deposited for 5000 s as reference.

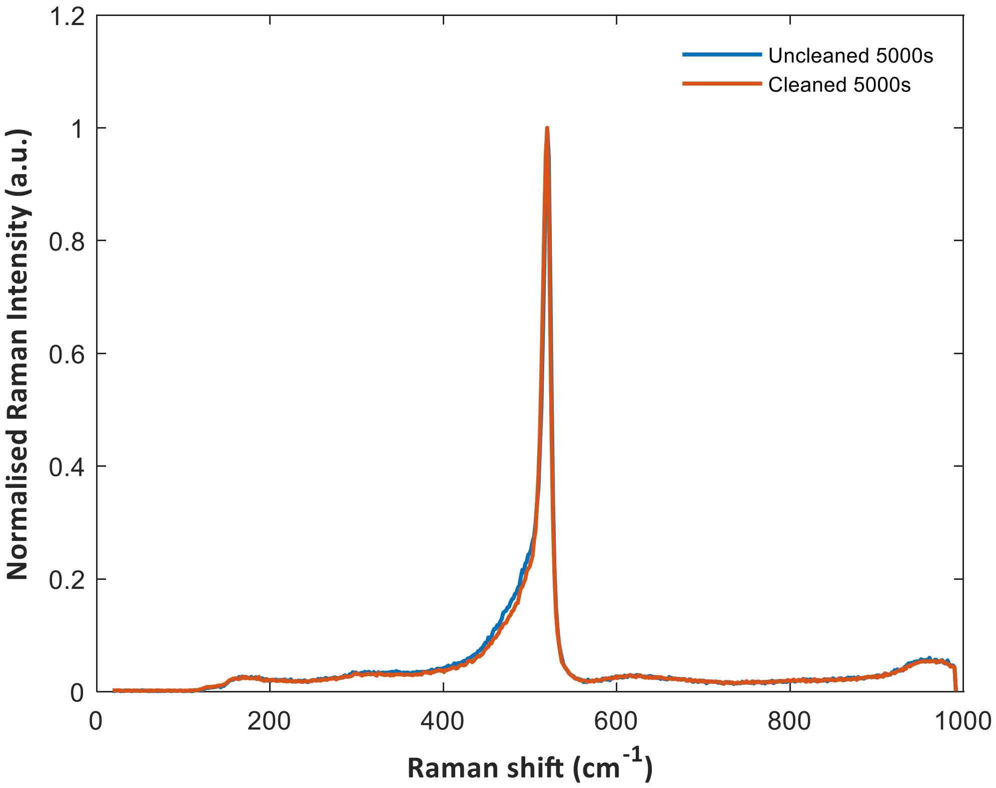

***Figure 39**: Raman spectra of nc-Si:H grown on uncleaned substrate and cleaned substrate.*

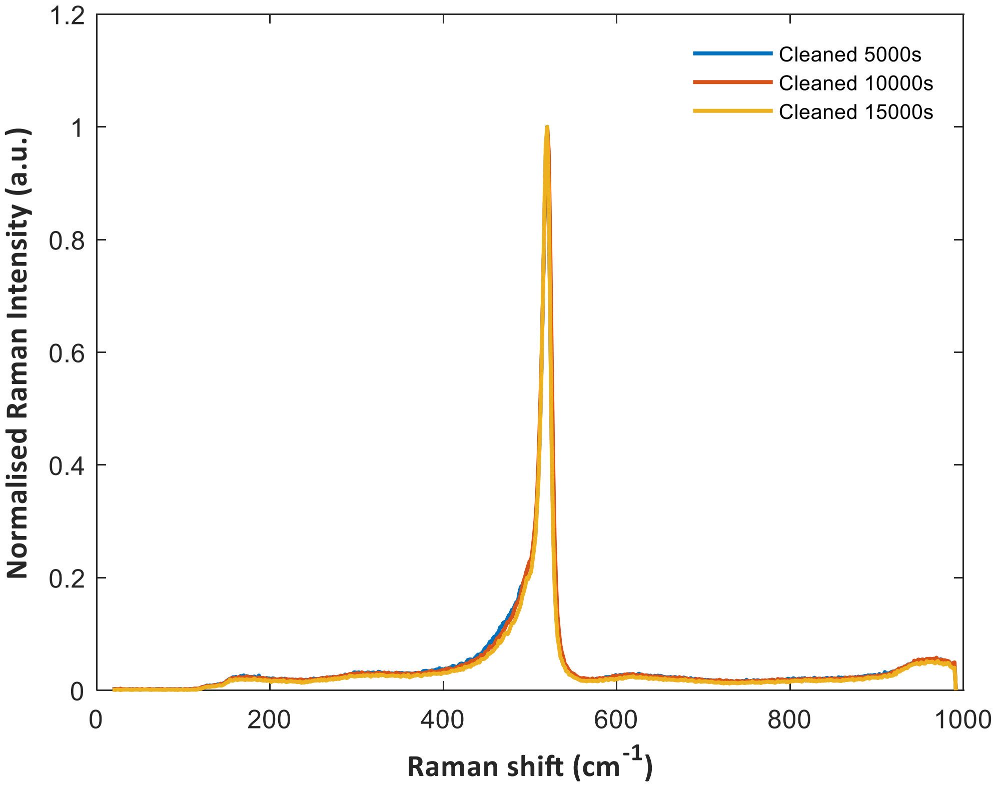

***Figure 40:** Raman spectra of nc-Si:H grown on cleaned substrates with increasing deposition times.*

From Figure 39, it can be observed that there is not much of difference in crystallinity when cleaning the sample, however, residues can create unwanted impurities in the solar cell layers resulting in poorly performing solar cells. Therefore, it is best to clean the samples before further processing. From Table 6, it can be understood that increasing the deposition time increases the crystallinity in the film as more crystalline grains are formed in relation to amorphous tissue. This increase could also be due to slight differences in the substrate textures as a result of the etching process. It may also indicate that the crystallization does not saturate at this particular silane concentration, even at thicknesses between 2 and 3 µm where single junction nc-Si:H solar cells show best performance. However, this should not be problematic as high efficiency nc-Si:H solar cells have been reported to have crystalline fractions between 65%[38] and 80% [21].

***Table 6**: Crystalline fractions for uncleaned and cleaned substrates. Similar deposition conditions for each cell were used with i-layer deposition time of 5000 s, 10000 s, 15000 s and corresponding thickness of 2.3 µm, 4.6 µm and 6.9 µm.*

	Crystalline fraction (%)
Uncleaned 5000 s	73.31
Cleaned 5000 s	76.64
Cleaned 10000 s	80.64
Cleaned 15000 s	82.06

5.1.5 Dark I-V characteristics

The process of finalizing the solar cell involves work to be carried out at HyET Solar. This entails; (i) the scribing of the TCO/p-i-n stack to define the cell area, (ii) sputtering of the ZnO:Al/Al back contact, (iii) laminating the permanent plastic carrier foil and finally (iv) removing of the aluminium substrate. At early stages it is important to investigate if all the layers have been deposited successfully without undertaking the cumbersome processing steps at HyET. A simple way of doing this is by measuring the dark I-V characteristics. Under non-illuminated conditions, a p-i-n cell should behave as a diode, the I-V curve can also be used to determine the series and shunt resistances which are important parameters in a solar cell.

To make this measurement, a metallic contact or TCO is deposited on the n-layer. In this case ITO squares (1x1 cm^2) are deposited on the rear. The cell is now in reverse stack order ITO/n-i-p/AZO/Al foil. The ITO will act as the front contact and the Al foil acts as the rear contact. This is shown in Figure 42(b).

The dark I-V characteristics can be measured using the WACOM. The curve of a measured cell is shown in Figure 41 confirms the diode behaviour of the p-i-n cell, the series resistivity is found to be 388 Ωm^2 and shunt resistivity is 1327 Ωm^2.

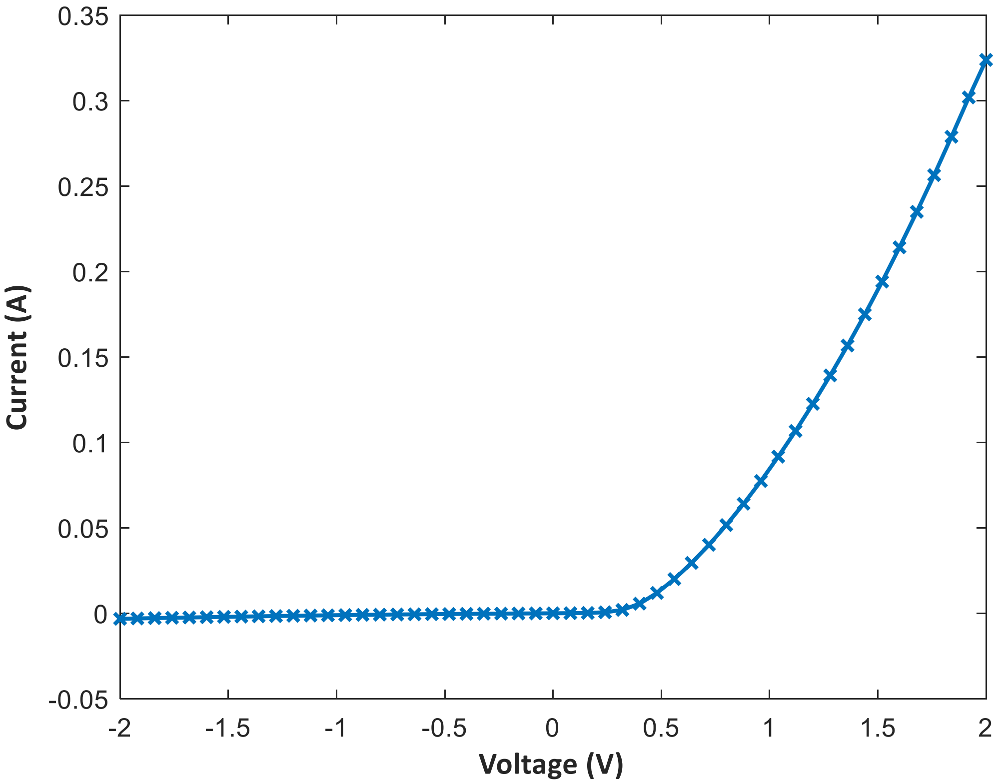

Figure 41*: Dark I-V characteristic of ITO/n-i-p/AZO/Al foil stack.*

The diode current is in the opposite direction of the photocurrent, as a result the series and shunt resistance may vary slightly under illumination. Another reason for deviation is that the diode current travels right through the contacts and spreads out into the solar cell, whereas under illumination, the photocurrent is generated in the bulk of the layers and get accumulated at the contacts and thus experience a higher series resistance. The values for series and shunt resistance are far from ideal, however, the importance of this experiment is that a working diode was produced using p-i-n nc-Si:H on Al foil substrate.

5.1.6 I-V characteristics under illumination of reverse configuration

It is interesting to measure the performance of the reverse configuration under illumination, although it is not the final deliverable of this thesis. However, it can be useful to understand some characteristics of the cell. The I-V curves are an indication of the quality of n-i and i-p interfaces, the substrate roughness, and the quality of the nc-Si:H grown on the substrate. The 1x1 cm^2 cells were measured under the AM1.5G spectrum with the ITO as top contact and the Al foil as the bottom contact as shown in Figure 42(a). The cell after depositing 300 nm of ITO is shown in Figure 42(b). The deposition of ITO is not uniform, which is aggravated by the fact the foil is curved due to inbuilt stress.

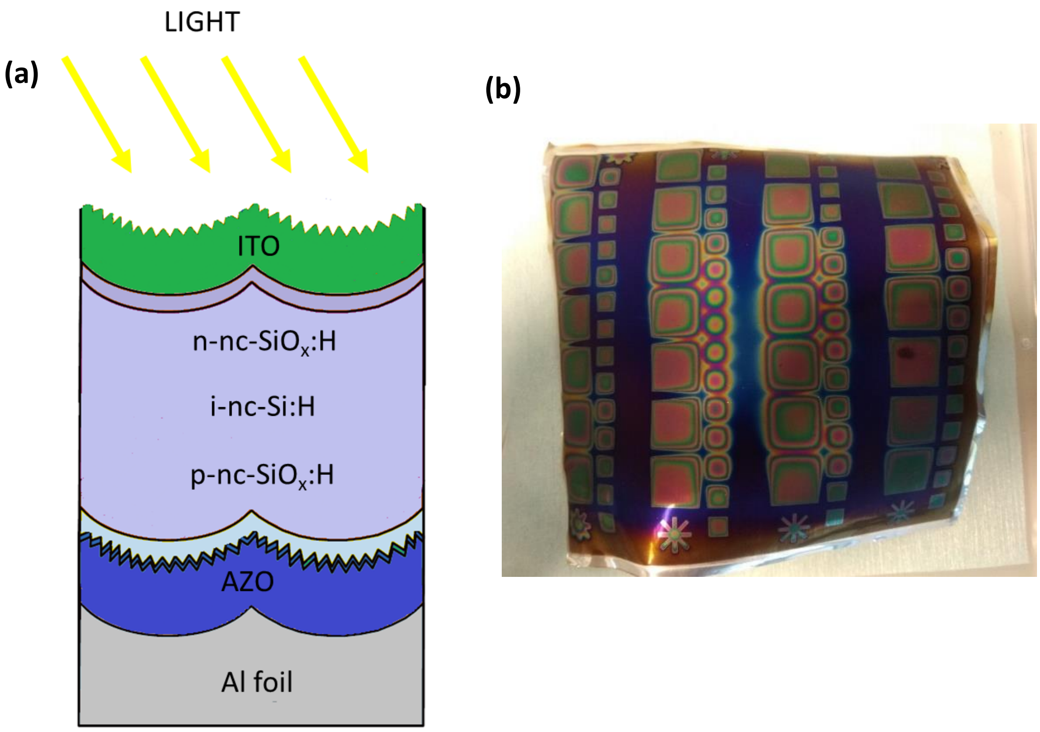

Figure 42*: (a) Solar cell stack as measured in reverse configuration under AM1.G spectrum, (b) The cell after depositing with ITO squares as front contact.*

Some of the I-V curves for two different samples are shown in Figure 43. The shapes of the curves vary between that of typical solar cells and resistive behaviour. The latter indicates that some of the cells are highly shunted which can also be the fault of the top contact probing through the ITO layer. The results are shown in Table 7 and compared to other nc-Si:H cells from literature. The efficiencies of tested cells vary between 1.19% and 2.65% and fill factor is extremely poor. Table 7 shows a comparison of the tested cells to some cells from literature. The experimental results are poor due to the following reasons:

- With solar cells deposited in n-i-p configuration, the n-layer is deposited first on the substrate followed by a seed layer which allows a good n-i interface. Furthermore, the delicate p-layer which is grown last is less influenced by the substrate textures and allows better controllability for a good p-i interface. In our p-i-n cells, efficiencies can be improved through a good p-i interface by optimising deposition conditions.
- In both n-i-p and p-i-n configurations, the p-layer is where the light enters the cell and not the n-layer as in the temporary configuration tested in Figure 42(a). The latter case results in additional recombination as holes travel a longer distance from the top of the cell to the p-layer. Furthermore, the n-layer which is 98 nm thick causes a drastic drop in blue light response.
- In the world record efficiency nc-Si:H cell, the front TCO consisting of BZO is grown using MOCVD to reduce plasma induced damage at the p-layer surface. An optimized honeycomb structure is implemented using photolithography. The inability to use these two techniques will of course act as limitations for reaching world record efficiencies in our single junction nc-Si:H solar cells.

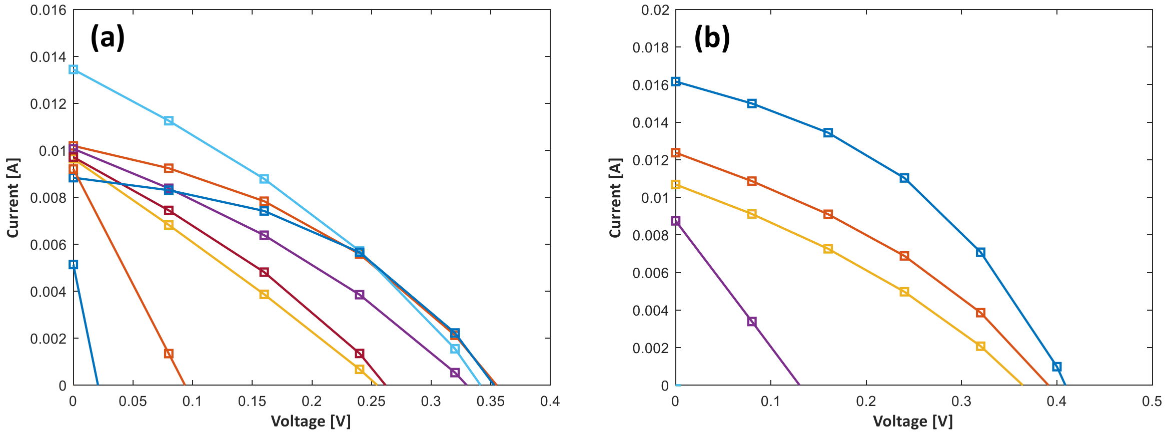

Figure 43: *J-V curves measured in the reverse configuration under AM1.5G.*

Table 7: *Parameters of measured J-V curves versus other state of the art nc-Si:H solar cells in literature.*

Parameter	**Reverse p-i-n on Al foil**	**n-i-p configuration on flat Al sheet [23]**	**p-i-n using MST on glass[22]**	**Best on glass substrate (n-i-p) [21]**
V_{oc} (V)	0.36 – 0.409	0.382	0.552	0.548
J_{sc} (mA/cm^2)	10.68 – 16.16	23.9	25.6	29.4
FF (%)	31 - 40	54	72.6	73
Efficiency (%)	1.19 – 2.65	4.9	10.2	11.8
Thickness (μm)	2.3	4	3	2

Higher efficiencies can be achieved by completing the solar cell at HyET. In the final cell, the light will shine through the p-layer as shown in Figure 18 resulting in better values of V_{oc}, J_{sc} and efficiency. Additional performance can be gained by implementing the following:

- Using optimized MST to obtain high quality nc-Si:H growth with no cracks resulting in less shunts and high FF/V_{oc}.
- Using a seed layer following the p-layer to obtain a good p-i interface that can result in higher V_{oc}, J_{sc} and/or FF.
- Optimize the material properties such as crystallinity and stretching mode signature to obtain high quality nc-Si:H intrinsic layer.
- Optimize p- and n-layer thicknesses and opto-electrical properties to maximize efficiency.
- Optimize front TCO layer thickness to improve optical coupling into the cell while maintaining decent electrical properties.
- Optimize the thickness of nc-Si:H i-layer on MST.
- Optimize other deposition parameters such as power and pressure to grow high quality nc-Si:H cell at higher deposition rates.

5.1.7 The effect of changing silane concentration on properties of nc-Si:H

The silane concentration (S_c) is an indication of the amount of silane relative to hydrogen in the deposition chamber. As discussed in section 3.5 and section 4.1, S_c affects the crystalline properties of the material. A lower S_c implies that there is more hydrogen which favours crystallization resulting in higher crystalline material. At higher $S_{c,}$ more silane is present which enhances amorphous silicon growth. It is found that with decreasing silane concentration there is a reduction in the deposition rates as less silane is available for growth of silicon layers [18]. In order to transfer the lab scale growth of nc-Si:H into large scale deployment at HyET, it is important to understand how the S_c affects the crystallinity, quality of the material and deposition rates on Al substrates.

The experiment is undertaken by varying the hydrogen flow of the i-layer between 60 sccm and 130 sccm. The silane flow is kept constant at 3.5 sccm similar to the baseline deposition recipe described in section 5.1.2. The S_c is therefore varied between 2.62% and 5.15% as shown in Table 8. The deposition conditions are similar to those given in Table 2, Table 3 and Table 4 with an i-layer deposition time of 5000 seconds. However, no n-layer is deposited to avoid interference with Raman measurement. The substrate texturing used in all the experiments is MST 4. The red and green laser is used to analyse the homogeneity of the crystalline fraction throughout the depth of the cell. The results are shown in Figure 44.

***Table 8**: Silane concentration and corresponding flows for hydrogen and silane. $X_{c,\ green}$ and $X_{c,\ red}$ refers to crystalline fraction measured with the green and red laser, respectively.*

No.	i-layer Hydrogen flow (sccm)	i-layer Silane flow (sccm)	i-layer Silane concentration (%)	$X_{c,\ green}$ (%)	$X_{c,\ red}$ (%)
1	130	3.5	2.62	78	62
2	125	3.5	2.72	60	62
3	120	3.5	2.83	76	78
4	115	3.5	2.95	82	83
5	110	3.5	3.08	64	66
6	105	3.5	3.23	67	71
7	95	3.5	3.55	76	82
8	80	3.5	4.19	23	14
9	60	3.5	5.51	53	56

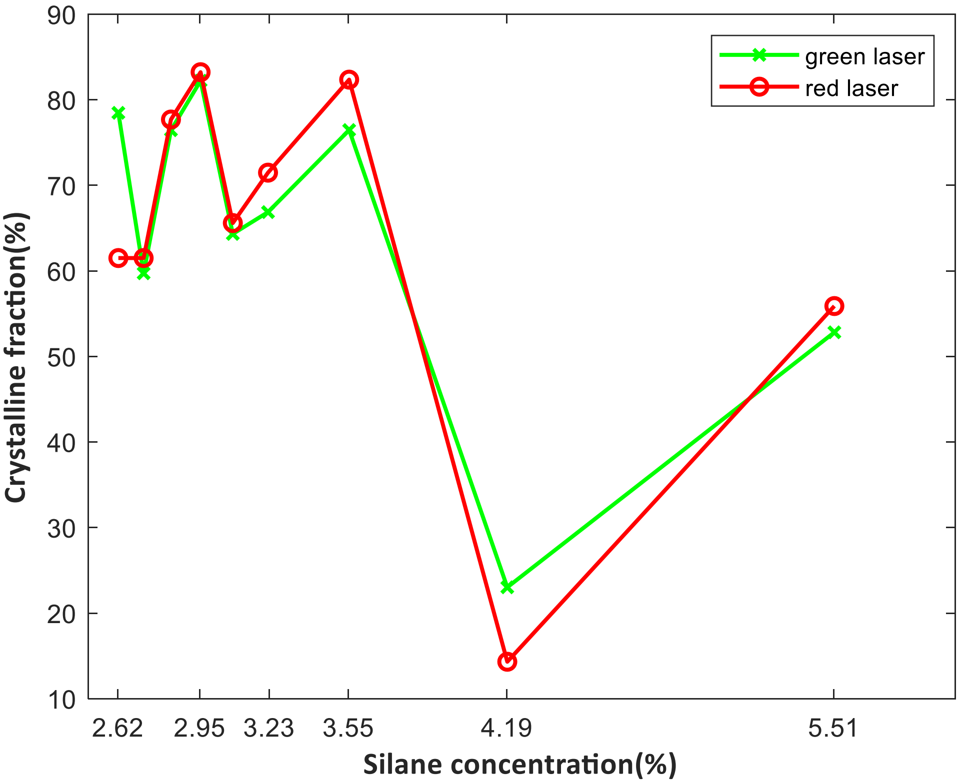

***Figure 44**: Variation of crystalline fraction with silane concentration.*

The results show a significant inconstancy in the crystalline fraction as the silane concentration changes. According to theory, one would expect the crystalline fraction to reduce with increasing silane concentration. The crystallinity is quite uniform in depth at silane concentrations between 2.72% and 3.08% as shown by the closeness of the red and green lines, however, at higher silane concentrations it is not the case. The reason for this is not quite clear as for an S_c = 3.55%, the red laser shows a higher crystalline fraction than the green laser, this is counterintuitive as one would expect the crystallinity to be higher towards the end of the deposition rather than at the beginning as crystallization continues to develop during the deposition.

There are several reasons for the irregular variation in the crystalline fraction:

1. The MST is prepared by etching at specific temperature, time, and concentration of etchant. These three factors are susceptible to issues of reproducibility. These slight changes in substrate textures can influence the initial growth of the material and affect the crystallinity. As observed in the section 5.1.3, Figure 38 shows different MSTs yielded a crystalline fraction between 66% and 80% under the same deposition conditions.

2. The load and tune of the PECVD tool are dependent on the flows of the hydrogen and silane for a fixed power and pressure. Changing the flows from the baseline recipe without optimizing the load and tune values can result in an unstable plasma which may not result in the exact H_α to Si^* atom ratio available for deposition [17]. This can lead to lower or higher crystallization than expected based on the composition of the plasma. It should also be noted that the PECVD tool does have reproducibility issues, this diagnosis is outside the scope of the thesis project, however, this can only be seldom expected.

3. The seed layer used is similar for all the experiments. The seed layer consists of a highly crystalline layer of 25 nm deposited for 500 seconds with $S_c = 1\%$, which is grown between the p- and i-layer. The same seed layer may not be conducive for growth of an i-layer deposited with any value of S_c. It is suggested that a seed layer deposited while varying the silane concentration from a low value to required final S_c is more favourable to growing nc-Si:H with certain crystalline fraction [49].

In addition, the following differences can be observed between glass and Al substrates:

- There is no clear-cut decreasing trend in the crystalline fraction with increased silane concentration on aluminium unlike in glass [18].
- Very high crystallinities are obtained on aluminium compared to glass substrates over a much wider range of silane concentration [18].

This can be attributed to a possible catalysing effect of aluminium substrates on nanocrystalline silicon growth [50].

5.1.8 Analysis of the Raman spectra in the normal and extended range

To understand the nature of the nc-Si:H material grown under varying silane concentration, the Raman spectra shown in Figure 45 to Figure 48 can be analysed. From the normal range, it is observed that the spectra for $S_c = 4.19\%$ ($H_2 = 80$ sccm) is fully amorphous while for $S_c = 5.51\%$ ($H_2 = 60$ sccm) is partly crystalline; this indicates that something may have gone wrong in the tool during deposition. Looking at the spectra in the extended range, the curves are compared with those of high quality nc-Si:H hydride (Si-H_x) stretching mode (SM) signatures shown in Figure 26. From Figure 47, $S_c = 2.95\%$ (H_2 = 115 sccm) and $S_c = 3.23\%$ ($H_2 = 105$ sccm) shows a good SM signature with the green laser. However, for $S_c = 3.23\%$, a non-ideal red laser signature is observed from Figure 48, this indicates that material properties are non-homogeneous throughout the layer.

From Figure 47, for S_c = 5.51, 3.08 and 2.72 %, the signature seems to have a significant contribution from a-Si:H tissue in the bulk as observed by both the single peak around 2030 cm^{-1} in the extended range and also the shoulder at 480 cm^{-1} in the normal range. It can be deduced that a poor signature with only a single peak around 2030 cm^{-1} and no peak at around 2100 cm^{-1} corresponds to less crystalline material (crystalline fraction below 70%). The good signature with both peaks visible showing thickness homogeneity (similar red and green signature) is synonymous with a high crystalline fraction greater than 80%, this is true for $S_c = 2.95\%$ ($H_2 = 115$ sccm).

It can also be observed that material growth is not consistent. Taking a simple example, from Figure 47, $S_c = 3.23\%$ ($H_2 = 105$ sccm) shows a good nc-Si:H signature with the green laser but shows an amorphous signature with the red laser, this shows that crystallisation is stronger towards the end of the deposition than in the bulk. Whereas for 2.72 % ($H_2 = 125$ sccm), an amorphous signature is shown with the green laser but a good nc-Si:H signature is shown with red laser, this shows that crystallisation in stronger in bulk than towards the end. This indicates varying growth properties as one would expect the material to continue crystallising rather than become more amorphous as the deposition progresses. This suggests that some external process parameters such as power, pressure, load and tune values may need to be optimised to ensure growth properties remain constant. Therefore, merely changing the silane concentration may be inadequate.

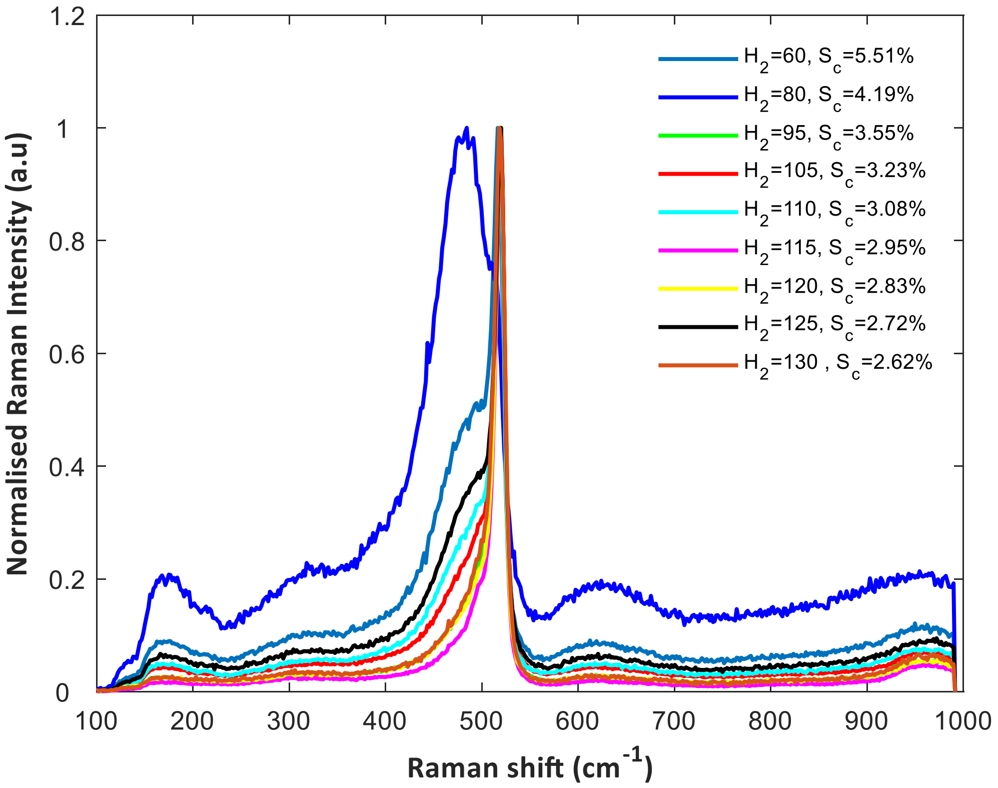

***Figure 45**: Effect of changing silane concentration on the Raman spectra as measured under the green laser.*

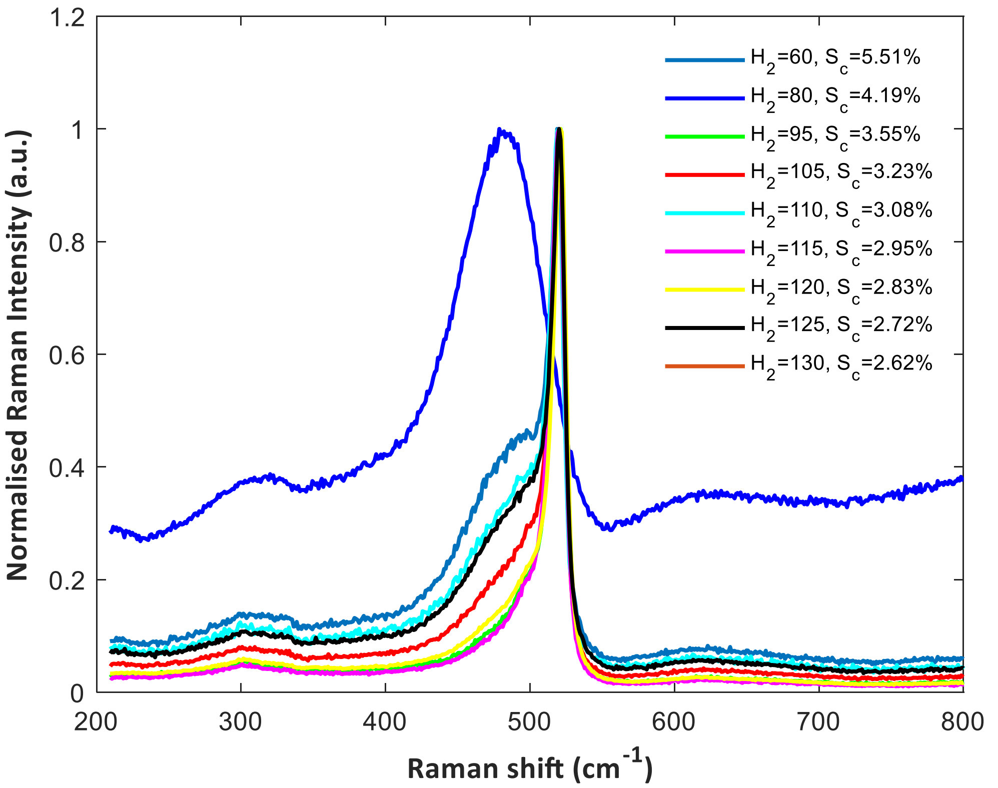

***Figure 46**:Effect of changing silane concentration on the Raman spectra as measured under the red laser.*

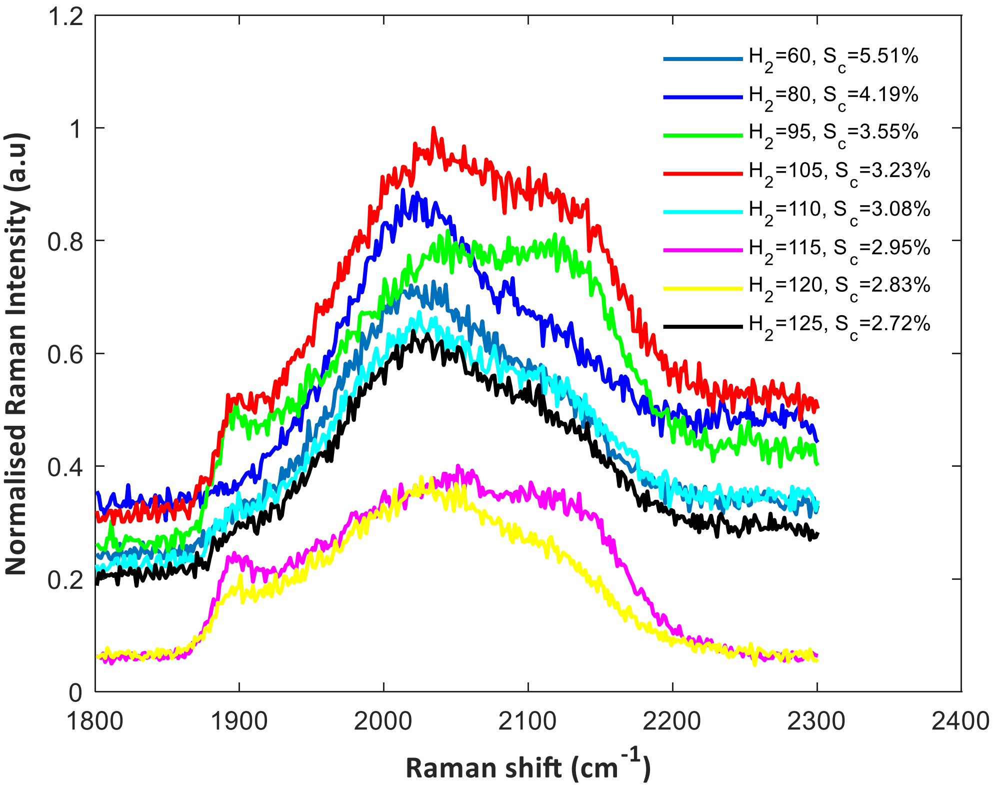

Figure 47*: Effect of changing silane concentration on the Raman spectra in the extended range as measured under the green laser.*

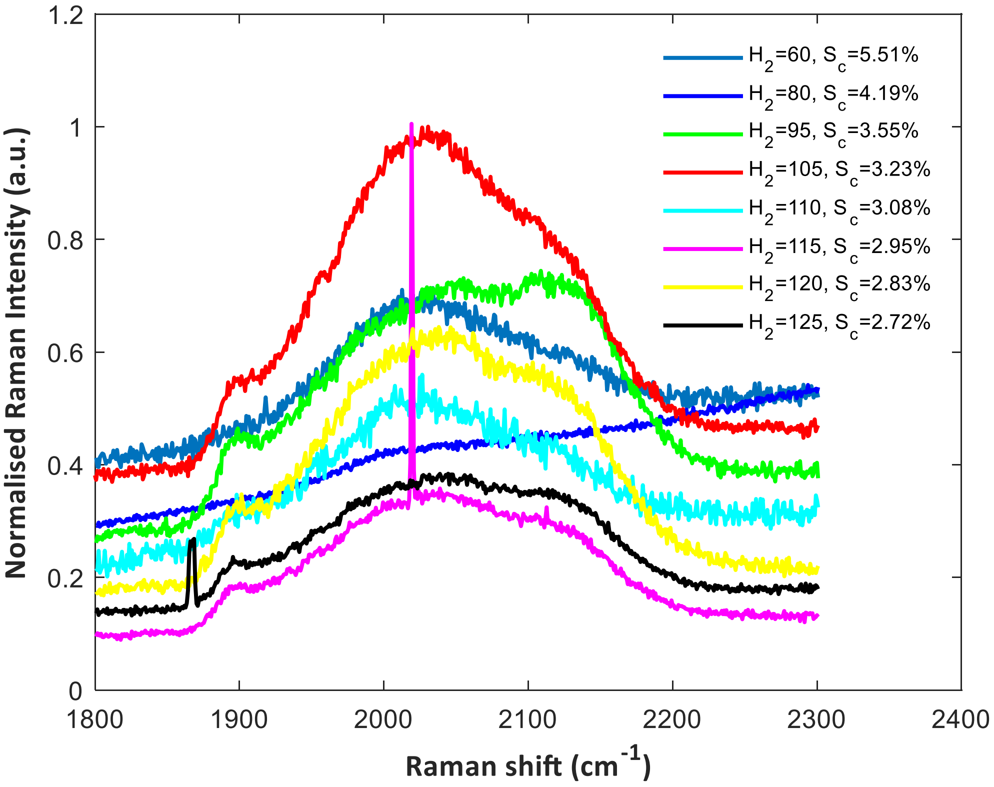

Figure 48*: Effect of changing silane concentration on the Raman spectra in the extended range as measured under the red laser.*

For the fixed deposition conditions, it can be concluded that $S_c = 2.95\%$ ($H_2 = 115$ sccm) shows a good signature with both the red and green laser implying that the nature of material is homogenous throughout the layer. On the other hand, $S_c = 2.83\%$ ($H_2 = 120$ sccm) and $S_c = 2.72\%$ ($H_2 = 125$ sccm) also show very good signatures, however, only observed with the red laser. The discrepancy between red and green signatures hints that the baseline seed layer may not be conducive to growing homogeneous material at $S_c = 2.83\%$ and $S_c = 2.72\%$. Therefore, moving forward it is important to test nc-Si:H cells in the range of $2.72\% <= S_c <= 2.95\%$ ($115 \text{ sccm} <= H_2 <= 125 \text{ sccm}$) for the given deposition power and pressure. Using a silane concentration beyond this range would require these parameters to be optimised.

5.1.9 Measuring the deposition rates

Deposition rates vary with changing silane concentration for fixed power, pressure, and gas flows. These parameters are important to understand when upscaling to large area production where higher deposition rates in excess of 1 nm/s are required to reduce time and cost. As discussed earlier, ellipsometry cannot be used to determine the thickness, therefore we shall have to depend on SEM analysis. In the previous chapter, experiments were undertaken by changing the silane concentration of the i-layer while keeping the deposition time constant. The deposition rate is then evaluated by dividing the i-layer thickness by the deposition time. Some of the SEM images used for this purpose are shown in Figure 49 below.

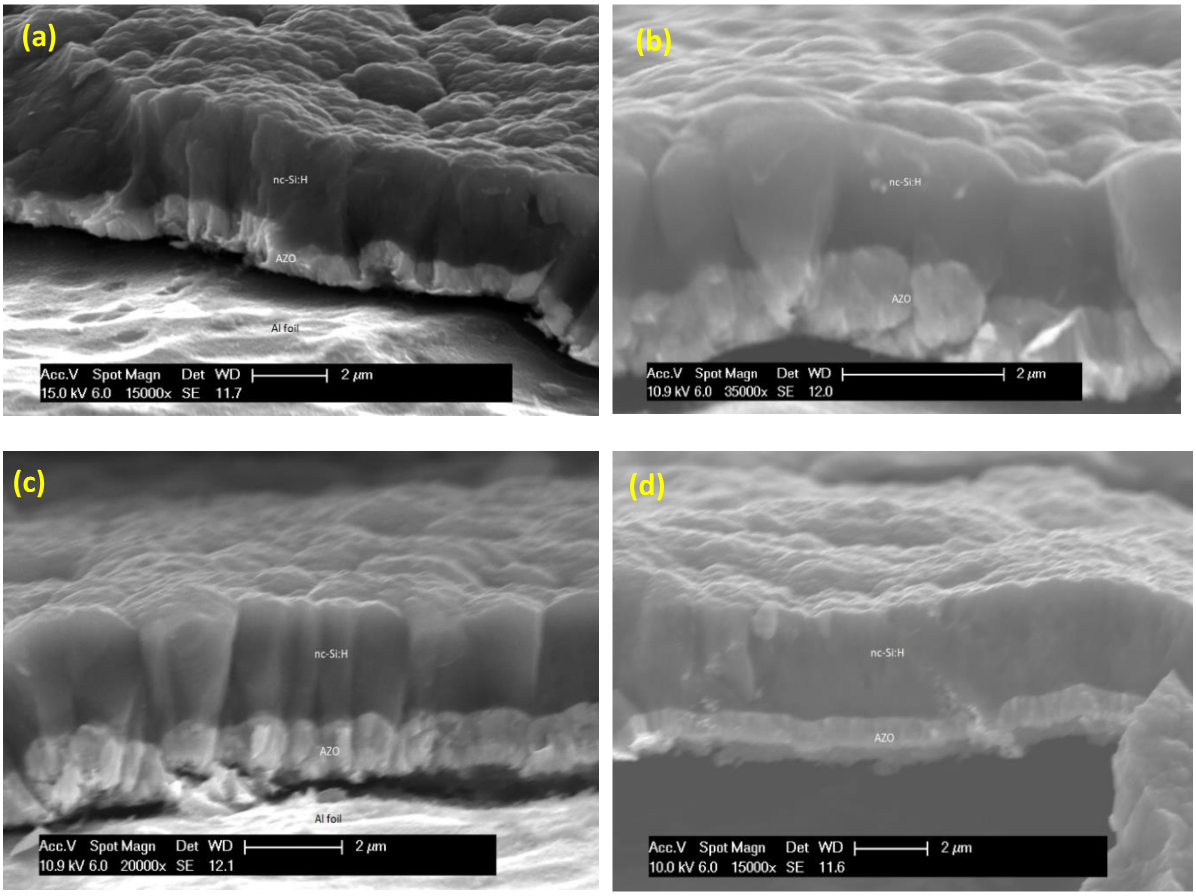

Figure 49*: Some of the cross-section SEM images used to determine deposition rates. (a) $S_c = 5.51\%$, $H_2 = 60$ sccm, (b) $S_c = 4.19\%$, $H_2 = 80$ sccm, (c) $S_c = 3.08\%$, $H_2 = 110$ sccm, and (d) $S_c = 2.62\%$, $H_2 = 130$ sccm.*

It is interesting to observe from Figure 49(b), that a hydrogen flow of 80 sccm or $S_c = 4.19\%$ should have resulted in thickness above 2 µm, however the image shows a thinner layer. This further confirms that something went wrong during the deposition which resulted in a thick amorphous layer as observed earlier in Figure 45. This is a classic example of reproducibility issues encountered with the PECVD tool.

The deposition rates for different S_c are calculated and plotted in Figure 50 below. The deposition rates vary irregularly with S_c. Possible explanations for the variation can be:

- The thickness of the i-layer also includes a 48 nm p-layer. There is no way to distinguish these very thin layers in the SEM, therefore the i-layer thickness includes the p-layer as well.
- It is difficult to determine from the SEM image whether the measurement is made perpendicular to the substrate surface. This is because the Al foil is bent by nature, therefore some measurement error can be expected.
- There seems to be no correlation between the crystalline fraction and the silane concentration, it may indicate that random crystallisation on the substrate is leading to different deposition rates.

From the results it can be concluded that for S_c between 2.72% and 2.95% which is the range for optimal nc-Si:H growth, the deposition rate is between 0.46 and 0.48 nm/s. A higher deposition rate of 1 nm/s can be obtained using a high pressure & high power, also known as the high pressure depletion regime [18]. However, further enhancement of the deposition rate is not in the scope of this thesis. In addition, knowing the deposition rate enables us to make thickness series of nc-Si:H solar cells which is used to optimize the thickness of the cell with regards to performance.

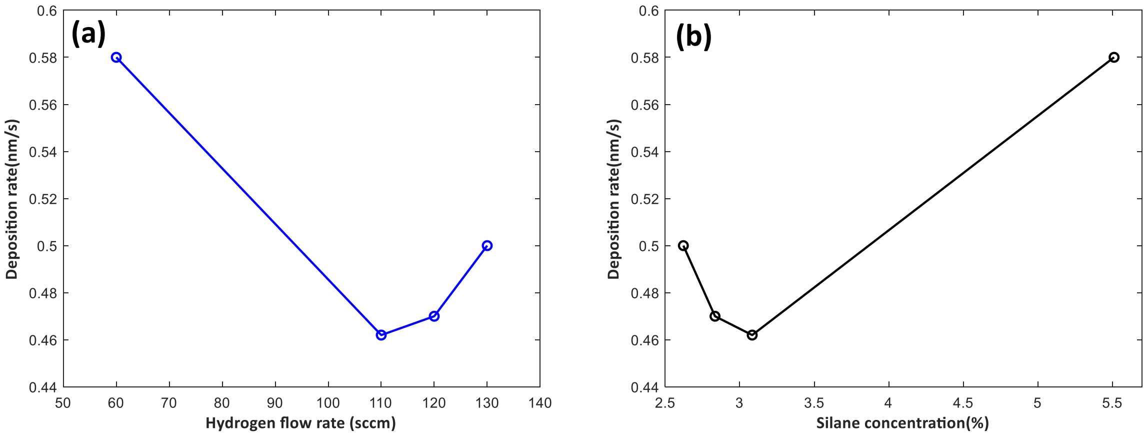

***Figure 50**: Variation of depostion rate with (a)hydrogen flow rate, (b) silane concentration.*

5.1.10 Thickness series with best signature in extended range

From the previous experiment in section 5.1.8, it is found that a S_c of 2.95% with hydrogen flow of 115 sccm and silane flow of 3.5 sccm results in the best hydride stretching mode signature and also exhibit good thickness homogeneity. In order to further understand the growth of layers, a thickness series is done with the same S_c. The i-layer deposition time (based on the deposition rate) is varied to produce corresponding thicknesses of 1.5, 2 and 3 µm. In all 3 experiments, all other deposition parameters are similar to Table 2, Table 3 and Table 4. The results are shown in Figure 51. The baseline 2.3 µm refers to the sample deposited with S_c = 2.95% (H_2 = 115 sccm) from the experiment discussed in section 5.1.8. The value X_c refers to the crystalline fraction. Some sharp peaks are also observed in the spectra which appear to be random noise in the measurement and can be ignored from the analysis.

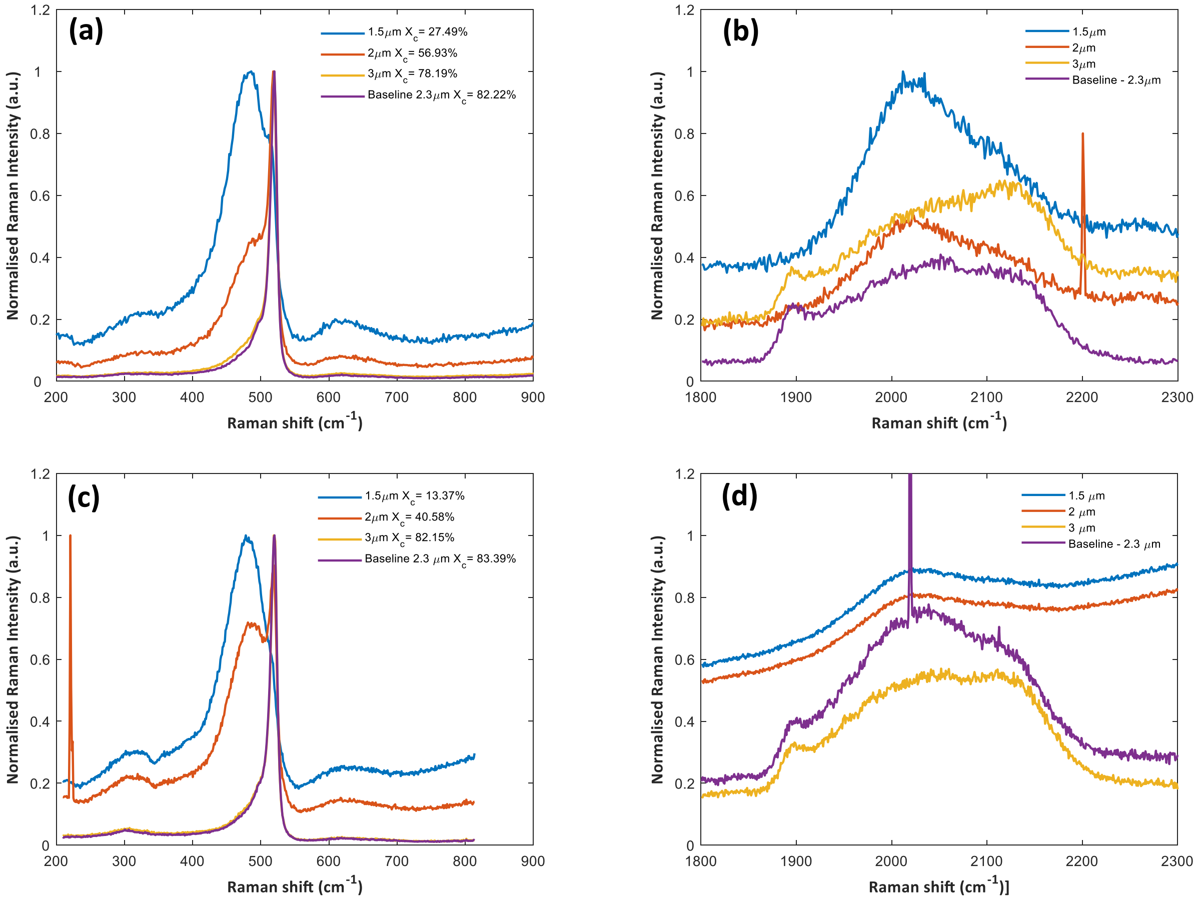

***Figure 51**: Raman spectroscopy undertaken for thickness series with S_c = 2.95%, H_2 = 115 sccm, (a) Green laser normal range, (b) Green laser extended range, (c) Red laser normal range, (d) Red laser extended range.*

Figure 51(a) and (c) show that at 1.5 µm, the layers are highly amorphous. At 2 µm, the peak at 520 cm^{-1} is observed which indicates that nanocrystalline material has begun to form. At 3 µm, the spectrum corresponds to a similar shape and crystalline fraction as in the baseline sample of 2.3 µm. In the extended range, the green laser signature for 1.5 µm and 2 µm corresponds to that of increased amorphous tissue in the bulk as deduced in section 5.1.8, whereas the 3 µm corresponds to an increased contribution of di- and tri-hydrides without much a-Si:H tissue to passivate the pores and crystalline grain surfaces [38]. However, with the red laser, the 3 µm sample shows a very good signature. The red laser extended signature for 1.5 µm and 2 µm shows abnormal results for which the reason is unclear. Again we observe the material does not exhibit thickness homogeneity and the results were not reproducible from section 5.1.8 with S_c = 2.95%, (H_2 = 115 sccm).

From these findings, the following can be concluded:

- The growth of the material in the first 1.5 µm is not crystalline. This implies that the material only starts crystallizing between 1.5 and 2 µm. This is problematic for nc-Si:H solar cells as the incubation layer should be as small as possible, typically within the first 25-50 nm. Thicker incubation layers can result in a poorly performing solar cell as the amorphous fraction is too high [6].
- The 25 nm seed layer with S_c = 1% deposited for 500 seconds, used in the baseline recipe may not be conducive to crystallization from the onset of growth. A good seed layer should be tuned to the substrate type, substrate textures and final silane concentration in the i-layer [49].

- If we assume that all the depositions took place in a similar manner, then it can be deduced that the red laser does not pick up a significant amorphous portion of the material at 3 µm as is observed at 1.5 µm and 2 µm.

5.1.11 Optimizing the seed layer using silane concentration grading (graded seed layers)

The seed layer forms an integral part of the development of a p-i-n nc-Si:H solar cell. When grown in the superstrate configuration, it serves as a good p-i interface, while in the substrate configuration it serves as a good n-i interface. Moreover, it improves the microstructure homogeneity of the i-layers which has led to increase in FF and J_{sc} in solar cells [51]. From literature it is known that substrates like glass and aluminium give rise to an amorphous incubation layer. This layer can be significantly thick as it was found in section 5.1.10 and detrimental to solar cell performance. Although a seed layer was used in previous experiments, it was not effective. Seed layers can also be incorporated into the p- or n-layers, however, for the purpose of this thesis, the two will be considered independently.

Studies have shown two main effects; (i) when doped layers are also used as seed layers their inherent crystalline fraction can determine the crystallinity of the i-layer[51], and (ii) substrate features can influence the crystallinity [49]. A third possibility is also the influence of the sharp textures of the TCO on the crystallinity of subsequent layers. Therefore, it is important to know beforehand that these factors play a role in determining the crystallinity of the i-layer. While the MST features can vary slightly due to variable etching conditions and the p-layer crystallinity is kept the same, the seed layer can be used to mitigate the effect of the substrate, p-layer microstructure and TCO features on crystallinity of the i-layer. Studies have shown that a good seed layer can almost decouple the dependence of the structural composition of the i-layer from the effects of the underlying layers [18].

A possible solution would be to implement a seed layer at lower silane concentration, for example S_c = 0.4% deposited for 500 seconds instead of the baseline S_c = 1%. However, it has been shown that at such low S_c, the thickness homogeneity cannot be maintained due to edge effects and furthermore, the results are not easily reproducible [49]. On the other hand, it has been found that highly crystalline and homogenously thick seed layers of 10-20 nm can be developed using silane concentration grading [49]. This process involves the gradual increase of the silane concentration from a fraction of the desired value to the final value. It has been found that initial S_c values between 10% and 50% of the final S_c can yield highly crystalline material within a thickness of 20 nm [49].

In this experiment, the silane concentration of the i-layer ($S_{c,\ Final}$) is chosen to be 3%. Note that this value of S_c is outside the optimal range found in section 5.1.8. Five different seed layers are deposited for 500 seconds, with initial silane concentration ranging from 10% to 40% of the final silane concentration ($0.1{*}S_{c,\ Final}$ to $0.4{*}S_{c,\ Final}$). In addition, one seed layer with initial $S_c = 0.1{*}S_{c,\ Final}$ is deposited for 250 seconds. For each deposition, the silane concentration was increased in discrete steps of 50 seconds from initial S_c to final S_c. In all the experiments MST 4 was used to prepare textures on Al foil, on which a 700 nm AZO was deposited followed by a p-layer of 48 nm as per the baseline recipe.

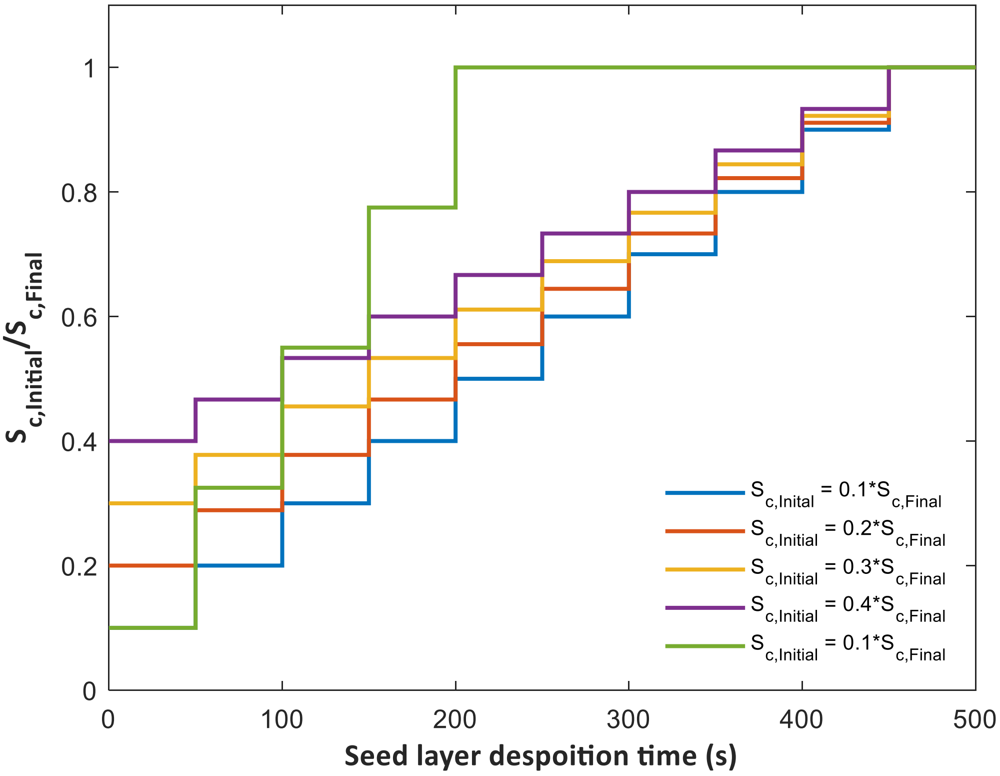

Figure 52: The seed layer is deposited for 500 seconds with different initial silane concentration varied in discrete steps of 50 seconds.

The results of the Raman spectra are shown in Figure 53, both the green and red laser was used to measure the spectra and the thickness of the films are estimated to be under 100 nm. Highly crystalline material above 64% was obtained with all seeds deposited for 500 seconds, whereas the seed deposited for 250 seconds was slightly more amorphous at 61%. From Figure 54, the red laser shows higher crystallinity than the green laser which implies higher crystallization at the start of nucleation due to lower silane concentration.

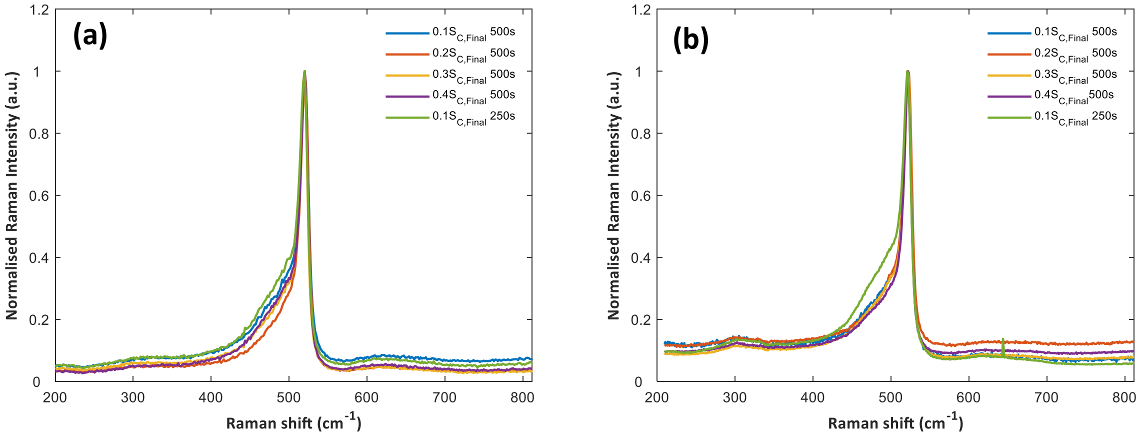

***Figure 53:** Raman spectra for seed layers deposited for 500 seconds and 250 seconds using silane concentration grading (a) green laser spectrum, (b) red laser spectrum.*

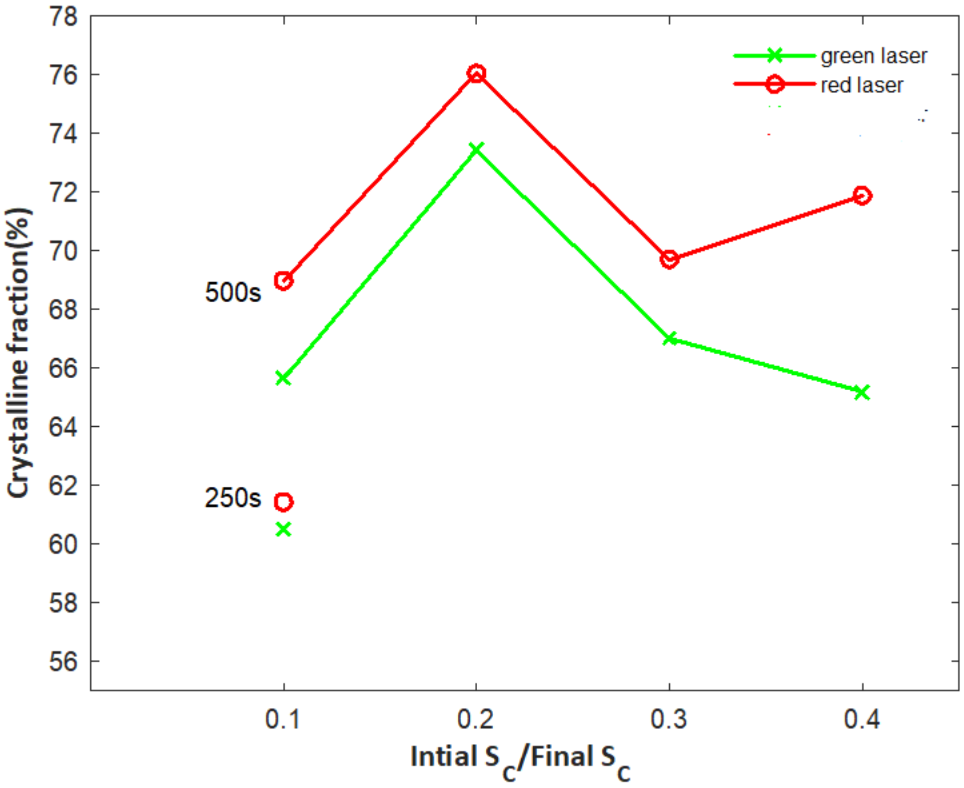

Figure 54: The variation of crystalline fraction when using different initial silane concentrations in the seed layer grading technique

In the extended range, very good hydride stretching mode signatures were obtained for all seed layers deposited for 500 seconds as shown in Figure 55. It should also be noted that the measurement noise with the red laser is much higher than the green laser. The red laser which probes deeper into the seed layer already shows good signatures; this is indicative of high quality nanocrystalline silicon material being grown from the onset of deposition. The consistency of the signature in the green laser shows good microstructure homogeneity in the growth direction has been maintained. The seed layer can be expected to transition better into the main i-layer while maintaining the desired properties of high quality nc-Si:H material. As a result, a good p-i interface can be expected. A favourable result is therefore obtained with a silane concentration of 3% using this grading technique, whereas the optimum S_c from previous experiment in section 5.1.7 with ungraded seed is found to be between 2.72% and 2.95%. This implies that the seed layer may have suppressed any underlying effects on crystallinity. It can be concluded that the graded seed layer tuned to the required final S_c is more effective in growing nc-Si:H, i-layer compared to the ungraded seed layer. Regardless of all the seed layers showing very good signatures, the $S_{c,\ Initial} = 0.2*S_{c,\ Final}$ shows the best signature in the extended range with both red and green laser, in addition to showing high crystallinity over 72%. It should be noted that in Figure 55(b), for $S_{c,\ Initial} = 0.3*S_{c,\ Final}$ the red laser signature is distorted, however the green laser signature looks very good. This could be just a measurement error, or it could mean that the material is poorly formed and too amorphous at the start.

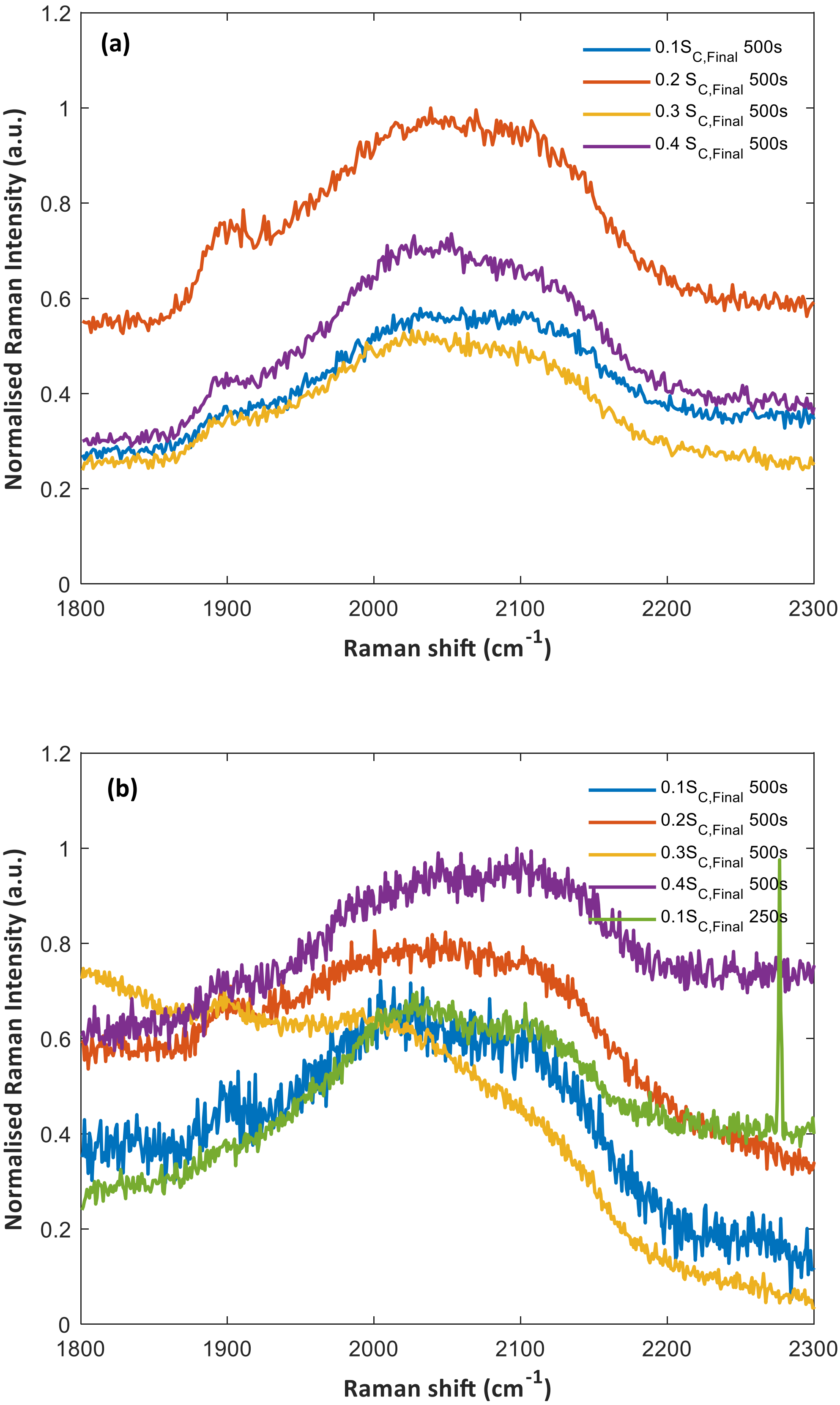

***Figure 55**: Raman spectra for seed layers deposited for 500 s using silane concentration grading measured in the extended range using (a) the green laser, (b) red laser.*

5.1.12 Ungraded seed layer vs. graded seed layer

A comparison between the ungraded seed layer (baseline seed layer) and graded seed layer can be made using Raman spectroscopy to understand why the latter is conducive to growth of higher quality nc-Si:H. Two seed layers were deposited for 500 seconds. The ungraded seed layer is made with S_c = 1% corresponding to hydrogen flow of 120 sccm and silane flow of 1.2 sccm as per the baseline recipe (Table 4). The graded seed layer is made from $S_{c,\ Initial}$ = 0.6% (0.2*$S_{c,\ Final}$) to $S_{c,\ Final}$ = 3% in steps of 50 seconds. In both experiments, MST 4 was used to prepare textures on Al foil, on which a 700 nm AZO was deposited followed by a p-layer of 48 nm as per the baseline recipe. The results are shown in Figure 56 below.

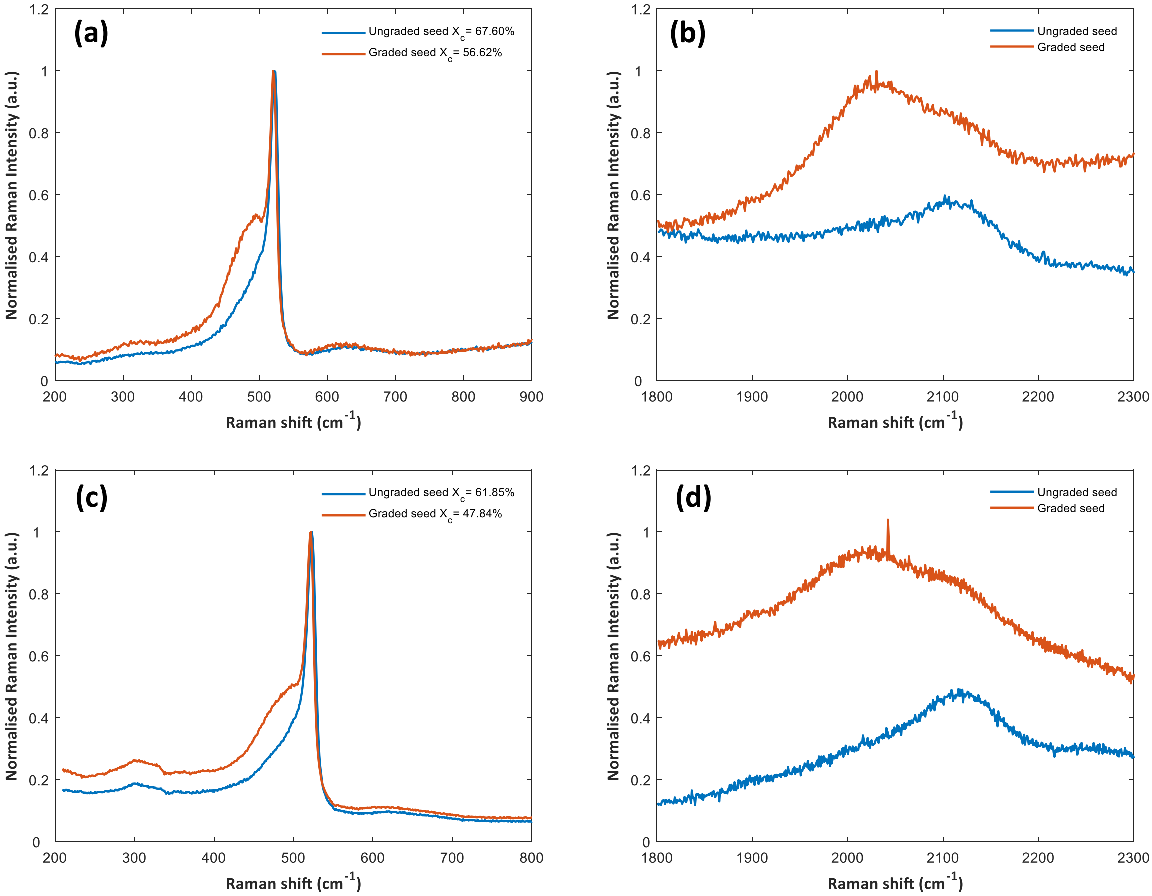

Figure 56: Raman spectra of the ungraded and graded seed layers as observed with (a) green laser normal range, (b) green laser extended range, (c) red laser normal range, (d) red laser extended range.

The spectra in the normal range show that the ungraded seed layer is highly crystalline, but the graded seed is slightly amorphous. The crystallinity for the graded seed was not reproducible from the previous experiment, even though all deposition conditions remained the same. This could be a reproducibility issue with the PECVD tool. The spectra in the extended range, however, shows a different story since the signature of the ungraded seed is far from desired. Figure 56(b) and (d), the ungraded seed (blue curve) shows no peak at 2030 cm^{-1}and only a single peak at around 2100 cm^{-1}. This signature is representative of a dominance of mono-, di-, and trihydrides on crystalline surfaces and di- and tri-hydrides in the bulk of nc-Si:H. It is also representative of less dense material with high crystallinity, and a lack of a-Si:H tissue to passivate crystalline grain boundaries and pores [38]. It is also reflective of the hydrogen rich plasma that is used to speed up nucleation which results in a defective p-i interface that leads to poor carrier collection [52] and results in lowest performing solar cells [53].

For the graded seed (red curve), the red and green laser results show that both the peaks at around 2030 cm^{-1} and 2100 cm^{-1} have started to form. This signature is representative of a denser bulk matrix and a reduction in di- and tri-hydrides, hinting at the reduced hydrogenated crystalline grain boundaries in the pore network [38]. In addition to the good signatures from section 5.1.11, this further confirms that the graded seeds can produce device grade (high quality) nc-Si:H from the onset of the growth regardless of a slightly higher amorphous fraction. In addition, the transition of silane concentration from a low to a high value in the graded seed can result in a better p-i interface as the microstructure evolves smoothly without an abrupt change unlike in the ungraded seed as shown in Figure 57 below.

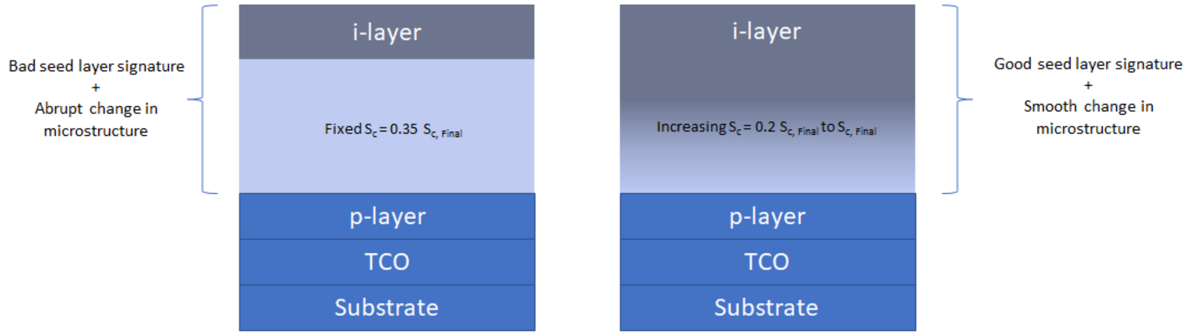

Figure 57*: A schematic comparison of the ungraded seed layer (left) against the graded seed layer (right).*

Figure 58 shows the Raman spectra of an i-layer with S_c = 2.83% deposited on the same graded seed layer for 5000 s. The similarity of the spectra with the green and red laser in the normal range as well as the signatures in the extended range shows very good thickness homogeneity in the growth direction. Notice that the i-layer S_c = 2.83% is less than $S_{c,\ Final}$ = 3% of the graded seed, this implies that slightly overshooting the silane concentration during seed layer deposition may be favourable to the growth of main nc-Si:H i-layer. Very high crystallinities of over 80% were achieved using this technique, these values correspond to crystalline fractions in high efficiency solar cells over 11% [21]. In addition to exhibiting very good SM signatures, very high short circuit currents can be expected from these p-i-n cells.

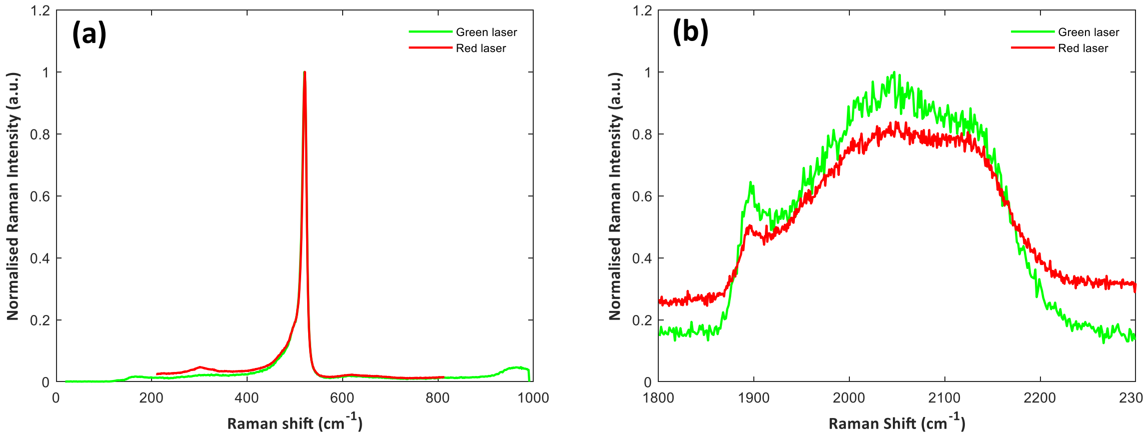

Figure 58*: Raman spectra of 5000 s i-layer deposited with Sc = 2.83% using graded seed in (a) Normal range, (b) Extended range*

Figure 59 shows an SEM image of the i-layer deposited in the above experiment. No cracks can be observed which indicates high quality nc-Si:H material is grown that in addition to high crystallinities, using graded seed layers. Some residual particles are also observed which is most likely due to the cutting of the samples.

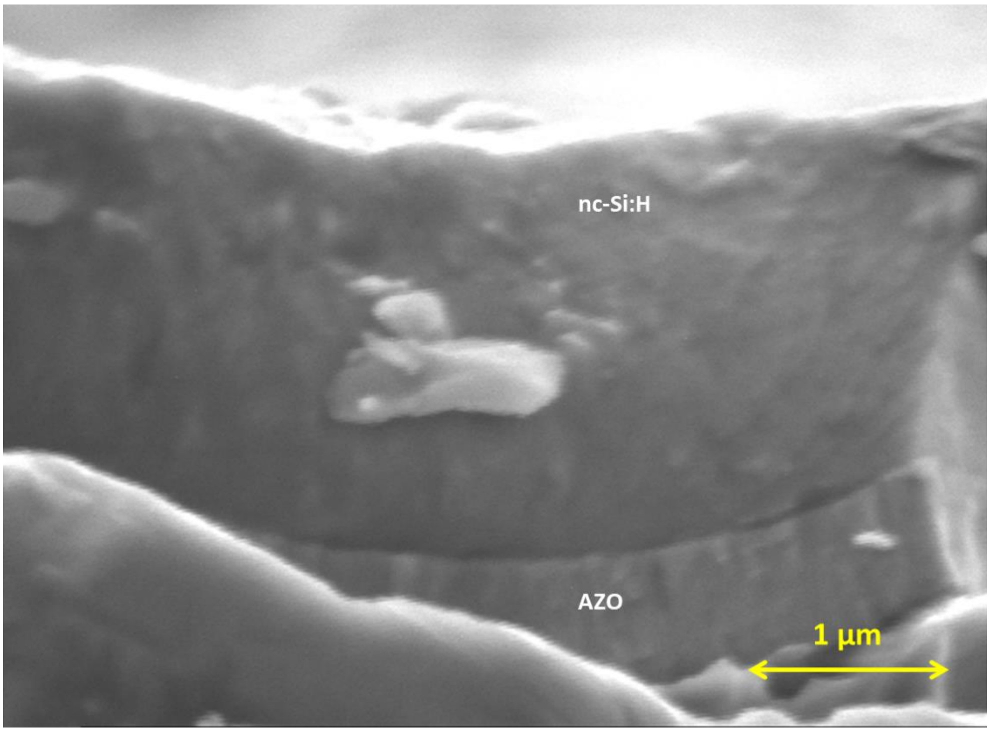

***Figure 59**: SEM image of nc-SI:H grown on graded seed layer with $S_{c,\ Final}$ = 3% and main i-layer S_c = 2.83%*

5.1.13 Use of different S_c with graded seed layers

Three different p-i-n cells are deposited with $S_{c,\ Final}$ = 2.68% (H_2 = 120 sccm and SiH_4 = 3.3 sccm), $S_{C,\ Final}$ = 2.83% (H_2 = 120 sccm and SiH_4 = 3.5 sccm) and with $S_{c,\ Final}$ = 2.95% (H_2 = 115 sccm and SiH_4 = 3.5 sccm). In all 3 depositions, MST 4 is used to prepare the substrate textures, a 700 nm AZO layer is deposited followed by a 25 nm p-layer. The p-layer is changed from 48 nm from the baseline recipe to 25 nm to reduce parasitic absorption and increase short wavelength response in the working solar cell. A graded seed layer tuned to $S_{c,\ Final}$ is deposited for 500 seconds starting at 20 % of the final silane concentration, this initial value is based on the optimal signature from Figure 55. Following the seed layer, a 5000 seconds deposition of the main i-layer with $S_{c,\ Final}$ is made. Finally, an n-layer of 25 nm is deposited as opposed to the 98 nm layer in the baseline recipe. The new experimental details are tabulated in below.

***Table 9**: Deposition parameters for ZnO:Al (TCO) layer in PECVD tool.*

	Pressure (mbar)	**Temperature (^oC)**	**Power (W)**	**Power per substrate area (W/cm^2)**	**Ar (sccm)**
AZO layer	2.6	300	300	3	20

***Table 10**: Deposition parameters for p and n-layer in PECVD tool, p-layer deposited for 900 s and n-layer deposited for 1500 s to produce thickness of 25 nm for both layers.*

	Pressure (mbar)	**Temperature (°C)**	**Power (W)**	**Power per substrate area (W/cm^2)**	**SiH_4 (sccm)**	**H_2 (sccm)**	**B_2H_6 (sccm)**	**PH_3 (sccm)**	**CO_2/CH_4 (sccm)**
p-SiO_x:H-layer	2.2	300	12	0.12	0.8	170	10		1.6
n-SiO_x :H-layer	1.6	300	11	0.11	2	120		0.8	0.8

***Table 11**: Deposition parameters for seed layer and intrinsic layer in PECVD tool.*

	Pressure (mbar)	**Temperature (°C)**	**Power (W)**	**Power per substrate area (W/cm^2)**
Graded seed	4	180	40	0.4
i-layer	4	180	40	0.4

The results are shown in Figure 60 below. The spectra in the normal range shows high crystallinity with good thickness homogeneity. The same can be said about the signature in the extended range. An anomaly for the extended range of $S_{c,\ Final}$ = 2.68% shows that the signature is not reproducible with the red laser. This signature with a single peak at around 2100 cm^{-1} is representative of a high dilution with hydrogen, with significant contribution of di- and tri-hydrides in the bulk as discussed previously. This is detrimental to solar cell performance. This could also possibly be due to a measurement error in the Raman Spectrometer or reproducibility issues in the PECVD tool.

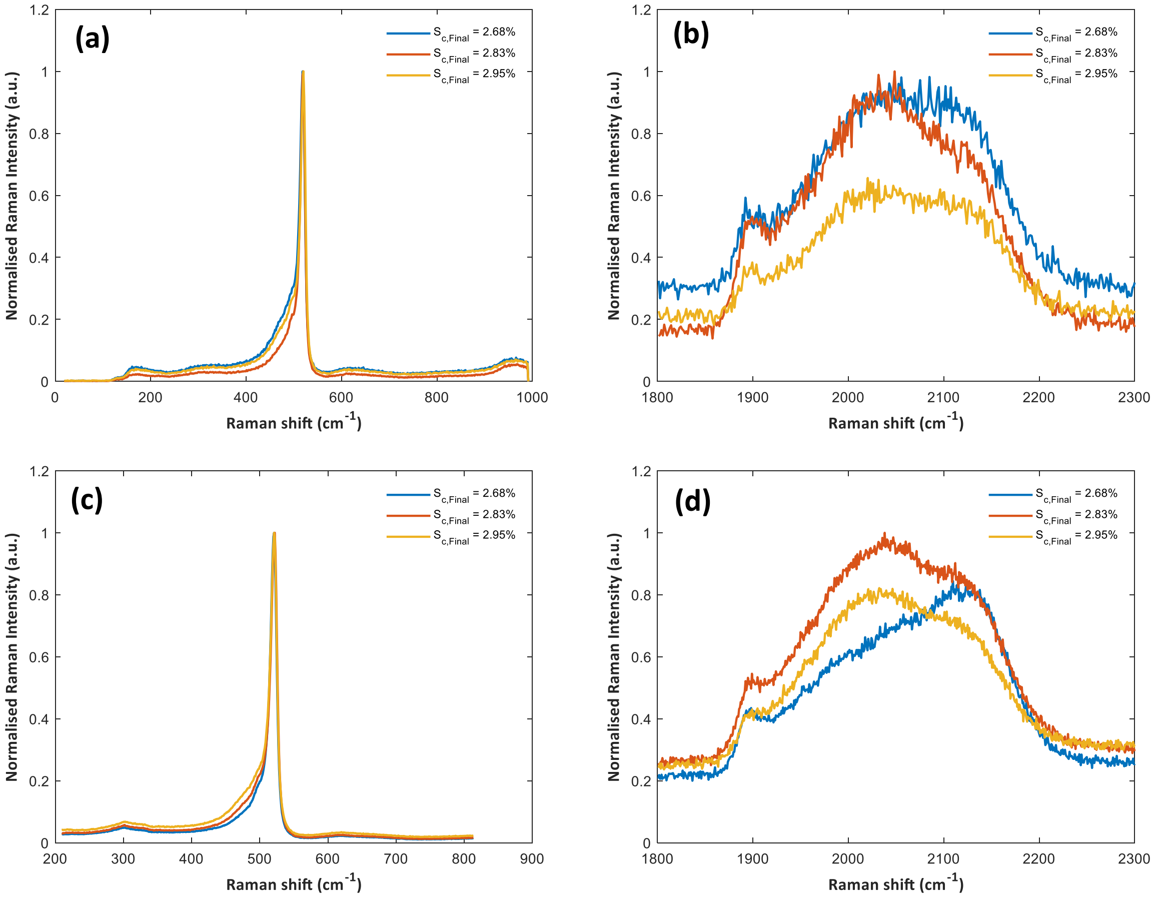

***Figure 60**: Raman spectra of p-i-n cells deposited at different silane concentrations with graded seed layers tuned to final silane concentration (a) Green laser normal range, (b) Green laser extended range, (c) Red laser normal range, (d) Red laser extended range.*

From this experiment, it can be concluded that graded seed layers can be used for growing nc-Si:H intrinsic layers within a certain silane concentration window while maintaining device grade properties. Concurrently, nc-Si:H with good microstructure homogeneity in the growth direction is present. As demonstrated by the device grade signatures exhibited by the graded seed layers from section 5.1.11, a good p-i interface is already implemented into these p-i-n cells. The seed layer, which acts as a buffer between the p and i layer can improve the V_{oc} of the solar cell due to reduced recombination at the interface, while allowing the p-layer to be undisturbed [52]. Moreover, an increase in J_{sc} is also expected due to increase in crystalline fraction in the bulk of the nc-Si:H. This is shown in Figure 61 where the crystalline fraction in the p-i-n cells with graded seed layers is higher when measured with the red laser than with the green laser. This indicates that there is high crystallization in the bulk of the nc-Si:H i-layer.

The p-i-n cells with ungraded seed layers seem to exhibit thickness homogeneity with respect to crystalline fraction as observed by closeness of the red and green laser results in Figure 61. This is because no silane concentration grading is used in the same. It is also interesting to note that the crystalline fraction does not decrease with increasing silane flow as observed with glass. On glass substrates, a clear transition from crystalline to amorphous is observed, which is not apparent on the Al foil [18].

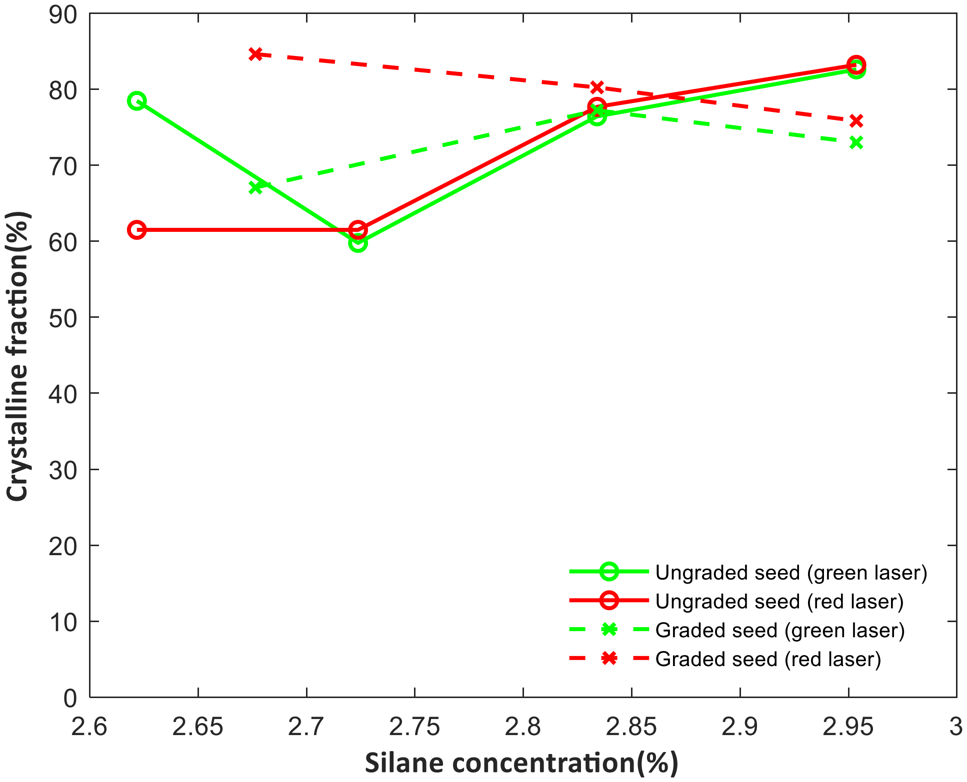

Figure 61: A comparison of the evolution of crystalline fraction in graded and ungraded seed layers.

Using graded seed layers, S_c between 2.68% and 3% gave very good signatures with good thickness homogeneity. This is better than the results for ungraded seed layers from section 5.1.8 where the optimal S_c was between 2.72% and 2.95%, however only $S_c = 2.95\%$ exhibited thickness homogeneity. It seems that with a properly tuned seed layer, the desired properties of nc-Si:H can be achieved without giving too much weight to the silane concentration as a limiting factor. This, however, should only be applicable when using aluminium substrates, and should be tested on glass substrates before coming to the same conclusion.

Therefore, the final p-i-n cells developed with graded seeding can be expected to perform well, however, it should be noted that the improvements will be an interplay between the gain in J_{sc}, V_{oc} and FF. The high crystallinities obtained using seeding is even more important for tandem solar cells where the bottom nc-Si:H cell is expected to have a strong long (red) wavelength response.

5.1.14 Effect of graded seed layers on preferential growth orientation of nc-Si:H

XRD measurements are done to investigate the preferred growth plane of nano-crystallites (crystalline grains). As explained in section 4.6, it has been found that growth in (220) plane is more favourable than the (111) plane, this enhances the efficiency of nc-Si:H solar cells. XRD measurements were taken on 3 different samples: (i) S_c = 2.83% with ungraded seed layer, (ii) graded seed layer with $S_{c,\,Final}$ = 2.83% and $S_{c,\,Initial} = 0.2*S_{c,\,Final}$ and (iii) graded seed layer with $S_{c,\,Final}$ = 2.95% and $S_{c,\,Initial} = 0.2*S_{c,\,Final}$. In each case, MST 4 is used to prepare substrate textures. A 700 nm layer of AZO is deposited, followed by a 25 nm p-layer before the seed layer and main i-layer is deposited with similar conditions to section 5.1.13.

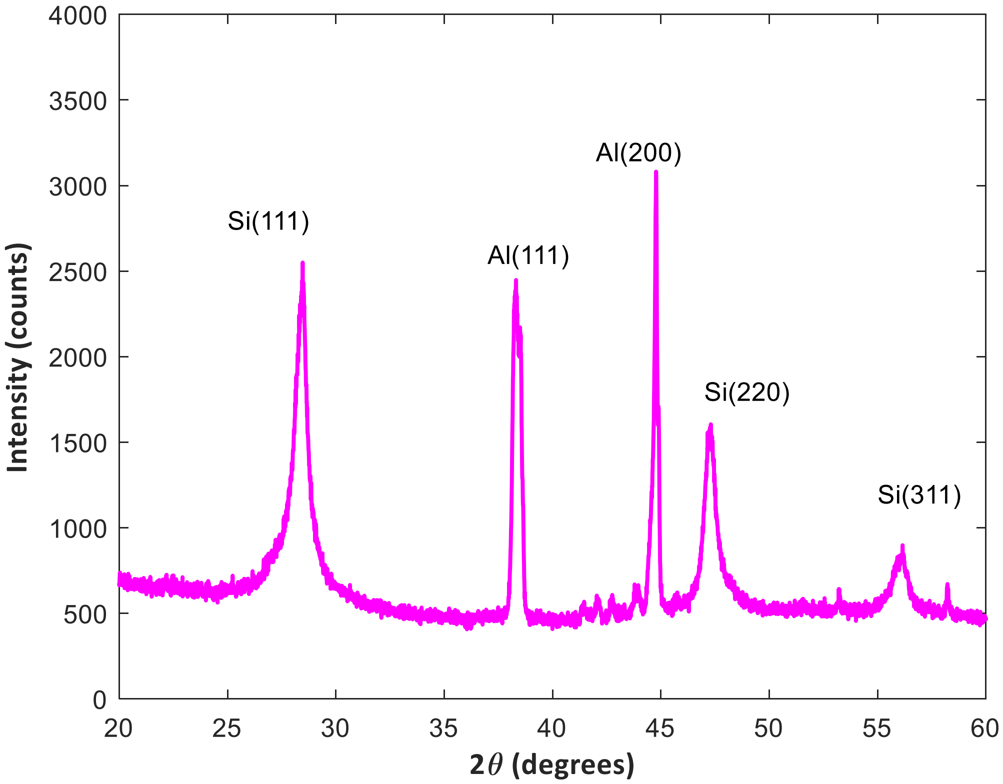

Figure 62: *XRD spectra of ungraded seed with S_c = 2.83% (H_2 = 120 sccm & SiH_4 = 3.5 sccm).*

Figure 62 corresponds to the XRD spectra of the ungraded seed layer deposited at S_c = 1% for 500 seconds, followed by an i-layer deposited for 5000 seconds with S_c = 2.83%. The spectrum shows three planes of preferred crystal growth orientation for Si in the (111), (220) and (311) plane. The (111) and (220) crystallographic orientations of aluminium is also observed, these can be attributed to the Al substrate or the ZnO:Al (TCO) layer. The Si (111) orientation has the highest intensity followed by Si (220) and Si (311). The ratio of the intensities of Si (220) to Si (111) is $I_{(220)}/I_{(111)} = 0.62$. The significance of Si (111) is most likely the result of random nucleation that also give rise to poly-hydride bonds at the grain boundaries [30]. Therefore, this type of cell is expected to result in relatively under-performing solar cells. The following can be concluded regarding the ungraded seed layer:

1. It provides a bad p-i interface that leads to random nucleation [30].
2. It results in defect rich (poly-hydride grain boundaries) nc-Si:H grown in the (111) plane [30].

When examining the XRD spectra of a i-layer deposited for 5000 seconds on a graded seed tuned to the same final silane concentration as in the ungraded case, it can be seen that the intensity of the Si (220) is slightly higher than Si (111) and $I_{(220)/(111)}$ = 1.12 as shown in Figure 63. For S_c = 2.95% with graded seed layer, the results of the XRD from Figure 64 shows encouraging results where the intensity of the Si (220) is much higher than the Si (111) plane when compared to both the previous experiments. The ratio $I_{(220)}$/ $I_{(111)}$ = 1.35. The results confirm that graded seeding seems to encourage the (220) preferential growth orientation of the nano-crystallites. As a consequence, high quality nc-Si:H solar cells with reduced bulk recombination and higher values of V_{oc} and FF can be expected [30].

It should be noted that these experiments were undertaken on MST 4. Using different underlying layers with respect to MST, p-layer or TCO may introduce induce different growth effects. However, the above findings indicate that graded seed layers have a positive effect on the nc-Si:H material properties and there exists a possibility to tune the seed layers to decouple strong substrate influences on crystallite formation.

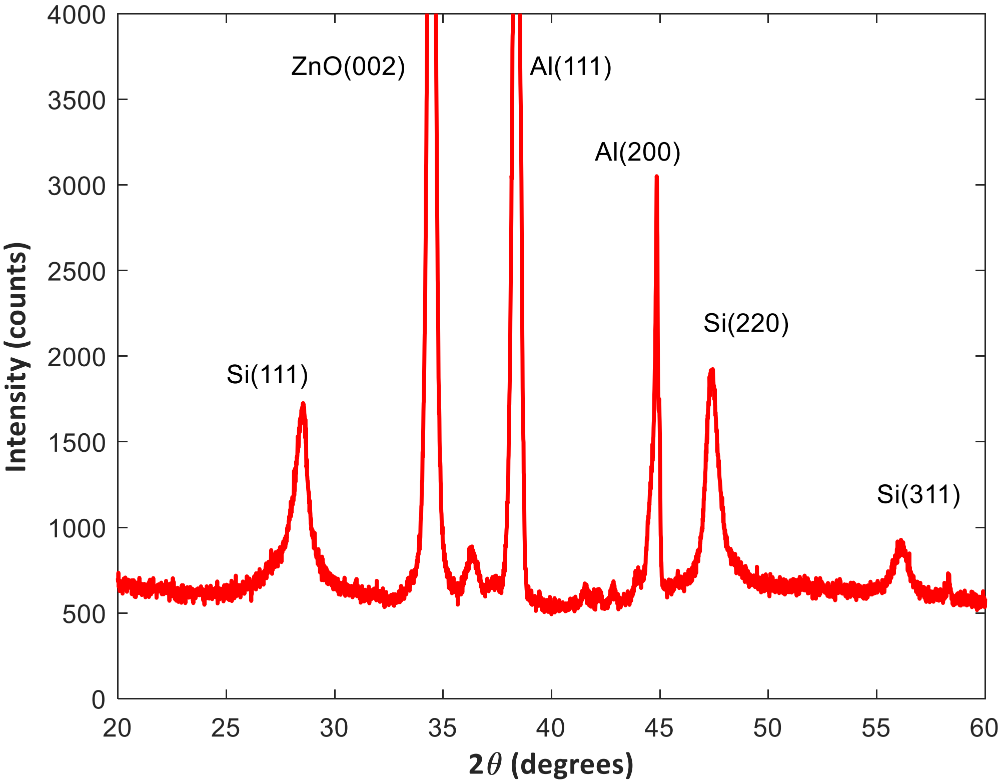

***Figure 63**: XRD spectra of graded seed with $S_{c,\ Final}$ = 2.83% (H_2 = 120 sccm & SiH_4 = 3.5 sccm).*

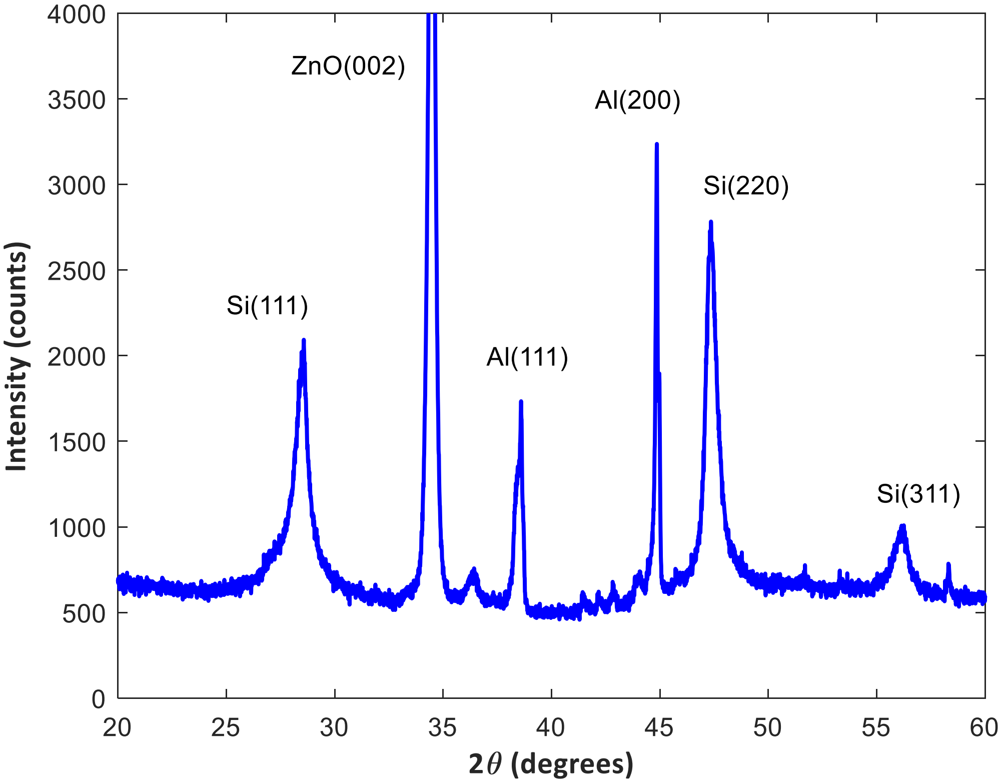

***Figure 64**: XRD spectra of graded seed with $S_{c, Final}$ = 2.95% (H_2 = 115 sccm & SiH_4 = 3.5 sccm).*

5.1.15 Optical Simulations and influence of MST

The optical simulations are run on three different surface textures; (i) HyET factory baseline pre-treatment (Figure 29) combined with FTO (ii) HyET new factory pre-treatment (Figure 35) combined with FTO and (iii) MST 4, which exhibits best micro-textures (Figure 34) combined with FTO. Note here, that FTO is used instead of AZO as front TCO because HyET employs the same in its solar cell stack. This is to provide a realistic comparison between the performance. The surface morphology is modelled based on real data from AFM measurements. A baseline i-layer thickness of 2.3 µm is chosen, details of all layers are given in Table 12.

***Table 12**: Model parameters for GenPro4 simulations*

Medium	GenPro4 Input type	Thickness
Air	Layer	N/A
Interface 1	Flat	N/A
Top encapsulation	Interface coating	140 µm
Glue	Layer	500 µm
Interface 2	Interface texture	N/A
FTO	Interface coating	700nm
AZO	Interface coating	20 nm
p-nc-SiO_x:H	Interface coating	25 nm
i-nc-Si:H	Layer	2.3 µm
Interface 3	Interface texture	N/A
n-nc-SiO_x:H	Interface coating	25 nm
AZO	Interface coating	80 nm

Aluminium	Interface coating	300 nm
Air	Layer	N/A

Figure 65 illustrates the layers described in the above table. In conventional p-i-n cells light trapping is achieved through roughness of the front TCO. However in this case, the microtextures imprinted by the substrate will also come into play, these features are modelled by interface 2. In the bottom layers, light trapping is achieved mainly by the back reflector. However, in this case, the bottom layers are expected to retain the micro textures of the substrate (shown in Figure 84), these features are modelled by interface 3.

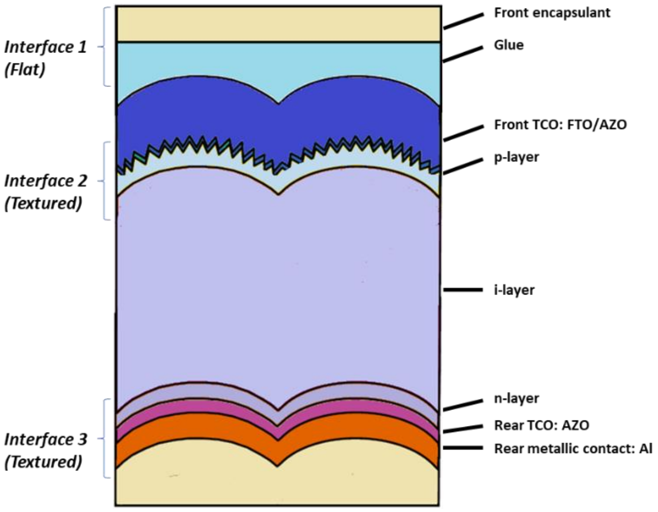

Figure 65*: Solar cell stack as modelled in GenPro4.*

GenPro4 has three models for simulating interfaces, namely flat, wave and ray model. The flat model is for flat interfaces, the wave model is used to simulate scattering effect from features smaller than the wavelength and ray model is used for features larger than the wavelength. Although there is no specific model for modulated surface textures, ray model is mostly applicable to MST due to dominance of feature sizes in the order of micrometres, and wave mode is applicable to nano-textured interfaces.

The results are sumarised in Table 13. The implied photocurrent of nc-Si:H solar cell increases from 22.41 mA/cm^2 to 25.95 mA/cm^2 when changing the surface features from the factory baseline to the modulated surface features. Between the new factory pretreatment and MST 4, there is only 0.23 mA/cm^2 increase in current. However, due to larger craters in MST 4, higher quality nc-Si:H can be grown [22]. Therefore, the cells employed with better MST features are expected to have better V_{oc} and FF resulting in higher efficiency solar cells when compared to the new factory pretreatment [54].

Table 13*: The results of the GenPro4 simulations with 3 different surface morphologies.*

Etching Recipe	**Interface model**	**Features**	**Implied photocurrent (mA/cm^2)**
Factory baseline pretreatment	Wave	Flat nano-textured surface	22.41
New factory pretreatment	Ray	Moderate modulated surface textures	25.95
MST 4	Ray	Best modulated surface textures	26.18

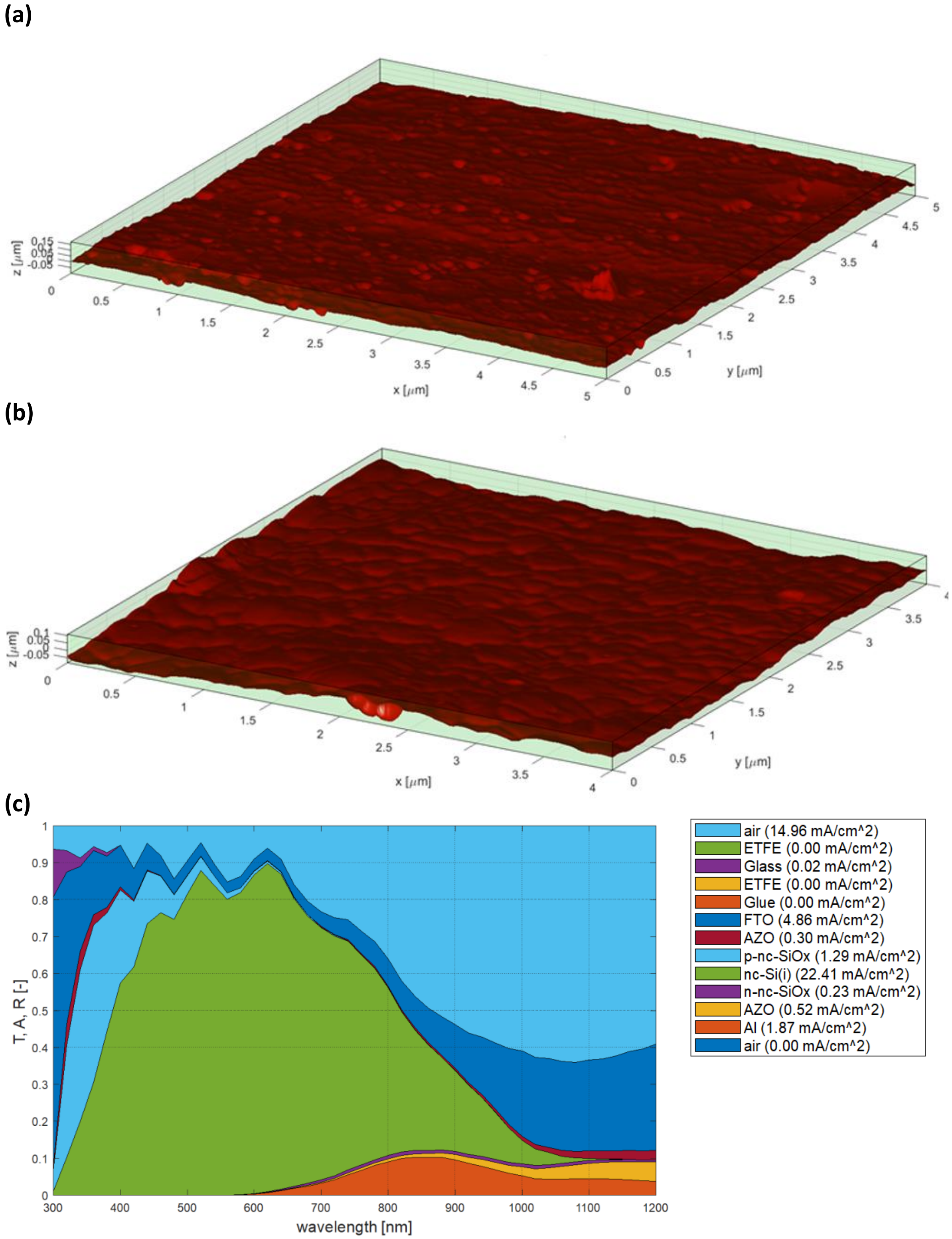

***Figure 66**: GenPro4 simulation results for HyET factory baseline superimposed with FTO, (a) Surface morphology of solar cell interface 2, (b) Surface morphology of solar cell interface 3, (c) Optical gain(losses) quantified in terms of implied photocurrent.*

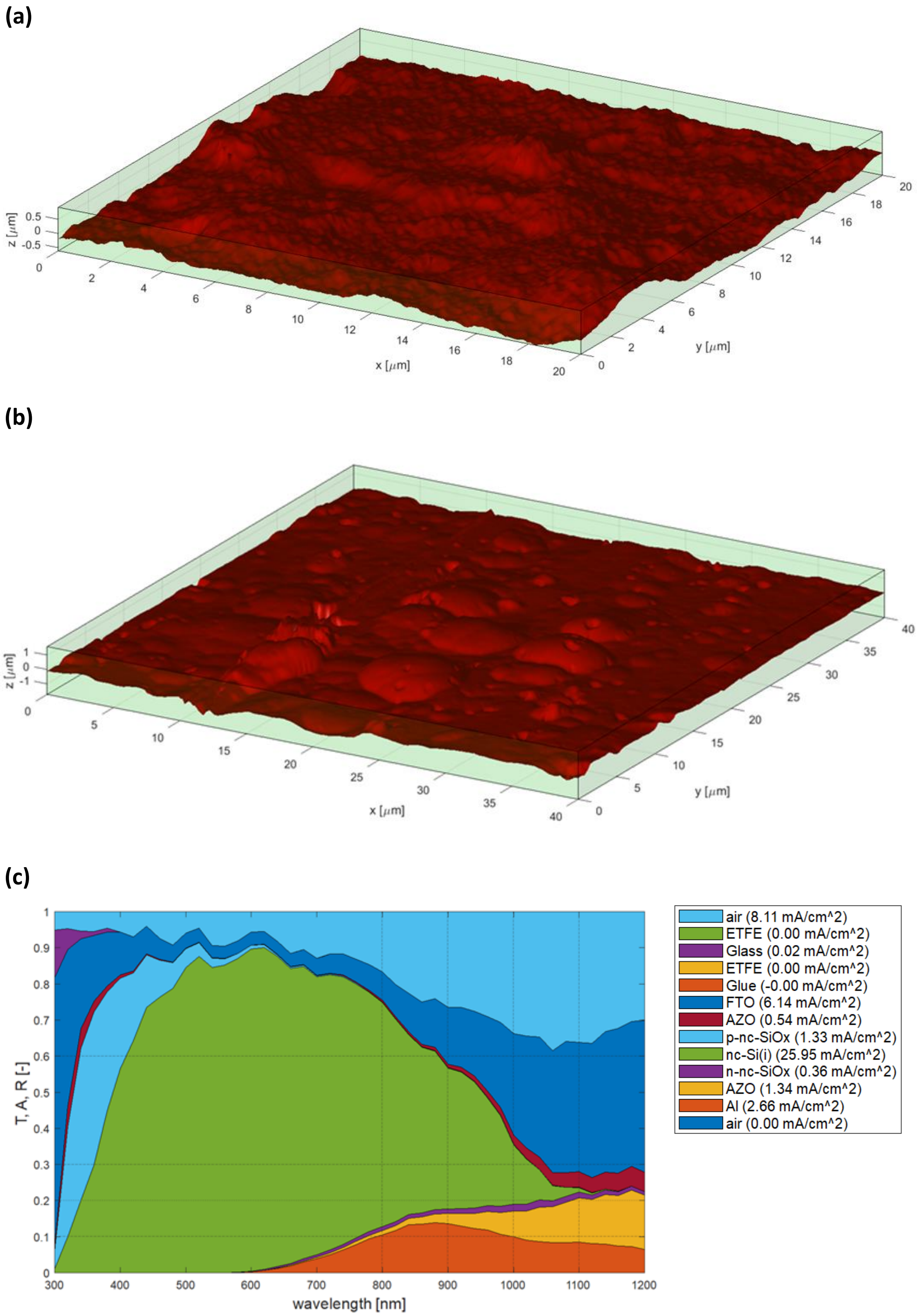

Figure 67*: GenPro4 simulation results for HyET new pre-treatment superimposed with FTO, (a) Surface morphology of solar cell interface 2, (b) Surface morphology of solar cell interface 3, (c) Optical gain(losses) quantified in terms of implied photocurrent.*

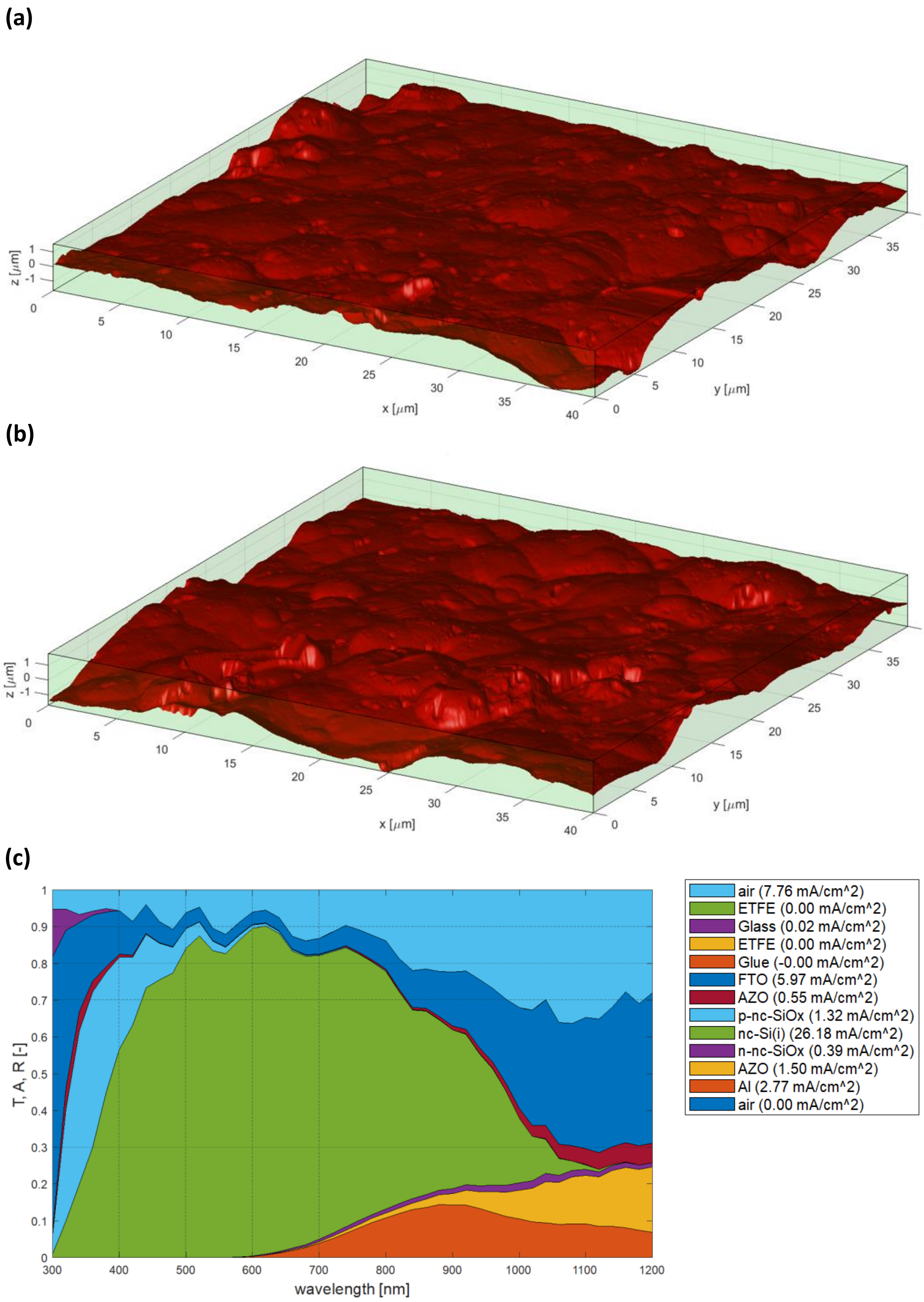

***Figure 68**: GenPro4 simulation results for best micro-textures superimposed with FTO, (a) Surface morphology of solar cell interface 2, (b))Surface morphology of solar cell interface 3, (c) Optical gain(losses) quantified in terms of implied photocurrent.*

The absorptance curves of the i-layer in nc-Si:H cells with modulated surface features and factory baseline features is shown in Figure 69. The extra current is due to better absorption from 700 nm to 1200 nm. This improvement suggests better scattering in the infrared range which can attributed to larger feature sizes in the MST that are able to scatter diffuse light more efficiently at larger angles through Mie scattering [26]. This increases the optical path length allowing more light to be absorbed in the nc-Si:H i-layer. The new factory baseline pre-treatment can only rely on nano-sized features of the FTO to scatter light below 600 nm through Rayleigh scattering.

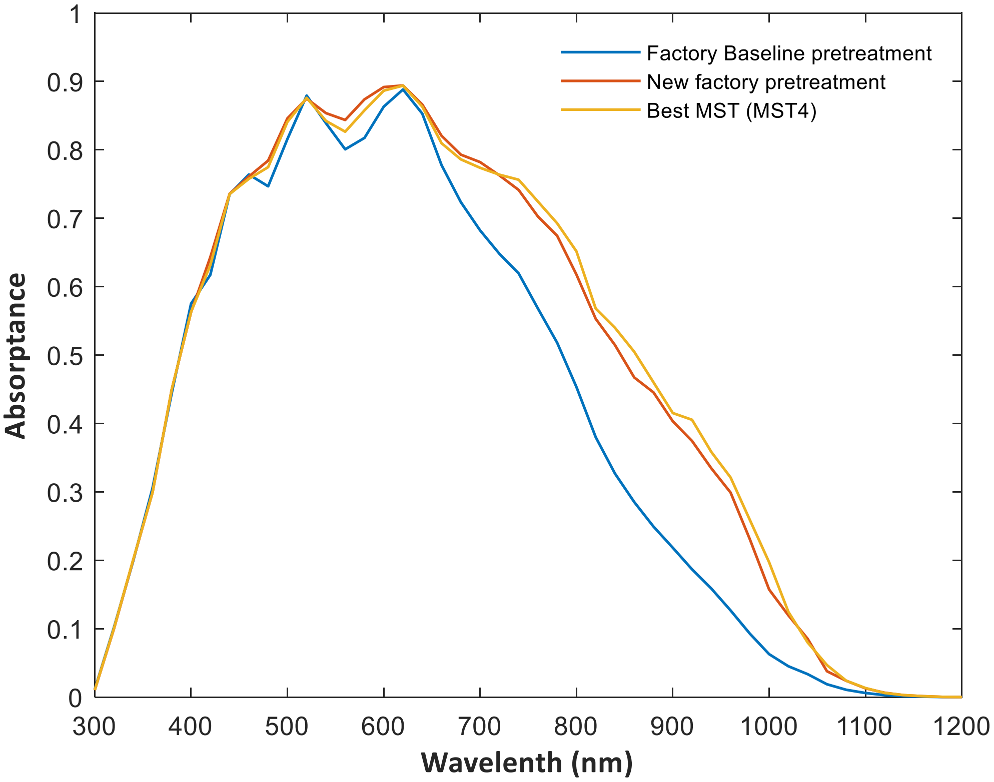

***Figure 69**: Comparison between the EQE of factory baseline pre-treatment and MST4 textures.*

To better understand how GenPro4 simulates textured surfaces, a simulation is undertaken using five different cases; (i) Flat surface with no textures using flat model, (ii) Micro-textures only of new pre-treatment using ray model, (iii) MST of new pre-treatment using wave model, (iv) MST of new pre-treatment using ray model and (v) Factory baseline using wave model. An intrinsic layer of 2.3 µm was used in all five cases similar to above experiments, and all other layers are similar to Table 12.

The results are shown in Figure 70. The “new pre-treatment MST” and “new pre-treatment micro textures only” using ray model show very similar results. This shows that GenPro4 takes into account only larger surface features when using the ray model. The “new pre-treatment MST” using wave model shows that it has improved scattering over the “factory baseline” between 700 nm and 1200 nm. This shows that there is scattering effect due to nano-textured features on the “new pre-treatment MST” even in long wavelength range. Whether these scattering effects are included in the results of the ray model and to what extent is unknown without deeper knowledge into how GenPro4 works. It should be noted that the ray model cannot be perfectly applied to MST as it is a combination of nano- and micro-sized features. However, from Figure 70, it is evident, that the difference in results would be between 700 nm and 1200 nm since the results for different combinations of models and textures are fairly similar between 300 nm and 700 nm.

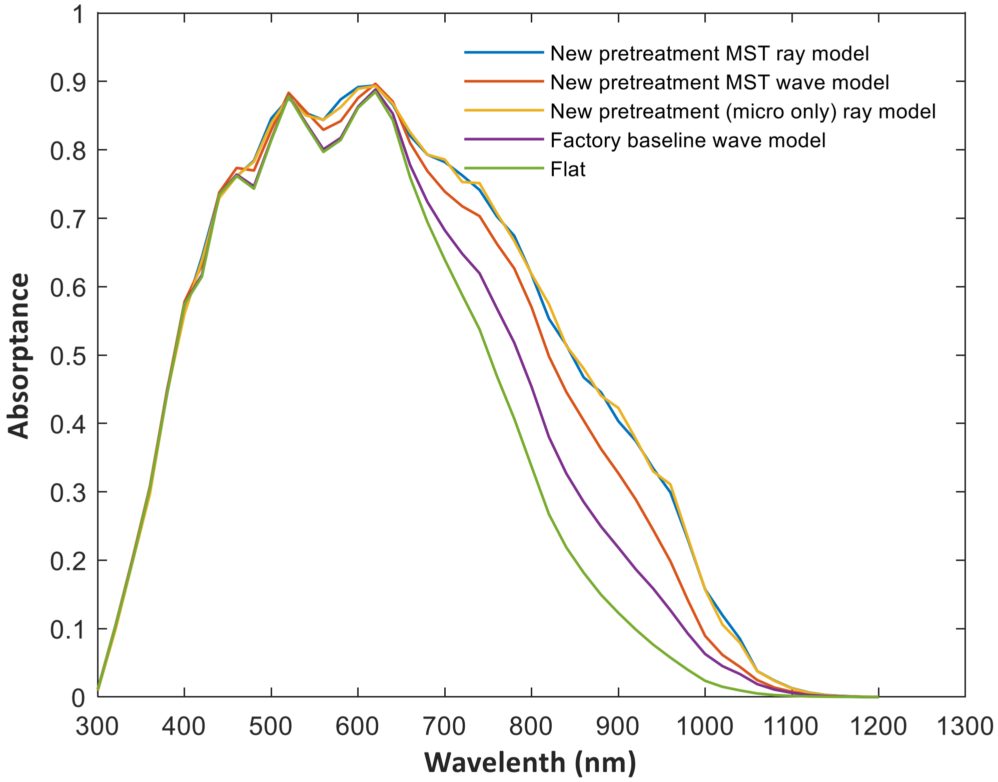

***Figure 70**: Contribution of micro and nano-textures to the implied EQE curve of the solar cell.*

A thickness series is done with the new factory pre-treatment and MST 4 to compare the photocurrent gains by employing better interface features. The i-layer thickness is varied between 1 µm and 5 µm. The back contact is also varied between aluminium and silver to understand its effect. The results plotted in Figure 71, show that there is a non-linear increase of photocurrent with thickness of i-layer. On average, 0.3 mA/cm^2 can be gained using better interface textures and 1 mA/cm^2 can be gained by changing from Al to Ag back contact. This is due to much better reflectivity of Ag compared to Al.

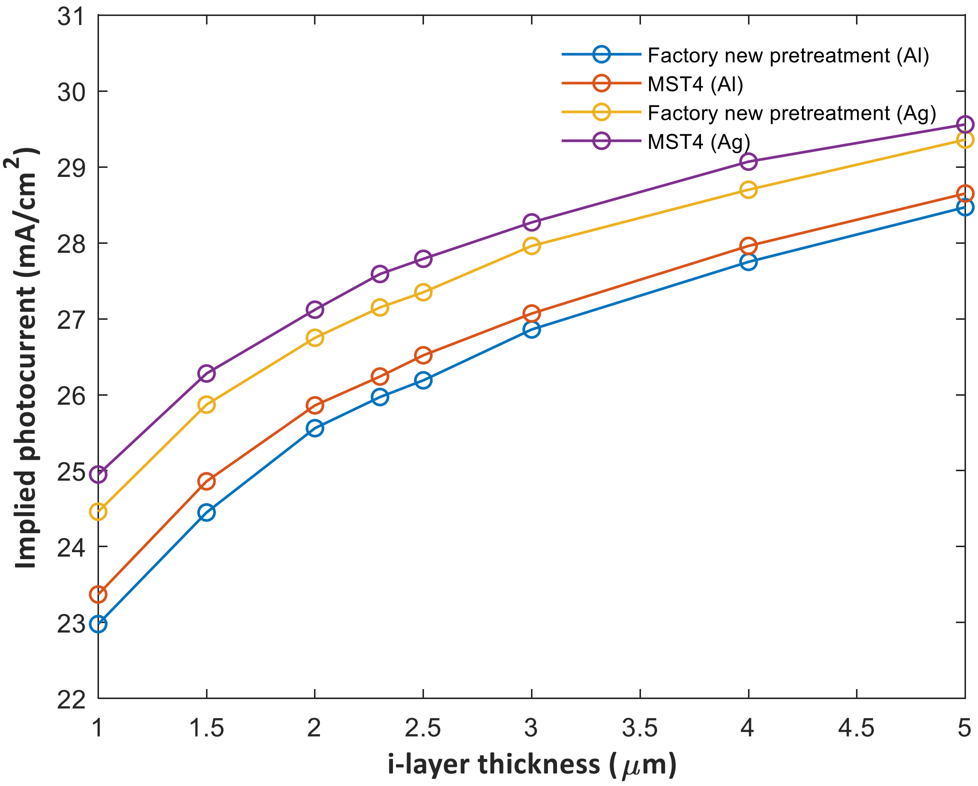

***Figure 71**: i-layer thickness series undertaken using surface features pertaining to HyET factory baseline and MST 4 surface. The back contact is also varied between Al and Ag to understand its effect on photocurrent.*

To check the validity of the simulation results, a simple comparison is made. For a 3 µm thick cell with Ag back contact, employing MST 4 textures and without front encapsulation, the simulation gives an implied photocurrent of 26.36 mA/cm^2. With real solar cells made on glass substrates using MST with similar feature sizes (L_c and σ_{rms}) and Ag back contact, a J_{sc} of 25.6 mA/cm^2 is obtained [22]. These values are comparable accounting for recombination losses in the real cells and slight difference in TCO used. Therefore, using the ray model, the simulation results agree with the expectations. However, a better validation of the results needs to be done after completing nc-Si:H cells at HyET.

Finally, it should be noted that further improvements to the implied photocurrent can be achieved by:

1. Optimizing MST 4 using thicker Al foils to achieve better feature distribution. The surface features of MST 4 are only the best so far and, furthermore, the AFM data used in above experiments may not be best representative of the quality of surface features.
2. Making the p-nc-SiOx:H more transparent to light in the shorter wavelength. This is achieved by varying the deposition conditions to alter the oxygen content in the layer and consequently its opto-electrical properties [55].
3. Optimizing the layer thicknesses for front encapsulation layers and TCO to increase transmittance of light into i-layer. The top encapsulant, TCO and back contact layers used in the above simulations have similar specifications to HyET's a-Si:H modules. Therefore, the layers can be optimized to make better use of light in the 800 nm to 1100 nm range where nc-Si:H cells outperform a-Si:H cells [6].

5.2 Work undertaken at HyET Solar

This section of the report focuses on work undertaken at HyET to complete the p-i-n cells deposited at TU Delft. The main steps to be performed here are (i) laser scribing to define cell area and isolate cells, (ii) the lamination of the permanent carrier foil and (iii) etching of the temporary Al foil substrate. As explained earlier, the primary aim at TU Delft was to optimize the MST features and characterize the growth of high quality nc-Si:H cells that would yield high performance in both single and tandem cells. Following these milestones, the next step is to complete cells on 10x10 cm^2 foils at HyET such their performance can be tested. The laser scribing and the lamination can be done only at HyET, whereas the etching process can be completed at TU Delft. However, to avoid unnecessary delays and interruptions, all the subsequent steps are performed at HyET with our assistance.

5.2.1 Dark J-V results of high quality nc-Si:H solar cells

The solar cells optimized at TU Delft comprise of Al substrate/AZO/p-i-n stack with i-layer deposited using the graded seeds. At HyET, 4x4 mm^2 area squares are sputtered with AZO/aluminium as shown in Figure 72. The dark J-V curves of some of the measurements shown in Figure 73 exhibit diode behaviour.

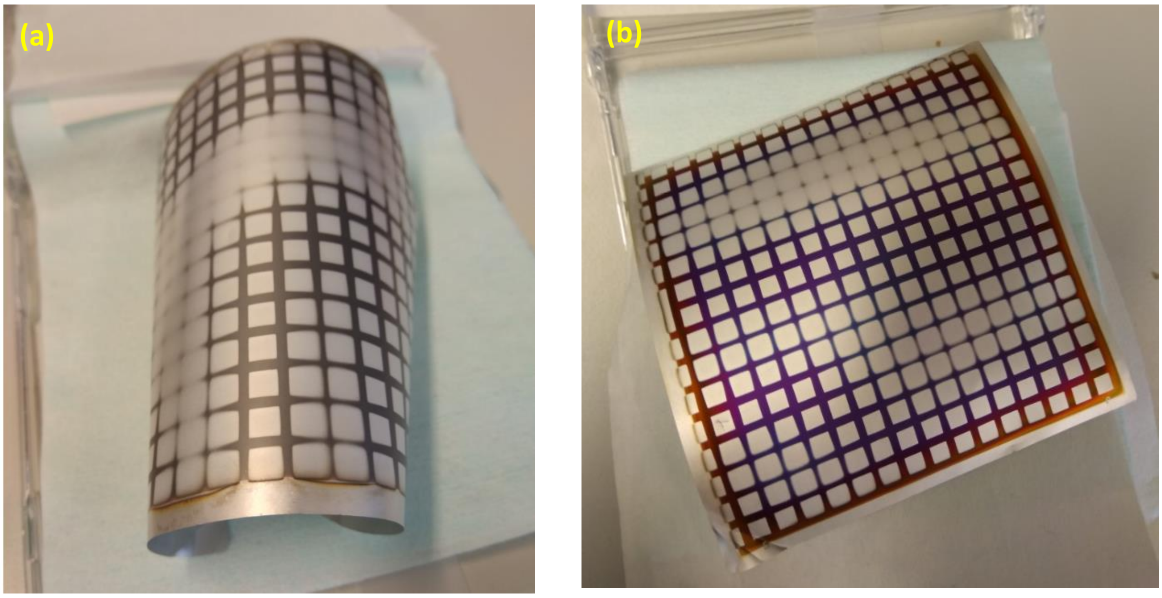

***Figure 72**: The 4x4 cm^2 square Al sputtered as a contact on top of the (a) nc-Si:H cell, (b) a-Si:H cell. The nc-Si:H solar cell is thicker and therefore, more bent due to inbuilt stresses.*

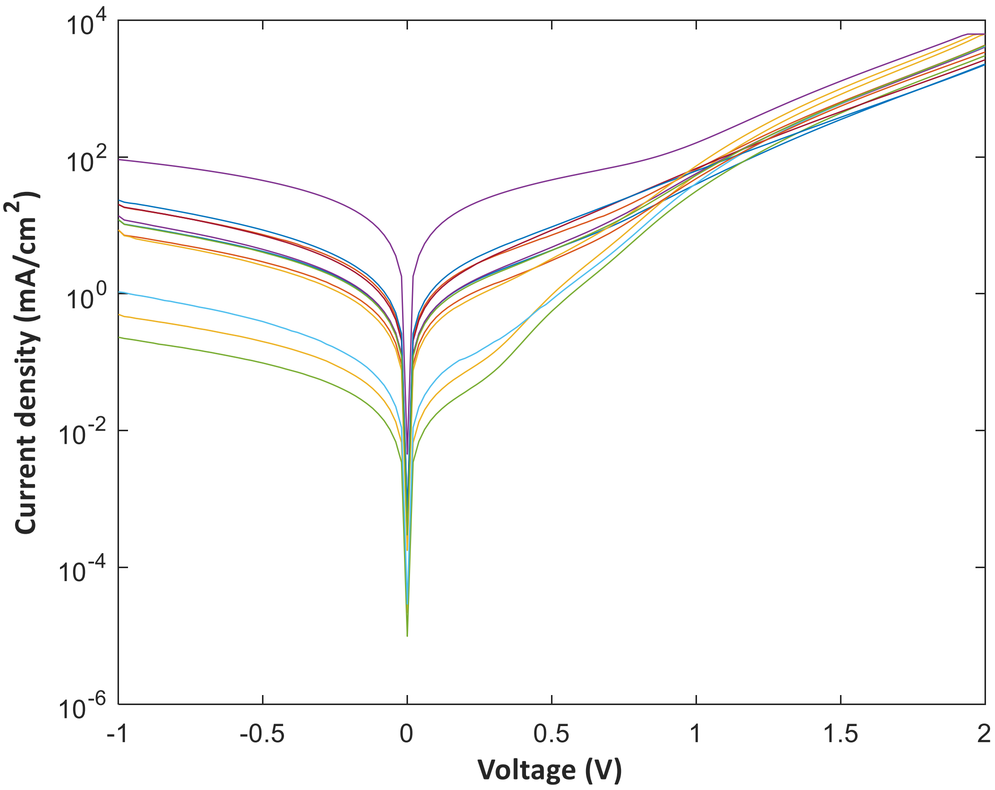

***Figure 73**: Some of the dark J-V curves tested on different contacts on the same nc-Si:H sample.*

When comparing the shunt resistance values, the nc-Si:H exhibits very strong performance. From Figure 74, the average shunt resistance is at least 10 orders of magnitude higher than that of the a-Si:H cells developed at TU Delft and at HyET. For nc-Si:H cells, the closeness of the distribution in shunt resistance values indicate that the quality of the solar cell layers is homogeneous throughout the area. This is not the case for a-Si:H cells where the spread is distributed over a larger range. This is indicative of high quality nc-Si:H with few cracks and shunts. As a consequence, solar cells with high FF and V_{oc} can be expected.

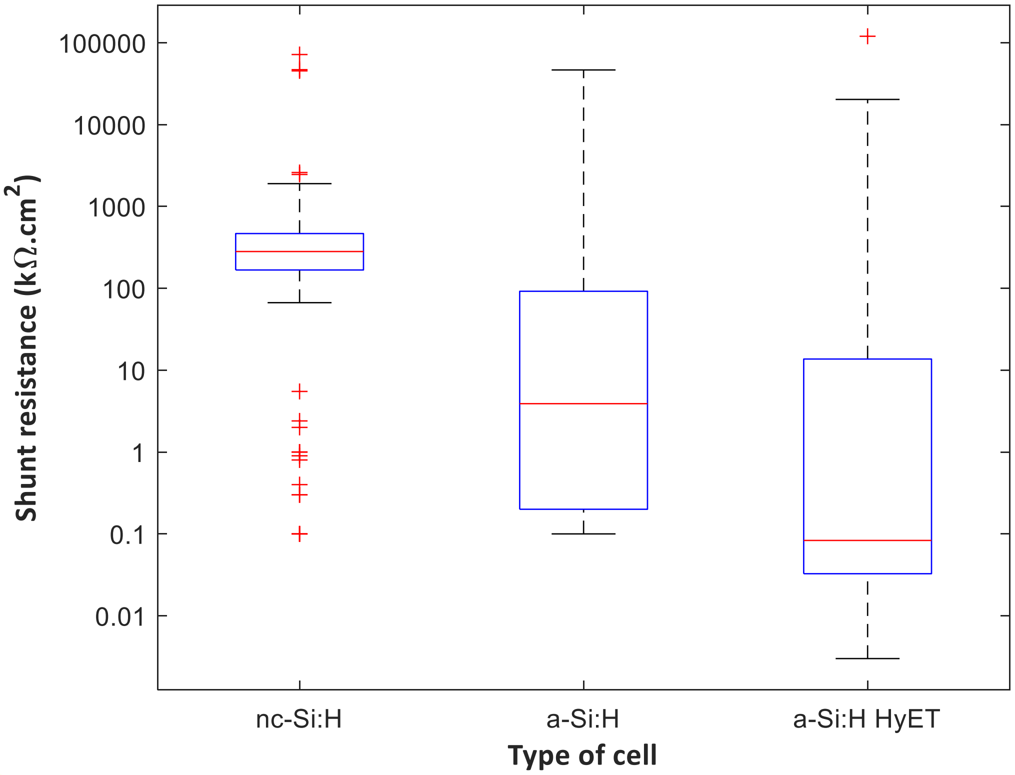

***Figure 74**: The shunt resistance of the nc-Si:H and a-Si:H developed at TU delft is compared to that of a-Si:H modules made at HyET Solar.*

5.2.2 Creation of 1X5 cm^2 single junction nc-Si:H cells

The fabrication of the 1x5cm^2 cells is slightly different to that described in Figure 5 which shows a complete module where cells are connected in series. Before fabricating modules, it is important to test the performance of individual cells under the AM1.5G spectrum. The foil is 10x10 cm^2, but much of the foil area will be inactive and removed. Only a maximum of 4 cells can be produced on the foil with a total active area of 20 cm^2, and total inactive area of 25 cm^2 which act as contacts between the cells. Therefore, roughly 55% of the total foil area is unused. The fabrication process is described in detail below.

Step 1 – Laser scribing to define active area

Laser scribing is done to define the cells' active area and inactive area. The laser scribes labelled P1, P2 and P4 are made and a TCO fill ink is introduced at P2; this ink insulates the front and back contacts such that holes and electrons are separately collected. A lift off ink is dispensed at P3. The purpose of the ink is to limit the total number of laser scribes.

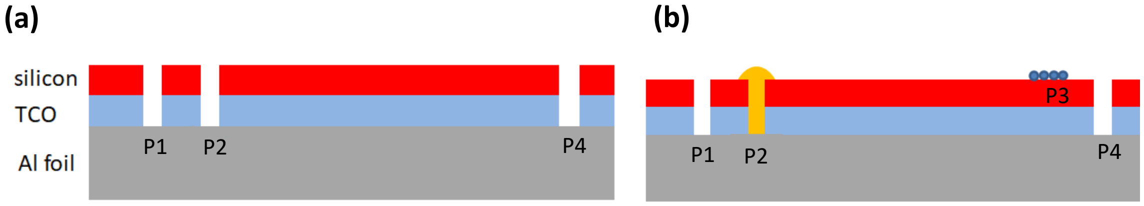

***Figure 75**: Cross-section view of solar cell (a) Laser scribes P1, P2 and P3 are made. (b) TCO fill ink is introduced at P2 and lift off ink is dispensed at P3.*

Step 2 – Deposition of back contact

The back contact is sputtered using DC magnetron sputtering, it consists of 80 nm of AZO followed by 300 nm of Al.

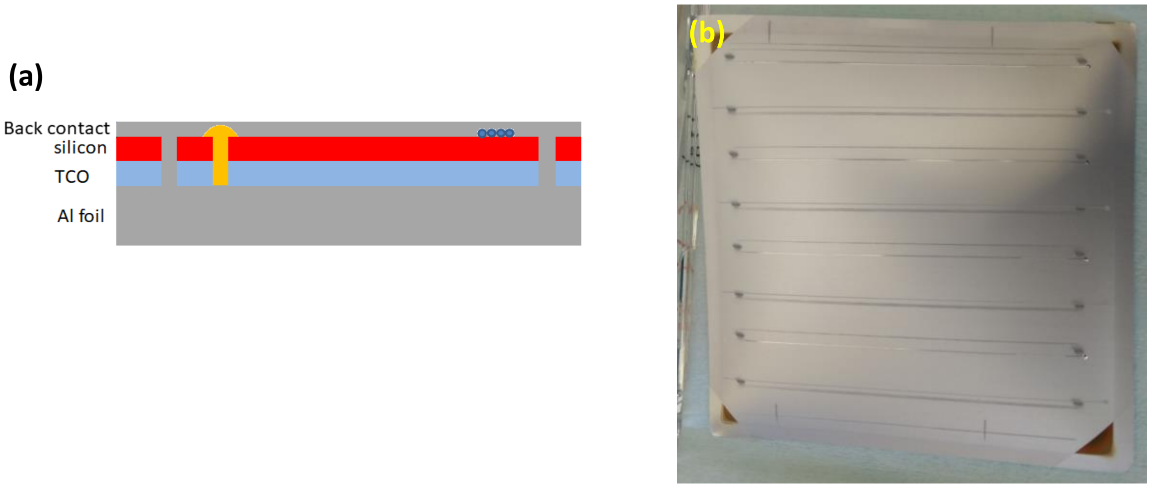

__Figure 76__: (a) Cross-section view of solar cell stack after back contact has been deposited (b) Sample as seen after the back contact is deposited, scribes are also visible.

Step 3 – Removal of lift-off ink

A Petri dish is placed under a fume hood containing a layer of Isopropanol (IPA). The sample is then placed with the back contact facing upwards as shown in Figure 77(a). The surface is sprayed with a thin layer of IPA and then covered with a cleanroom tissue soaked with the same. A maximum of four samples can be placed on top of each other. The Petri dish is then closed and left for 10 minutes. After opening the Petri dish, the first sample is taken out with care, the tissue soaked in IPA is used to gently scrub along the length of the lift-off ink. The scrubbing is done in a single direction until all traces of the lift-off ink has disappeared and the track is observed to be clear as shown in Figure 77(b). If any of the tracks do not clear off, the process should be repeated for another 10 minutes. After this step is successfully completed, the samples should be kept under the laminar air flow hood for 5 minutes.

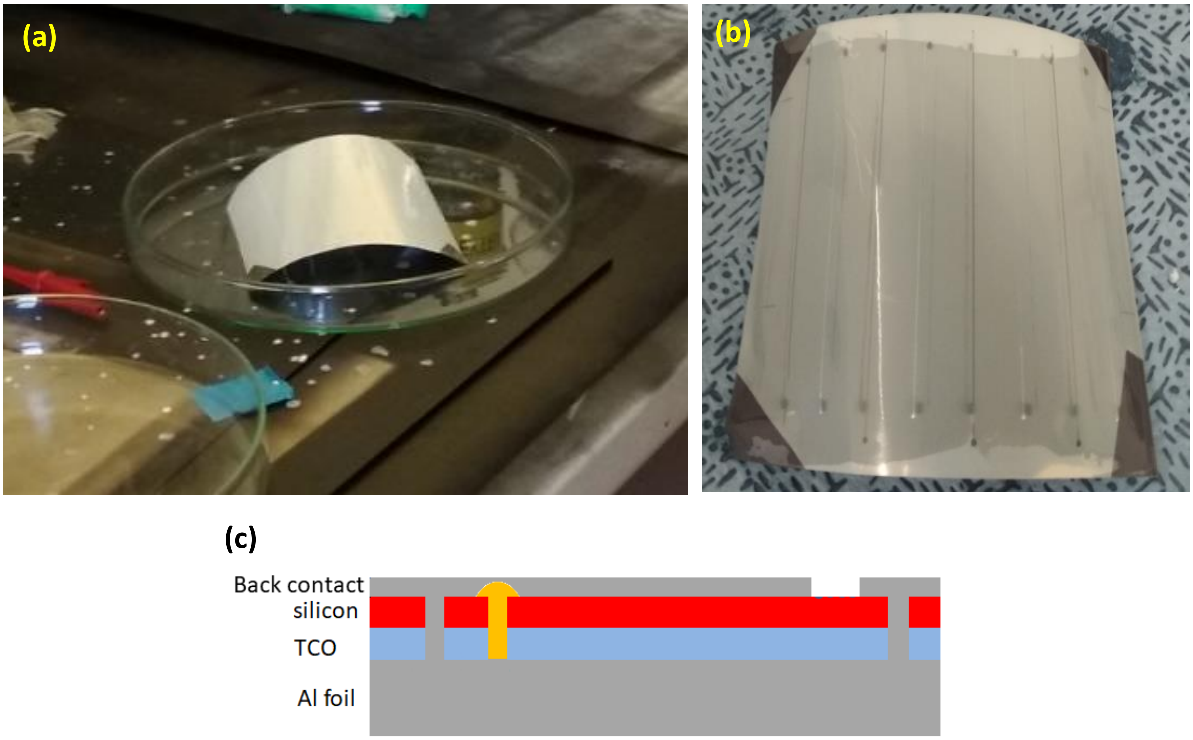

Figure 77: (a) Sample left to soak in the Petri dish (b) Sample after the lift-off ink has been removed (c) Cross-section view of solar cell stack after lift-off ink has been removed.

Step 4 – Preparation of glue

In this step the glue that holds together the lamination and the back of the solar cell is prepared. The epoxy glue consists of two components: A and B. Before component A is used, it must be put in a speed mixer at 2400 rpm for 1 minute to reduce its viscosity. As a rule of thumb used at HyET, to make glue for about 8 samples, 10 grams of component A and 0.5 grams of component B is mixed in a speed mixer at 2400 rpm for 1.5 minutes.

Step 5 – Bonding of plastic carrier foil to solar cell using glue

In this step the plastic carrier foil is glued to the solar cell before the lamination takes place in the press. Only two samples can be glued at one time due to limited space on the lamination table. Before lamination, it is important to check that the lamination table is free of dust and ensure so by cleaning the surfaces with IPA and switching on the laminar air flow. A piece of plastic foil (40x20 cm) is then cut from a roll and laid on the lamination table. A piece of scotch tape is attached to the foil to keep it from moving while the bonding is taking place. The glue is then carefully placed in a thin horizontal line at least 1 cm above where the sample will be placed as shown in Figure 78(a). Using the glass stick and pressing hard, the glue is then evenly distributed over the plastic foil in a single stroke.

The samples are placed on the plastic foil with the back contact facing the glue. The cut edge of the sample is made to align with the outline on the table to get the correct orientation of the cell. This has been done in advance at HyET to make the process easier. Some cleanroom tissues are placed around the samples to absorb excess glue during the lamination process as shown in in Figure 78(c).

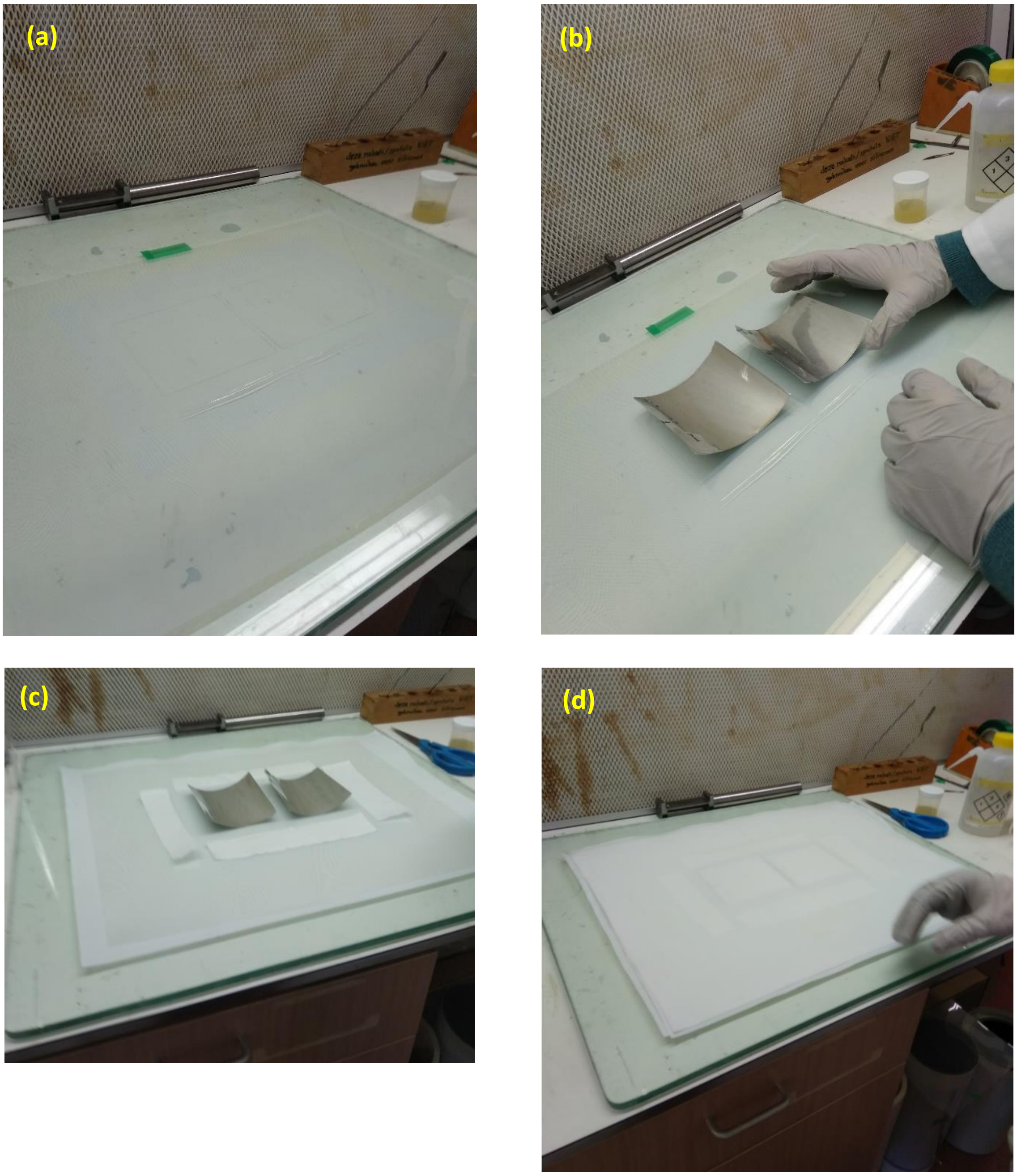

***Figure 78**: Pre-lamination preparation steps (a) Plastic foils taped to lamination table and glue has been applied. (b) Samples are placed on the glue. (c) Clean room tissue is placed around the samples to absorb excess glue during lamination. (d) Samples sandwiched between Teflon sheets.*

Step 6 – Lamination

This step involves the lamination itself. The laminator must be switched on and the vacuum must be disabled. The laminator is controlled by a desktop computer that already has preloaded settings for the process. Three Teflon sheets are taken out of the laminator, one is placed under the plastic foil and two are placed on top of the glued samples as shown in in Figure 78(d). The sandwiched sheets are then loaded into the laminator and the vacuum is enabled. Once the pressure reaches around 50 mbar, the process can be started. The process takes around 18 minutes and only two samples can be laminated at one time. Once completed, they are cut to remove excess plastic foil as shown in Figure 79(b).

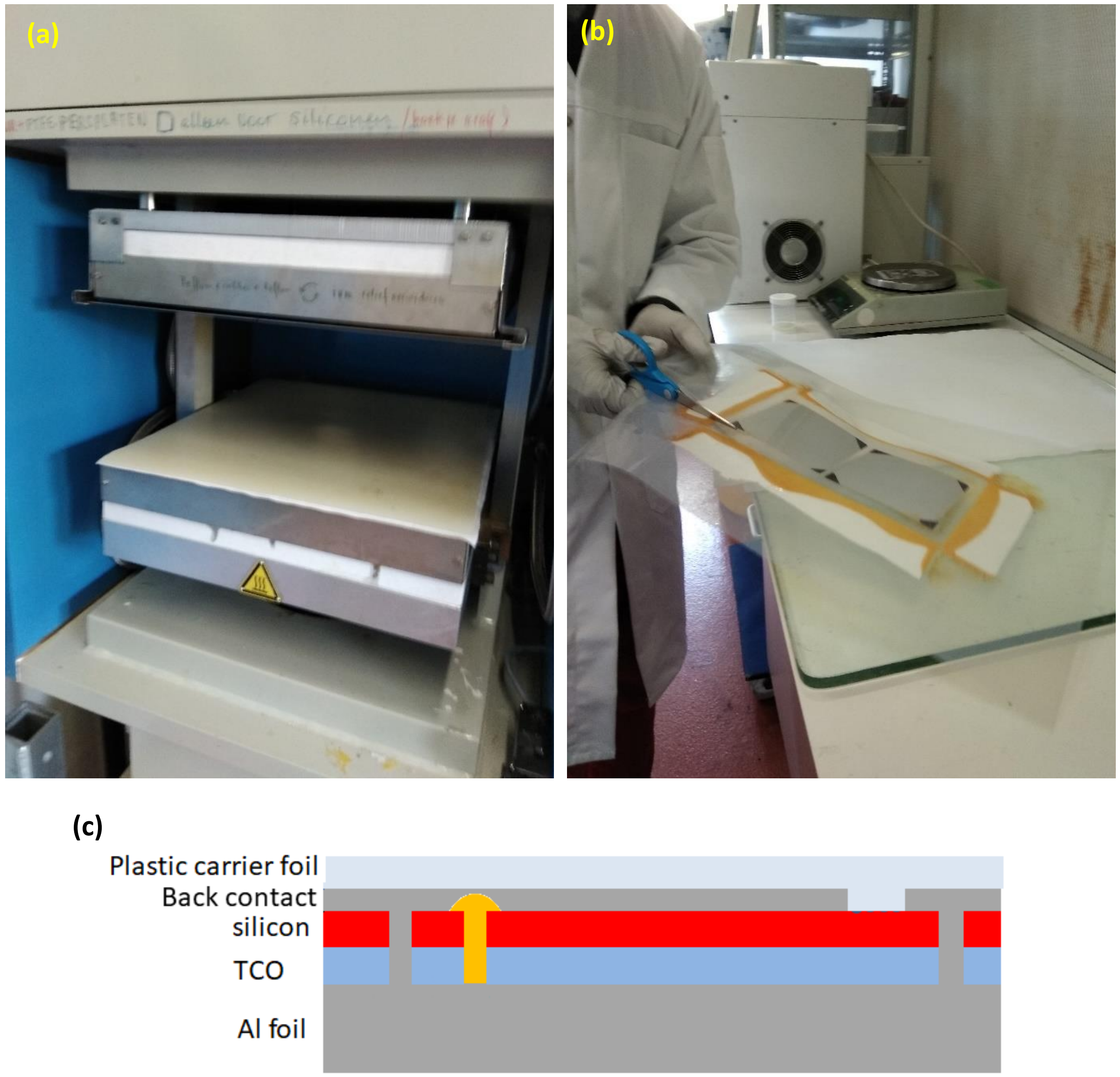

__Figure 79__: Lamination process (a) View of the lamination press loaded with samples. (b) Excess plastic foil is removed once lamination is completed. (c) Cross-section view of solar cell stack after plastic foil has been laminated.

Step 7 – Pre-etching of temporary Al substrate

This step is known as the pre-etching step. The goal is to etch away approx. 80 µm of Al foil and leave 30 µm behind for the next step which is annealing. The etching consists of three solutions:

(i) A 1.2M solution of NaOH, 5% w/w (mass of solute to mass of solution) ratio at 70° C. This is the main etching solution.
(ii) A 0.92 M solution of H_3PO_4, 9% w/w ratio at 70°C. This is an acid bath used for removing residues resulting from the etching, similar to experiments done at EKL.
(iii) Demi-water rinse bath for final cleaning of the sample.

HyET has already optimized this step for a-Si:H cells, usually the thickness of the cell resulting from Step 6 is between 230 to 288 µm. The aim of this step is to reduce this thickness by approx. 80 µm. The thickness is measured beforehand using a thickness meter. The sample is then clamped to a metal roster and inserted into the main etching solution. As a rule of thumb, the sample is etched for 5 minutes. Subsequently, the sample is dipped in the acid bath for 5 seconds to remove residues and is followed by rising with demi-water. The sample is dried, and the thickness is measured once again. If less than 80 µm is etched away, then the etching time is adjusted, and sample is re-etched until the required thickness is reached. If more than 80 µm is etched, the sample is unusable, however the etching time needs to be readjusted such that the next samples are also not ruined. At the end, all the samples should be pre-etched until 80 µm of Al foil is etched away. This ensures that approx. 30 µm of Al foil is left for the next step.

It should be noted that this process has been optimized for HyET's factory baseline foils which is about 110 microns thick after initial pre-treatment (Figure 29). However, the MST 4 developed at EKL results in a thinner Al foil of approx. 80 µm. This means the etching time should be adjusted to etch away only 50 µm leaving 30 µm. For the new factory pre-treatment (Figure 35), the same principle should apply as a thickness of Al foil resulting in 95 µm should allow etching of only 65 µm.

Step 8 - Annealing

In this step, the samples are annealed before the final etching. This is done to reduce thermal shock on the solar cell layers once the Al substrate is completely removed, otherwise it would introduce cracks in the solar cell layers. The samples are sandwiched between two aluminium plates and loaded into an oven for 20 minutes at a temperature of 175 ^{o}C. After annealing, the samples are left to cool down for at least 40 minutes before they are taken for the final step.

Step 9 – Final etching of Al substrate and completion of solar cells

In this final step, the Al under which the active solar cell area resides is etched away completely. In order to ensure that the contacts are available for J-V measurements, alternating sections of the Al foil are not etched. This is protected during the final etching by a green coloured "busbar tape", which is applied over the foil as shown in Figure 80(a). The busbar tape is resistant to etching solution and prevents parts of the Al from being removed, thus allowing these areas to act as the contacts. After applying this tape, the sample is then cut to a 5x10 cm^2 that contains the 4 cells and 5 contacts.

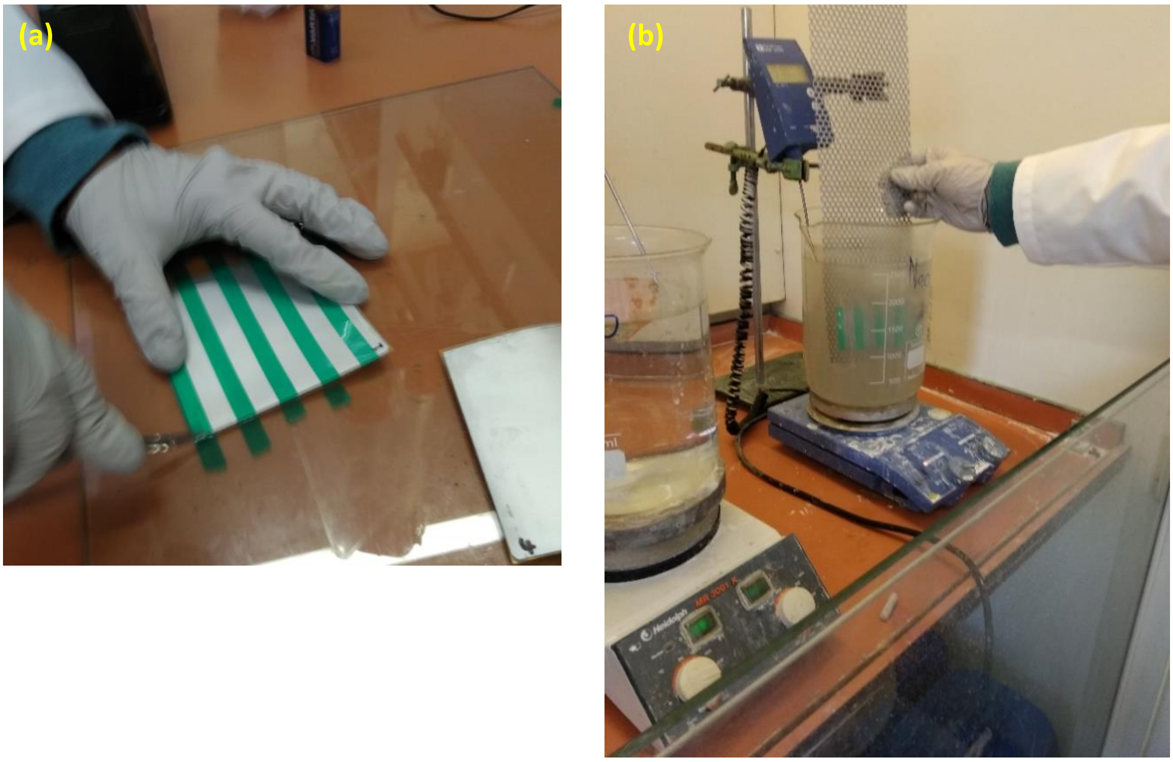

***Figure 80**: (a) Busbar tape is applied to prevent etching of the contacts, (b) final etching of the sample.*

The sample is then re-etched in the etching solution until the remaining 30 µm of Al is etched away completely. This happens when there is no more reaction observed and only the front TCO remains. For a-Si:H cells produced at HyET, a black colour is observed when the etching is complete. The sample is immediately dipped in the acid bath and rinsed with demi-water to rid of any residues. After confirming that all the Al is etched away, the sample is checked under light as shown in Figure 81, the scribes must be visible and there should be no pinholes in the active area. Finally, the busbar tapes are carefully removed to expose the contacts. The samples are then finally ready for J-V measurements. Figure 82 shows how two cells are connected between three contacts in the final arrangement.

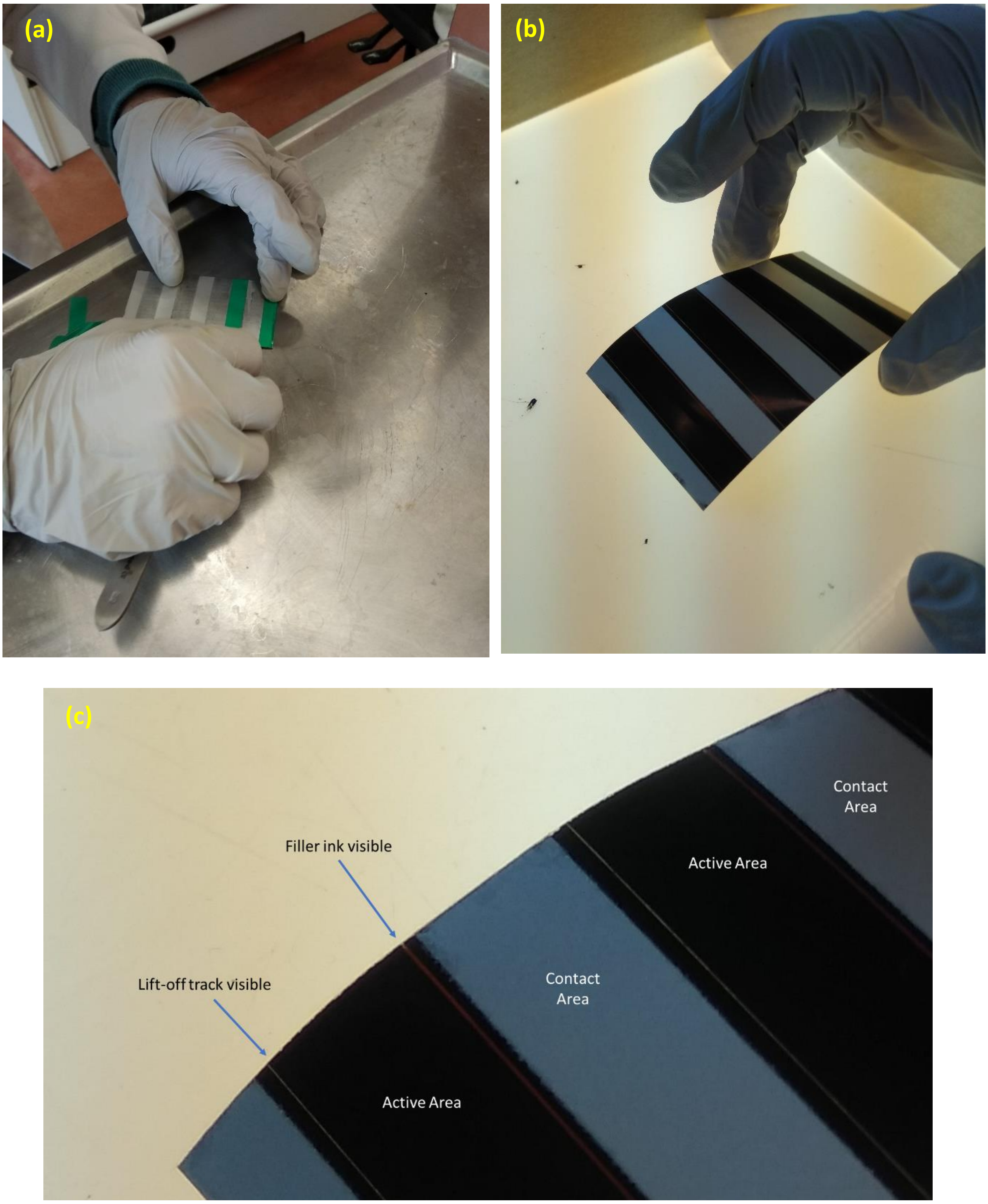

Figure 81*:(a) Busbar tape is removed once the etching is complete, (b) The sample is held up against the light to check if the scribes are visible and if pinholes are present, (c) Close of up view of scribe and lift-off under the light.*

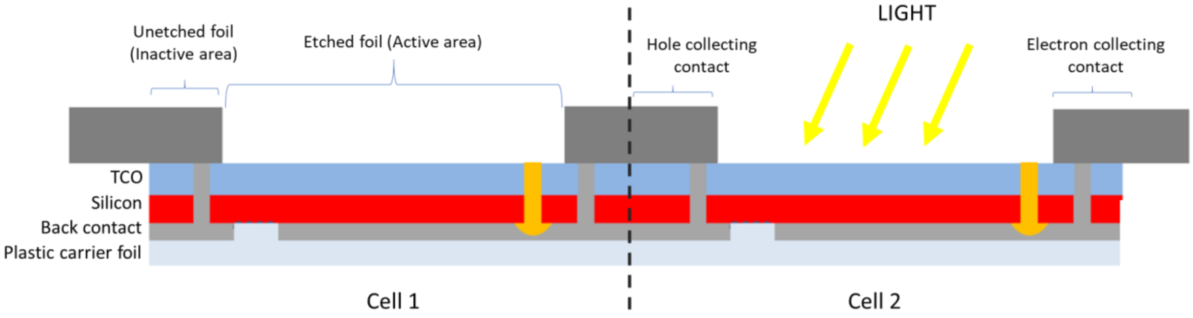

***Figure 82**: Cross-section of final solar cell stack showing two cells*

5.2.3 First Challenges encountered at HyET

The first nc-Si:H cells completed at HyET were not successful, mainly because the processes are optimized for a-Si:H solar cells. The J-V tests under non-illuminated conditions showed highly shunted behaviour. Possible reasons for the failure are discussed in detail below.

(i) The laser scribe settings need to be optimized for nc-Si:H. Higher laser powers are required to scribe through nc-Si:H compared to a-Si:H. It was not certain whether the laser scribes had completely etched through the layers as expected. The solution is to experiment with the laser settings and make EDS measurements to confirm whether the nc-Si:H has been scribed properly.

(ii) The Front TCO deposited at TU Delft is aluminium doped zinc oxide (AZO), whereas the TCO used at HyET is fluorine doped tin oxide (FTO). The FTO is used due to its chemically inert nature and can therefore withstand the final etching in NaOH. However, the AZO does not survive the etching with NaOH; this is problematic as once the aluminium is etched away, there is only a tiny window to remove the sample before the AZO and the nc-Si:H layers etch away completely as shown in Figure 83. This is impossible with the standard etching recipe (1.2M NaOH at 70°C) as the etching rate is too quick for human reaction. A solution would be to modify the etching recipe to a lower concentration and temperature with KOH such that the rate of reaction is slowed, this allows the AZO to be saved. However, extensive experiments would need to be done to determine the etching rate such that the experiments can be easily reproduced. TU Delft does not possess the equipment to deposit FTO, therefore, a solution is to use FTO deposited samples developed at HyET. The disadvantage of this is that these samples do not exhibit the better surface features of MST 4.

(iii) When the etching of HyET's a-Si:H cells are complete, a dark black colour can be observed as shown in Figure 81(c). This is not the same for nc-Si:H as the deposition is a steel-grey colour that is similar to the appearance of the Al foil. Given that the AZO is transparent and is also vulnerable to etching, it is difficult to know when exactly to stop the etching process. A solution is to do an etching series in parallel with SEM analysis to determine when exactly the Al is etched away. This would allow to preserve the AZO and nc-Si:H layers.

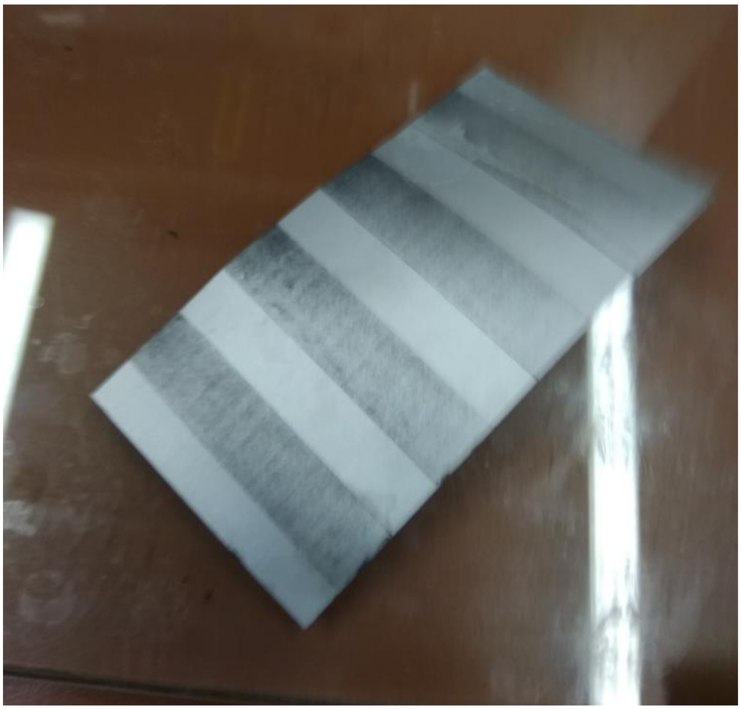

Figure 83*: The AZO does not survive the final etching step and the solar cell layers are also etched away within a matter of seconds.*

5.2.4 Further analysis of samples completed at HyET

A SEM analysis of the samples were undertaken. Figure 84 shows such a sample where the layers are labelled. The high quality nc-Si:H grown on MST surface can be observed with almost no visible cracks on the cross-section surface. It can also be observed that when the solar cell stack is transferred from the Al foil to the plastic carrier foil, the curvatures of the surface textures are maintained which is crucial for light trapping. The appearance of micro-textures at the back of the solar cell is crucial for scattering longer wavelengths that reach the back of the solar cell. In addition, no physical damage has occurred to the cell during the lamination, annealing and etching process. This proves that the concept of using MST on temporary Al foils does indeed work in practice. Furthermore, the lack of visible cracks indicates high quality nc-Si:H as supported earlier by high shunt resistance values. It is interesting to note that the Al foil is not completely etched away over the active area, this would explain why the dark J-V curves show highly shunted behaviour.

Several defects or artefacts can be observed in other cross-section images. One such as a high number of discontinuities as to what appear to be unused laser scribes that have may have become larger when exposed to etching solution as shown in Figure 85. These unused laser scribes may have been intended for filler ink which has not been properly deposited. Figure 86(a) shows a possible case where a too high laser power has been used and the filler ink has penetrated into the Al foil, whereas Figure 86(b) shows the case where a too low laser power is used and the filler ink has not penetrated the entire nc-Si:H and TCO layer.

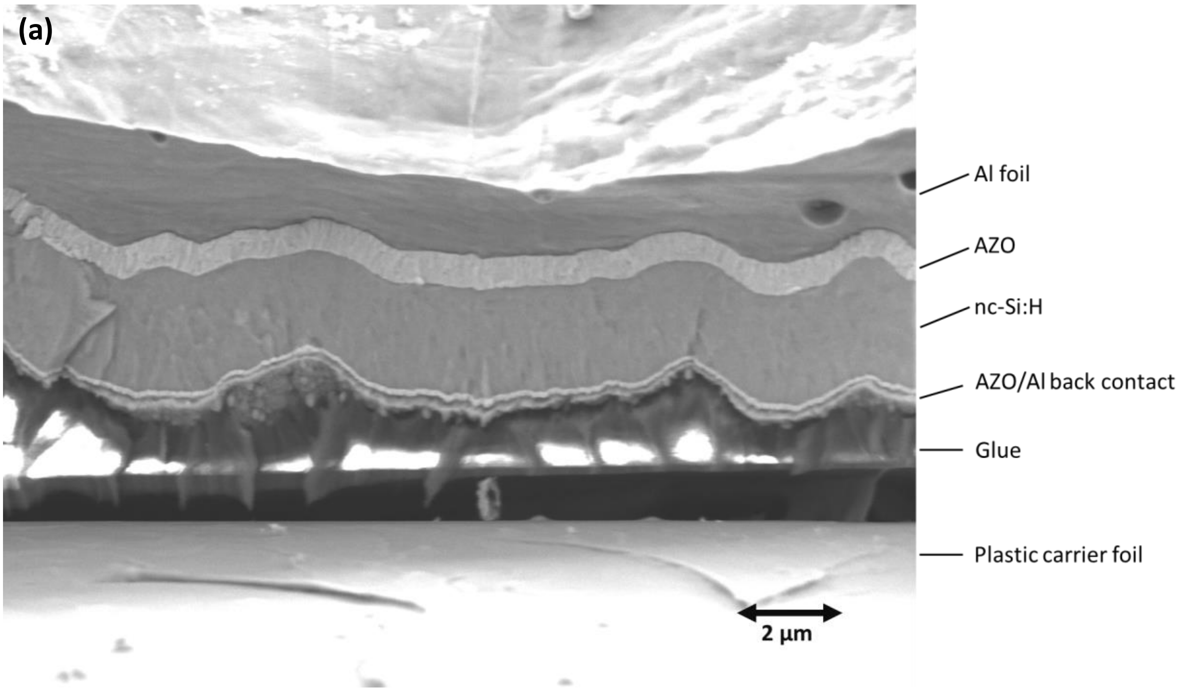
(a)
Al foil
AZO
nc-Si:H
AZO/Al back contact
Glue
Plastic carrier foil
2 µm

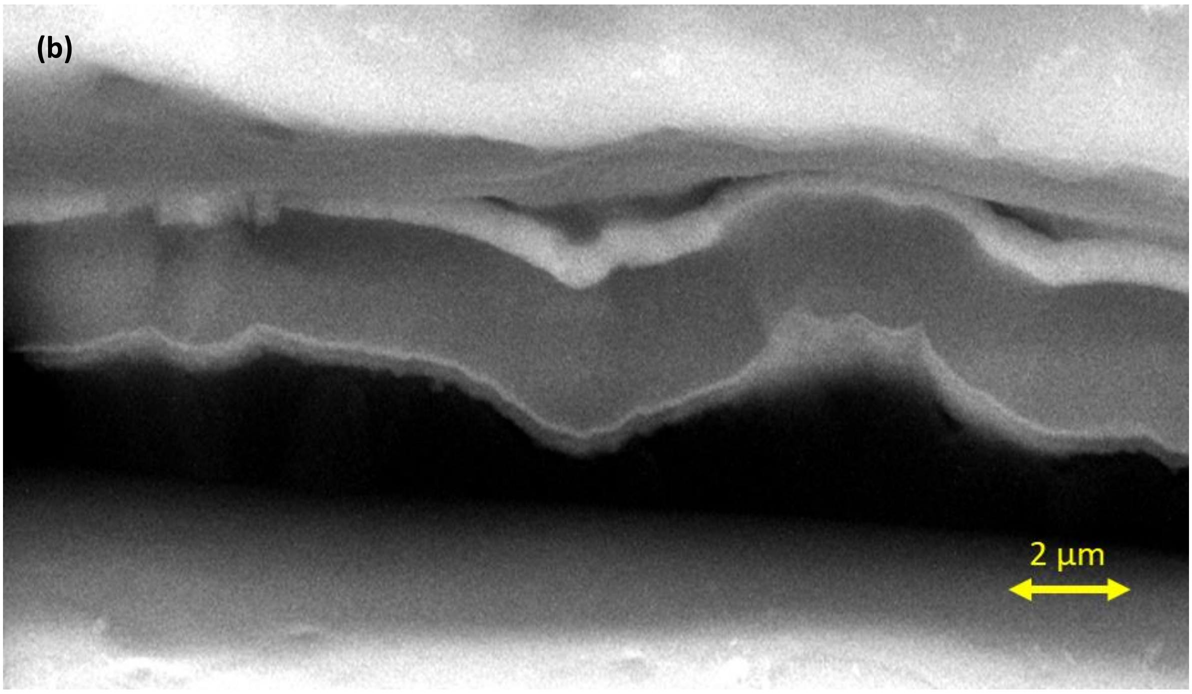
(b)
2 µm

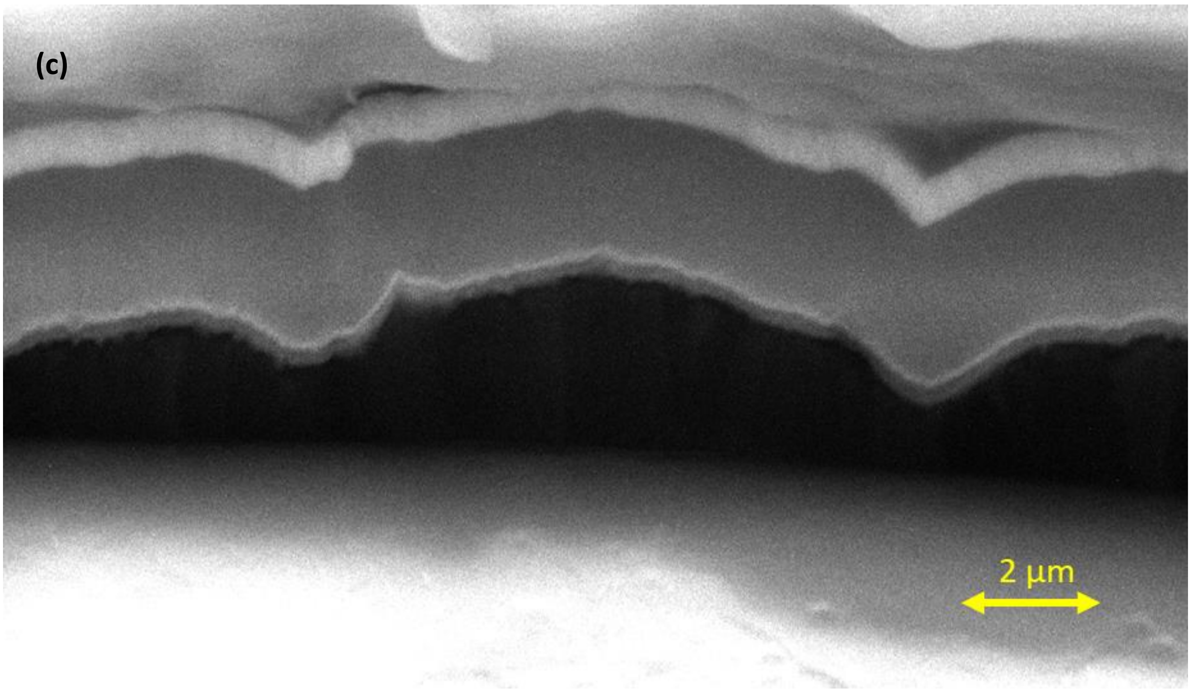

__Figure 84__: Cross sectional views of solar cell produced at HyET shows the micro-sized features of the substrate are preserved at the top and at the bottom layers of the cell.

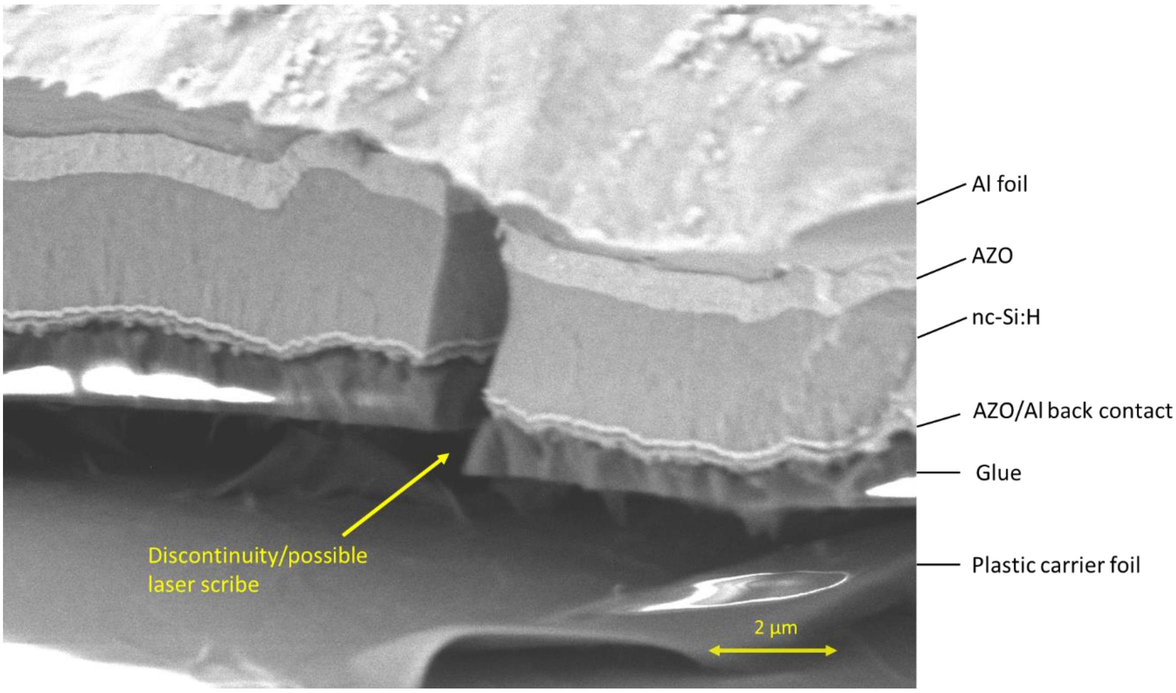

__Figure 85__: SEM image of discontinuity caused by unfilled laser scribes are observed, further deteriorated during etching.

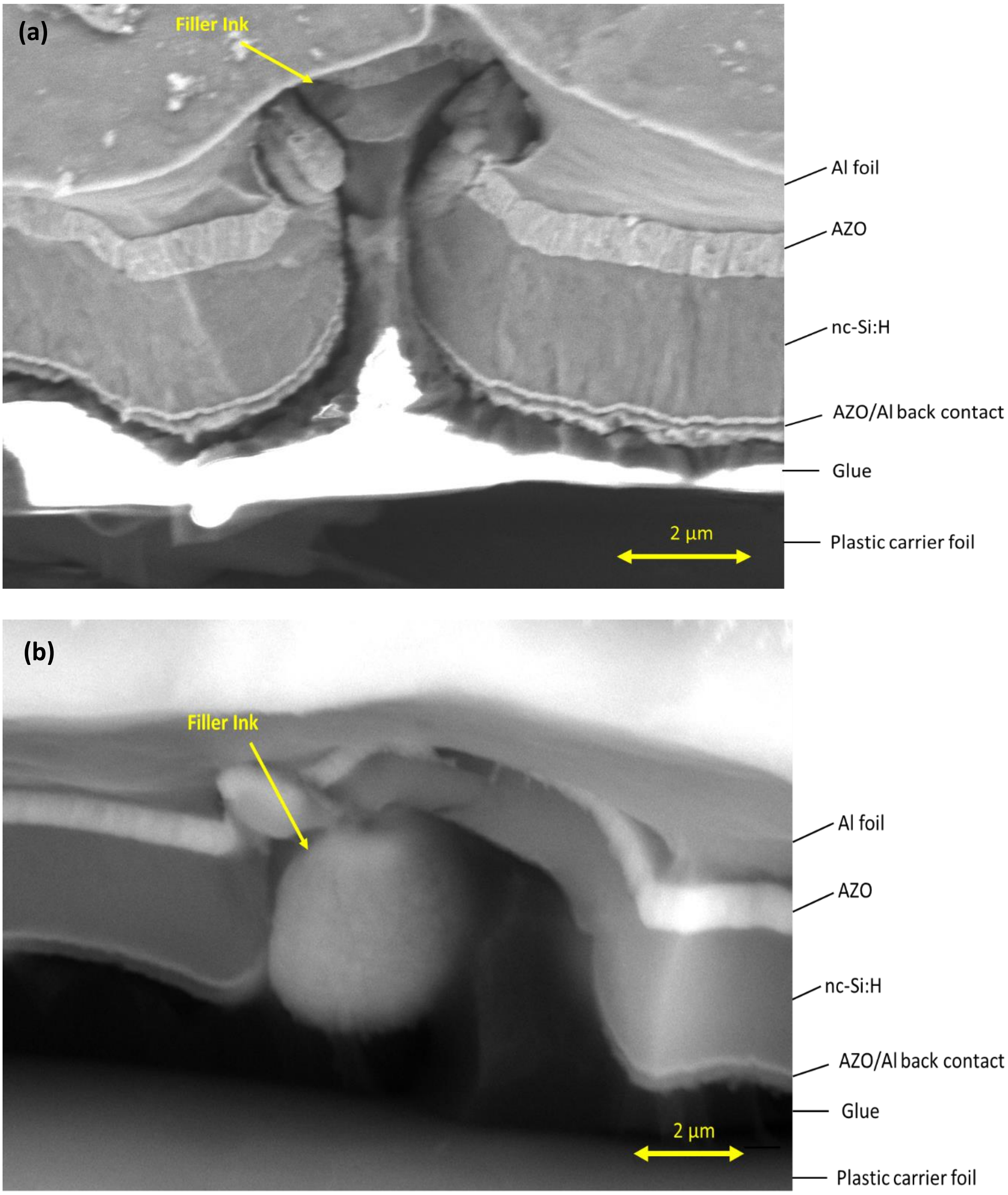

__Figure 86__: SEM images of the filler ink (a) Too high laser power used (b) Too low laser power used.

The same sample reveals that approximately 30µm of Al foil is remaining. An etching series is undertaken on the samples in order to etch away the remainder of Al. The etching is undertaken with 0.36M KOH (20g of KOH per 1000mL H_2O) at 35°C to slow down the etching rate as much as possible. The etching time is varied between 30 seconds and 3 minutes. It is quite difficult to determine the exact etching rate using SEM images at such small thicknesses, especially when the etching is not uniform. However, Figure 87(a) shows a SEM image of the same sample where all the Al is completely etched away. The naturally nano-textured surface of the AZO can be observed from the surface roughness. Figure 87(b) shows the sample corresponding to the same, it should be noted that the finished nc-Si:H cell shows a greyish colour contrary to the black colour of a-Si:H cell. This also proves that the AZO can indeed be preserved by etching at a very low rate. However, there is still uncertainty over the survivability of the AZO during the etching process with NaOH. Moreover, moving to KOH during the final etching requires more resources and time consumed, which is not favourable to HyET. Therefore, it is best to move forward with samples deposited with FTO developed at HyET.

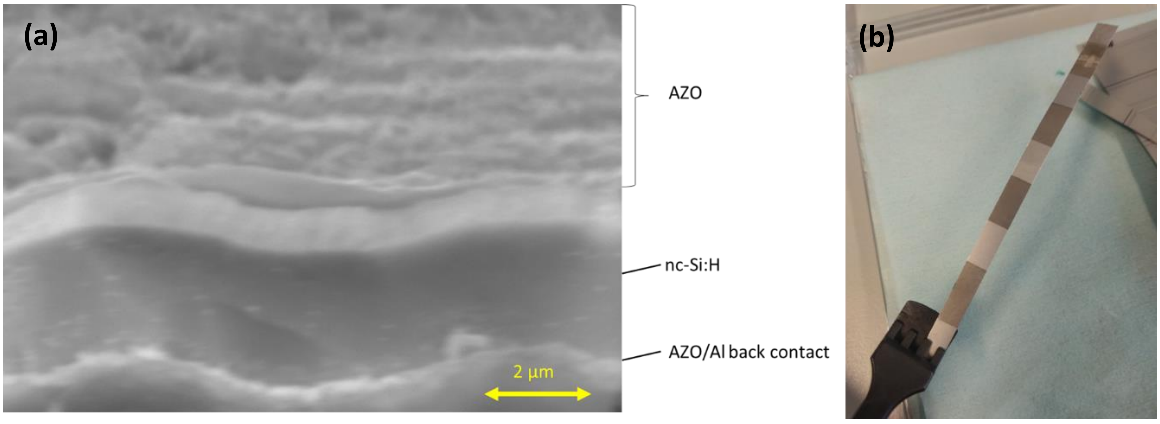

Figure 87: (a) SEM image of the cell after complete etching of the Al foil shows the surviving AZO and cell layers, (b) The sample appears to show a greyish colour compared to the black colour of the samples developed at HyET.

5.2.5 Alternate fabrication method at TU Delft

As explained in the previous chapter, the first experiments at HyET on nc-Si:H solar cells were not without its obstacles. HyET is still experiencing issues with its "LP3 interconnection tool" which is responsible for the laser scribing and filler ink deposition, moreover, the laser parameters were not optimized for nc-Si:H layers. The use of these tools is strictly limited to HyET staff only. The purpose of this section is to present an alternative way of fabricating the solar cell at TU Delft such that the solar cell can be tested under AM1.5G spectrum. The purpose of doing this is to provide an initial estimate of the efficiency using a fairly similar approach without relying too much on the processes at HyET. The process is described below.

1. The active layers are deposited on the Al foil using the PECVD tool.
2. A full area Al contact of 500 nm is evaporated. No laser scribing is performed as the entire area of the 10x10 cm^2 foil will serve as the active area.
3. A metal contact is soldered to the Al back contact and extended outward. This contact will serve as a contact point for the probe during J-V measurement.
4. The sample is laminated to the permanent carrier. Here, EVA and plastic foil is used as a substitute for the glue and carrier foil in HyET's process. During lamination, care must be taken to protect the extended contact.
5. The sample is then dipped in an etching solution to etch the Al foil.
6. The sample is placed under the WACOM. A mask is used to illuminate 1x1 cm^2 area of the cell. The TCO is used as the front contact and the extended metal is used at back contact.

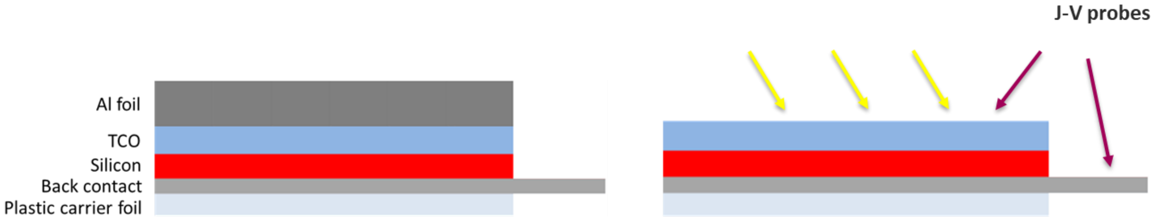

Figure 88: Schematic for alternate fabrication method and testing of solar cell.

5.2.6 First Challenges of alternate fabrication method

The experiments undertaken were not successful and the processes were faced with some challenges. However, there is a strong possibility to perfect this method in order to obtain working solar cells. The main constraint is time, as this new approach can form a master thesis project on its own. Some of the challenges are described below.

1. The metal contact cannot be easily soldered to the Al back contact of the cell using the normal soldering iron as the contact is not properly held in place. A solution would be to use ultrasonic soldering.
2. The lamination process and tools used at PVMD and HyET are different, though to what extent it is unclear. Some laminations undertaken at PVMD were successful whereas others resulted in air pockets (Figure 89) that were detrimental during the etching process. It is important to understand the processes and optimise the settings such that the outcome of the lamination at PVMD is fairly similar to HyET's, thus allowing results to be easily reproduced.
3. The etching rate of Al foil is difficult to understand without doing some extensive experiments. It is also difficult to understand when to stop the etching. As discussed earlier, the samples developed at TU Delft are deposited with AZO. The AZO etches away completely within a matter of seconds together with the active cell layers, thus rendering the sample obsolete. Again, a solution would be to use FTO deposited samples from HyET.

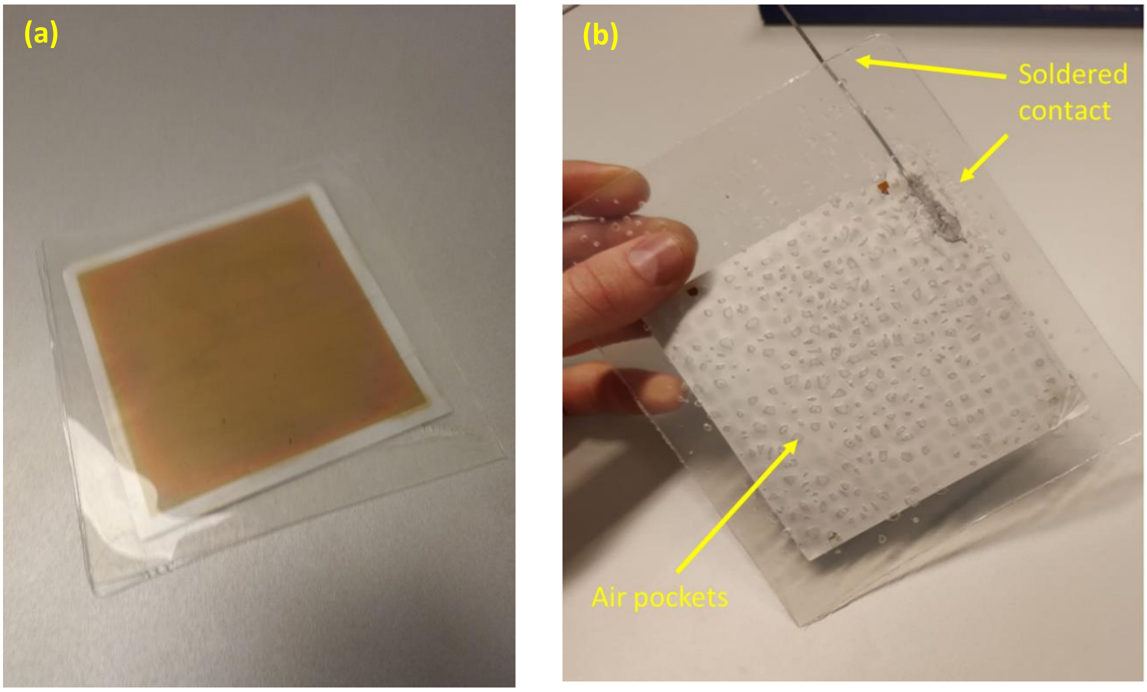

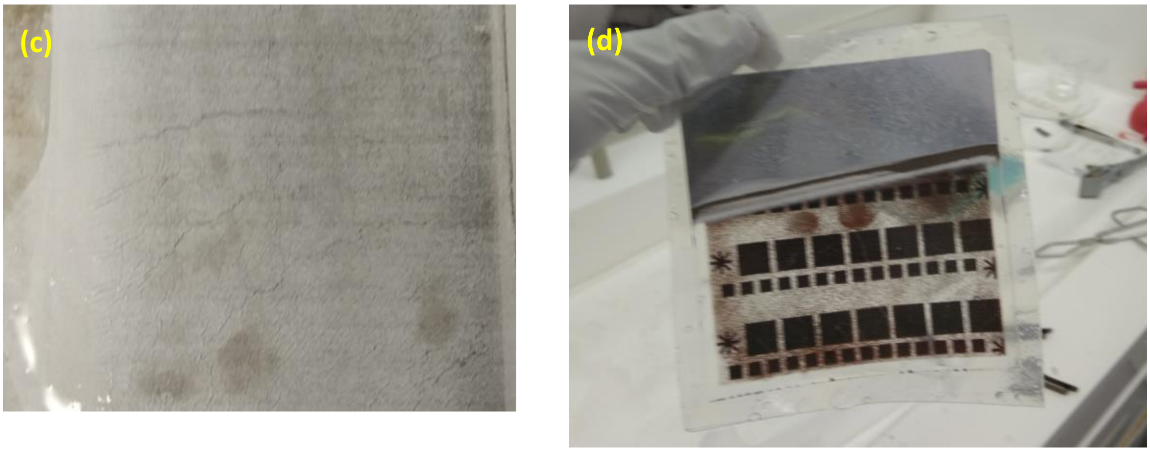

***Figure 89**: Images of alternate fabrication method developed at TU Delft (a) A case of successful lamination of the solar cell to the plastic foil, (b) Contact soldered and extended outward from the lamination, (c) Cracks appear at the back of the sample during etching even though this side is laminated, (d) Cell is completely etched within a matter of seconds once the Al foil is etched away.*

Despite these issues, we believe it can be overcome to produce working cells inhouse at PVMD. It is recommended that further research should be undertaken in this area to perfect alternate ways of producing this cell at TU Delft rather than completely depending on HyET's facilities and processes. However, further research into this area is not part of this thesis project.

6 Conclusions

Nanocrystalline silicon solar cells were successfully grown on flexible Al substrate at TU Delft for the first time. The concept of modulated surface textures was implemented to grow high quality nc-Si:H while maintaining good light trapping properties. The concept of growing nc-Si:H cells in substrate (n-i-p) configuration on permanent flat Al substrates is found in literature. However, the construction philosophy of using a flexible temporary Al substrate to deposit nc-Si:H in p-i-n superstrate form is a novel technique that is unique to HyET Solar. In this chapter the most important findings and results are summarised in line with aims of this thesis.

6.1 Applying the concept of modulated surface textures to Al foils

Substrate textures with large micro-sized craters were created using different etching recipes. The best surface features correspond to a correlation length of 4 µm, RMS roughness of 500 nm, and aspect ratio of 0.13. These features sizes are comparable to those of high efficiency solar cells employing MST on glass. Surface textures created by chemical etching should be done under controlled conditions, and deviations in temperature and etching time will create too small or too large features. Average thickness of the foil after etching is 80 µm. Thinner foils are also detrimental to later stages of the process when the substrate needs to be removed.

6.2 Factors influencing the growth of nc-Si:H material on Al foil using MST

A dependence of substrate features on crystallinity is observed. Substrates with smaller craters resulted in less crystalline material which indicates a thicker incubation layer, whereas substrates with larger craters resulted in highly crystalline material. It is important to decouple these effects when moving to a largescale roll to roll process where external factors such as temperature and concentration are prone to variation and can lead to changes in crystallinity.

By varying the silane concentration, it was found that a value between 2.72% and 2.95% yields device grade nc-Si:H as indicated by the signature of silicon-hydrogen ($Si-H_x$) or hydride stretching modes in Raman spectrum between 1800 cm^{-1} and 2300 cm^{-1}. By observing the spectrum, a signature for high-quality nc-Si:H (mix phase of nanocrystalline and amorphous) could be identified. Furthermore, a signature for highly amorphous and highly crystalline (but defective) material could also be distinguished. The depositions also exhibit non-homogeneity in material growth. Deposition rates of up to 0.49 nm/s were measured in the optimum silane concentration range, this rate is similar to that on glass substrates.

When compared to nc-Si:H grown on glass substrates, there is an inconstancy of crystalline fraction with silane concentration. Furthermore, very high crystallinities are obtained on Al substrate compared to glass substrate over a wider range of silane concentration. This suggests that the optimum deposition parameter window on Al substrates may be more forgiving than that of glass, and it also suggests some catalytic nature of the Al substrate on crystallisation.

A thickness series undertaken with optimum silane concentration indicated that thicknesses of 1.5 µm and 2 µm yield highly amorphous layers whereas at 3 µm shows good characteristics. This indicated that the standard seed layer used on glass is not conducive to create nc-Si:H material from the onset of growth.

6.3 Growth and characterisation of high quality nc-Si:H material on Al foil

The seed layer plays an important role in providing a good p-i interface and decoupling any strong substrate influences on the microstructure of nc-Si:H intrinsic layer. For MST on Al substrate, the standard seed layer used on glass cannot achieve this result. Even though the seed layer is highly crystalline, its hydride SM signature reflects a poorly passivated layer with increased contribution of di- and tri-hydrides in the bulk as well as hydrogenated grain boundaries. This type of seed layer is defective and can cause hole collection losses at the p-i interface. This is detrimental to solar cell performance.

A technique called silane concentration grading is applied to the seed layer, the hydrogen and silane flows in the PECVD chamber are varied to drive the silane concentration from a low value to the desired final value during a time of 500 seconds. This technique yields highly crystalline layers that exhibit very good hydride SM signatures within the first 100 nm of deposition. This signature is reflective of dense material which is well passivated with amorphous tissue and without hydrogenated grain boundaries. The seed layers show good thickness homogeneity and reproducibility. The best seed layers are obtained using an initial silane concentration that is 20% of the final value. It should be noted that this initial value is substrate dependent and may need to be tuned for changes in underlying layers such as substrate textures, TCO and p-layer thickness.

Consequently, these seed layers are applied to grow thick i-layers which can be used in solar cell applications. The i-layers show good thickness homogeneity in the growth direction in terms of crystalline fraction and stretching mode signatures. Graded seed layers also enhance the preferential growth orientation of the nanocrystalline grains in the (220) plane compared to (111) plane. This indicates that graded seed layers favour thermodynamically preferred grain growth rather than random nucleation which leads to defect rich crystalline grains characterized by (111) plane. The opposite is observed for ungraded seed layers where crystallites favour the (111) plane. It can be concluded that graded seed layers can:

1. Decouple substrate effects in the MST and other underlying layers.
2. Provides a smooth transition of microstructure at the p-i interface and yields device grade material with high crystallinities from onset of growth.
3. Improves the microstructure homogeneity of the i-layer in the growth direction.
4. Favours high crystallinities and device grade material properties independent of the silane concentration over a wider range of values compared to ungraded seed layers.
5. Expect to show increased performance of the solar cell in terms of $V_{oc,}$ J_{sc} and FF.

It is found that crystalline fraction varies irregularly with increased silane concentration on the Al substrates when using either graded or ungraded seed layers. This is unlike on glass substrate where a strong dependence exists and a clear decreasing trend of crystalline fraction with increased silane concentration can be observed. The high crystallinities are suited to high efficiency solar cells and more importantly for tandem solar cells, where the red wavelength response of the bottom nc-Si:H should be maximised. As discussed, this may be advantageous to the roll to roll processing as the deposition parameter window on Al substrates may be less narrow compared to glass.

In addition to SEM images showing no cracks using graded seed layers, dark J-V measurements undertaken at HyET showed good results. Shunt resistance values of nc-Si:H cells were orders of magnitude higher than that of a-Si:H cells produced at EKL and at HyET. The closeness of shunt resistance values spread over the area of the cell indicates good homogeneity in the quality of the deposited layers. This can be attributed to the use of MST and graded seed layers used to grow high quality nc-Si:H with limited cracks and defects in the bulk material.

Optical simulations show that when solar cell layers adopt the surface morphology of micro-sized craters at the front and back of the solar cell, an increase in the implied photocurrent can be observed. This is mainly due to increased scattering in the 700 nm to 1200 nm. For 3 µm i-layer cells modelled with HyET's encapsulation, back contact, and best MST features an implied photocurrent of 27.07 mA/cm^2 is achieved with Al back contact and 28.27 mA/cm^2 is achieved with Ag back contact. Further improvements can be made by optimizing the MST, transparency of the p-layer and thicknesses of individual layers. The use of GenPro4 is not completely applicable for simulating MST since the ray and wave model are mutually exclusive to micro- and nano-sized features respectively. The ray model is a reasonable approximation to MST; however, more validation needs to be done by comparing results with that of real solar cells.

6.4 Fabrication of nc-Si:H solar cells at HyET Solar

The solar cells were successfully laminated onto the permanent plastic carrier foil. The resulting cell showed that the active layers follow the shape of the MST at the front and the back of the cell. In addition, no cracks or physical damage is observed in the nc-Si:H layers. These two characteristics prove that the concept of MST can be applied on Al substrates using HyET's unique construction method.

Some challenges were faced when completing the 1x5 cm^2 cells at HyET Solar, this is mainly due to inexperience with nc-Si:H cells since processes have been optimized for a-Si:H cells. Initial experiments resulted in highly shunted cells. Further analysis at TU Delft showed that this is because the Al substrate was not completely etched away, as it was unclear when to stop the etching process. A few shortcomings of the laser scribing system at HyET were identified. The laser settings need to be optimised due to different material properties and thickness of nc-Si:H compared to the a-Si:H. The appearance of the completed nc-Si:H cells appear to be grey in colour compared to the black colour of a-Si:H cells. It was found that the AZO does not survive the final etching of the Al substrate as it reacts too quickly with the etching solution. It was therefore recommended that cells with FTO as front TCO should be used for further experiments. The foils containing FTO produced at HyET however, only exhibit surface features of new factory pre-treatment and not the best textures developed at TU Delft. Therefore, the V_{oc} and FF of the final cells will be limited.

6.5 Characterising solar cells under illuminated conditions

The illuminated performance of the cells is not measured in this thesis project due to bottlenecks explained in section 6.4. It is unclear how much time HyET Solar would take to iron out issues with regards to their internal processes which are optimised for the a-Si:H modules. Not to mention that HyET Solar has its own priorities within the company, however, this does not mean that they have not given us their utmost support throughout the project. PVMD is not privy to the processes at HyET Solar and therefore, this is out of our control. This dilemma provides additional reasoning to implement a new fabrication method within TU Delft itself.

An alternate fabrication method was explored at TU Delft to complete the cells without depending on the cumbersome and delayed processes at HyET Solar. The first attempt was unsuccessful due to issues with lamination and etching. However, we are confident that with further research and dedication, a more successful approach can be developed.

7 Recommendations

In this final chapter, some interesting areas for future research is proposed. These are both extensions of the work carried out under the thesis, as well as novel processing techniques for nc-Si:H solar cells found in literature.

7.1 Buffer layer between p-i interface

In high efficiency nc-Si:H solar cells over 11%, an amorphous buffer layer is added between the p-layer and a highly crystalline i-layer with crystalline fractions of above 80%. The use of the buffer layer is to passivate the highly crystalline i-layer and p-nc-SiO_x:H layer. This leads to an improvement in V_{oc} [56]. The use of the buffer layer is less important in tandem solar cells, where top cell can contribute to the V_{oc} while the bottom cell contributes to red wavelength response. It is recommended that a buffer layer should be optimized for single junction nc-Si:H to improve performance.

7.2 S_c grading in the main i-layer

Another possibility is to undertake silane concentration grading within the main i-layer. In this thesis, S_c grading was applied only to the graded seed layer, however in high efficiency solar cells, this technique has been applied to the main i-layer as well [57]. This allows better controllability of the crystallinity. It is found that using graded seed layers, the crystallinity towards the end of the deposition is slightly lower compared to the bulk of the material. S_c grading can be used to ensure crystallinity is homogenous throughout the layer.

7.3 Further tuning of seed layer and possible influence of i-n interface

Further experiments would need to be undertaken to better understand the growth of the seed layer and its sensitivity to the gradient of the grading, i.e. in terms of $S_{c,\,Initial}$, $S_{c,\,Final}$ and deposition time. As suggested in section 5.1.12, slightly overshooting the final S_c in the graded seed may have a positive influence in main i-layer growth. These parameters are also sensitive to some external parameters such as substrate textures and different TCO such as FTO or AZO, which could be a reason why some results could not be perfectly reproduced. The effects of the graded seed layer on the preferred orientation growth of crystallites should be understood more since it seems to prefer the (220) plane rather than the (111) plane.

It is a possibility to also apply S_c grading to the i-n interface, although not much weight is given to this interface due to the superior mobility of electrons. However, it is still interesting to understand the effect of a good i-n interface on the performance of the solar cell.

7.4 Possible high-efficiency nc-Si:H cells

The p-i-n cells deposited using graded seed layers with $S_{c,\,Final} = 2.95\%$ (H_2 flow = 115 sccm and SiH_4 = 3.5 sccm) show great promise. These cells exhibit good thickness homogeneity with respect to crystalline fraction and hydride mode signatures in the extended range. High crystallinities in excess of 70% were obtained. In addition, they also had the highest ratio of XRD intensity of $I_{(220)}/I_{(111)} = 1.35$, which shows a favourable (220) planar orientation for crystallites. According to the theory, taking into account all the above, the solar cells should demonstrate high V_{oc}, J_{sc} and FF, thus leading to high efficiency nc-Si:H single junction solar cells.

7.5 Thickness series and optimization of other layers

Once the cell fabrication is successful and the efficiency has been optimized for a baseline thickness of 2.3 µm, it is recommended to undertake a thickness series to see how the V_{oc}, J_{sc}, FF and η behaves. This should allow us to obtain the thickness at which the efficiency is maximized for a certain set of deposition conditions. Further improvements are possible by optimizing the thickness of the p and n-layers, as well as the TCO and back contact layers for nc-Si:H to achieve the best compromise between optical and electrical properties.

7.6 An alternate path to completing solar cells at TU Delft

Several challenges were met whilst competing the cells at HyET Solar. These challenges are out of the control of PVMD students and sometimes HyET staff. For these reasons it is highly recommended that an alternative path of completing the cells is researched at TU Delft. Initial attempts on this so far has shown that is possible to implement a method that is similar to HyET's methodology such that fairly similar results can be obtained. The FlamingoPV project is far from complete and implementing an alternate method at TU Delft would bring added value.

Bibliography

[1] Solar Power Europe, "Global Market Outlook for Solar Power / 2018-2022," 2018. [Online]. Available: https://www.solarpowereurope.org/wp-content/uploads/2019/07/SolarPower-Europe_Global-Market-Outlook-2019-2023.pdf.

[2] International Renewable Energy Agency, "FUTURE OF SOLAR PHOTOVOLTAIC Deployment, investment, technology, grid integration and socio-economic aspects," 2019. [Online]. Available: https://www.irena.org/publications/2019/Nov/Future-of-Solar-Photovoltaic.

[3] Fraunhofer ISE, "Photovoltaics Report," 2019. [Online]. Available: https://www.ise.fraunhofer.de/content/dam/ise/de/documents/publications/studies/Photovoltaics-Report.pdf.

[4] T. D.Leea and A. U.Ebong, "A review of thin film solar cell technologies and challenges," *Renewable and Sustainable Energy Reviews,* vol. 70, pp. 1286 - 1297, 2017, doi: https://doi.org/10.1016/j.rser.2016.12.028.

[5] CED Greentech. Thin Film vs. Crystalline Silicon PV Modules [Online] Available: https://www.civicsolar.com/article/thin-film-vs-crystalline-silicon-pv-modules (Accessed March 2020).

[6] A. Shah, *Thin-film Silicon Solar Cells*. EPFL Press, 2010.

[7] A. Smets, Jäger, K. et al., *Solar energy, The physics and engineering of photovoltaic conversion, technologies and systems*. UIT Cambridge Ltd, 2016.

[8] M. A. Green, E. D. Dunlop, D. H. Levi, J. Hohl-Ebinger, M. Yoshita, and A. W. Y. Ho-Baillie, "Solar cell efficiency tables (version 54)," *Progress in Photovoltaics: Research and Applications,* vol. 27, no. 7, pp. 565-575, 2019, doi: 10.1002/pip.3171.

[9] M. Nakamura, K. Yamaguchi, Y. Kimoto, Y. Yasaki, T. Kato, and H. Sugimoto, "Cd-Free Cu(In,Ga)(Se,S)2 Thin-Film Solar Cell With Record Efficiency of 23.35%," *IEEE JOURNAL OF PHOTOVOLTAICS,* vol. 9, no. 6, 2019.

[10] TU Delft. Thin-film Si PV technology [Online] Available: edx.org (Accessed March 2019).

[11] A. Smets, "Flexible Lightweight Advanced Materials In Next Generation Of PV: FlamingoPV," T U Delft, 2018.

[12] M. N. Donker *et al.*, "Flexible amorphous and microcrystalline silicon tandem solar modules in the temporary superstrate concept," *Solar Energy Materials and Solar Cells,* vol. 91, pp. 572-580, 2007, doi: 10.1016/j.solmat.2006.11.012.

[13] Clean Technica. Hyet Solar Plans €200 Million Solar Fab In India [Online] Available: https://cleantechnica.com/2017/12/25/hyet-solar-plans-e200-million-solar-fab-india/ (Accessed April 2020).

[14] K. Jäger and E. Hamers, "Large-Area Production of Highly Efficient Flexible Light-Weight Thin-Film Silicon PV Modules," presented at the 28th European Photovoltaic Solar Energy Conference and Exhibition, 2013.

[15] HyET Solar, "LP3 interconnection process," ed, 2019.

[16] C. H. Tsai, "Characterization and Fabrication of Thin-Film Microcrystalline Silicon," ed, 2018.

[17] A. Gordijn, "Microcrystalline Silicon for Thin-Film Solar Cells," PhD, Faculty of Physics & Astronomy, University of Utrecht, Netherlands, 2005.

[18] S. N. Agbo, "Growth and Characterization of Thin Film Nanocrystalline Silicon Materials and Solar Cells," PhD, Electrical sustainable energy, T U Delft, 2012.

[19] KenjiYamamoto, AkihikoNakajima, and MasashiYoshimi, "A high efficiency thin film silicon solar cell and module," *Solar Energy,* vol. 77, no. 6, pp. 939 - 949, 2004, doi: https://doi.org/10.1016/j.solener.2004.08.028.

[20] H.Takakura and Y.Hamakawa, "Device simulation and modeling of microcrystalline silicon solar cells," *Solar Energy Materials and Solar Cells,* vol. 74, no. 1, pp. 479 - 487, 2002, doi: https://doi.org/10.1016/S0927-0248(02)00108-3.

[21] S. Hitoshi *et al.*, "High-efficiency microcrystalline silicon solar cells on honeycomb textured substrates grown with high-rate VHF plasma-enhanced chemical vapor deposition," *Japanese Journal of Applied Physics,* vol. 54, 2015.

[22] H. Tan *et al.*, "Highly transparent modulated surface textured front electrodes for high-efficiency multijunction thin-film silicon solar cells," *Progress in Photovoltaics: Research and Applications,* vol. 23, no. 8, pp. 949-963, 2015, doi: 10.1002/pip.2639.

[23] M. Goetz *et al.*, "N-I-P Micromorph Solar Cells on Aluminium Substrates," *MRS Proceedings,* vol. 452, 2011, doi: 10.1557/PROC-452-877.

[24] J. Bailat, E. Vallat-Sauvain, L. Feitknecht, C. Droz, and A. Shah, "Influence of substrate on the microstructure of microcrystalline silicon layers and cells," *Journal of Non-Crystalline Solids,* vol. 299-302, pp. 1219 - 1223, 2002, doi: https://doi.org/10.1016/S0022-3093(01)01142-5.

[25] M. Python, D. Dominé, T. Söderström, F. Meillaud, and C. Ballif, "Microcrystalline silicon solar cells: effect of substrate temperature on cracks and their role in post-oxidation," *Progress in Photovoltaics: Research and Applications,* vol. 18, no. 7, pp. 491-499, 2010, doi: 10.1002/pip.956.

[26] O. Isabella, J. Krc, and M. Zeman, "Modulated surface textures for enhanced light trapping in thin-film silicon solar cells," *Applied Physics Letters,* vol. 97, 2010, doi: 10.1063/1.3488023.

[27] T. Matsui, M. Tsukiji, H. Saika, T. Toyama, and H. Okamoto, "Influence of substrate texture on microstructure and photovoltaic performances of thin film polycrystalline silicon solar cells," *Journal of Non-Crystalline Solids,* vol. 299, pp. 1152-1156, 2002, doi: 10.1016/S0022-3093(01)01083-3.

[28] P. M. Martin, *Handbook of Deposition Technologies for Films and Coatings 3rd Edition*. William Andrew, 2010.

[29] A. Smets, "PV Technologies," in *ET4377 PV technologies Selection of slides on thin-film PV technologies*, ed: TU Delft, 2019.

[30] P. Mondal and D. Das, "Preferential 〈220〉 crystalline growth in nanocrystalline silicon films from 27.12 MHz SiH4 plasma for applications in solar cells," *RCS Advances,* 2015. [Online]. Available: http://dx.doi.org/10.1039/C5RA07781H.

[31] A. Bleakie and D. Djurdjanovic, "Dynamic Feature Monitoring Technique Applied to Thin Film Deposition Processes in an Industrial PECVD Tool," *ASME 2011 International Manufacturing Science and Engineering Conference, MSEC 2011,* vol. 2, 2011, doi: 10.1115/MSEC2011-50041.

[32] SEMICORE Equipment Inc. What is RF Sputtering? [Online] Available: http://www.semicore.com/news/92-what-is-rf-sputtering (Accessed January, 2020).

[33] Laboratoire Charles Coulomb Montpelier. RF magnetron sputtering [Online] Available: https://coulomb.umontpellier.fr/RF-magnetron-sputtering?lang=fr (Accessed February 2020).

[34] Angstrom Engineering. Aluminium Evaporation [Online] Available: https://angstromengineering.com/tech/resistive-thermal-evaporation/aluminum-evaporation/ (Accessed January 2020).

[35] SEMICORE Equipment Inc. What is Thin Film Deposition By Thermal Evaporation? [Online] Available: http://www.semicore.com/news/71-thin-film-deposition-thermal-evaporation (Accessed January, 2020).

[36] C. Smit, R. A. C. M. M. van Swaaij, H. Donker, A. M. H. N. Petit, W. M. M. Kessels, and M. C. M. van de Sanden, "Determining the material structure of microcrystalline silicon from Raman spectra," *Journal of Applied Physics,* vol. 94, no. 5, pp. 3582-3588, 2003, doi: 10.1063/1.1596364.

[37] C. Droz, "Thin film microcrystalline silicon layers and solar cells : microstructure and electrical performances," 2003.

[38] A. H. M. Smets, T. Matsui, and M. Kondo, "Infrared analysis of the bulk silicon-hydrogen bonds as an optimization tool for high-rate deposition of microcrystalline silicon solar cells," *Applied Physics Letters,* vol. 92, no. 3, p. 033506, 2008, doi: 10.1063/1.2837536.

[39] Newport Corporation. Integrating Sphere Fundamentals and Applications [Online] Available: https://www.newport.com/t/integrating-sphere-fundamentals-and-applications (Accessed February 2020).

[40] Park Systems. How AFM Works [Online] Available: https://parksystems.com/medias/nano-academy/how-afm-works (Accessed February 2020).

[41] M. Bloomfield, "Roughness Concepts," 2006. [Online]. Available: http://homepages.rpi.edu/~bloomm2/roughness.pdf.

[42] C. Woodford. Electron microscopes [Online] Available: https://www.explainthatstuff.com/electronmicroscopes.html (Accessed February 2020).

[43] S. K.Rama, SatyendraKumara, and P. R. i. Cabarrocas, "Role of microstructure in electronic transport behavior of highly crystallized undoped microcrystalline Si Films," *Thin Solid Films,* vol. 515, no. 19, pp. 7469 - 7474, 2007, doi: https://doi.org/10.1016/j.tsf.2007.01.003.

[44] D. Rajagopal, "Al texturing highlights No.2," in "Flamingo Progress," TU Delft, 2020.

[45] D. Rajagopal, "Al texturing highlights No. 6," in "Flamingo Progress " TU Delft, 2020.

[46] D. Rajagopal, "Achieving Modulated Surface Texturing on temporary aluminium substrate for flexible thin-film solar cells," in "Flamingo Progress Mid term," TU Delft, 2020.

[47] D. Rajagopal, "Modulated Surface Texuring for Flexible Thin-Film Solar Cells," in "Flamingo Progress " TU Delft, 2020.

[48] D. Rajagopal, "Al texturing highlights No. 10," in "Flamingo Progress," TU Delft, 2020.

[49] O. Vetterl, M. Hülsbeck, J. Wolff, R. Carius, and F. Finger, "Preparation of microcrystalline silicon seed layers with defined structural properties," *Thin Solid Films,* no. 427, pp. 46-50, 2002.

[50] P. Bellanger *et al.*, "Crystalline silicon growth on aluminum substrate for photovoltaic application," *physica status solidi c,* vol. 14, no. 10, p. 1700173, 2017, doi: 10.1002/pssc.201700173.

[51] Y. Yuan, W. Zhao, J. Ma, Z. Yang, and W. Li, "Structural evolution of nanocrystalline silicon in hydrogenated nanocrystalline silicon solar cells," *Surface and Coatings Technology,* vol. 320, 2016, doi: 10.1016/j.surfcoat.2016.12.028.

[52] Y.-M. Li, L. Li, J. A. A. Selvan, A. E. Delahoy, and R. A. Levy, "Effects of seeding methods on the fabrication of microcrystalline silicon solar cells using radio frequency plasma enhanced chemical vapor deposition," *Thin Solid Films,* vol. 483, no. 1, pp. 84-88, 2005/07/01/ 2005, doi: https://doi.org/10.1016/j.tsf.2004.12.029.

[53] E. Johnson, L. Kroely, M. Moreno, and P. Cabarrocas, "Characterization of Microcrystalline Silicon by High Wavenumber Raman Scattering," *MRS Proceedings,* vol. 1153, 2009, doi: 10.1557/PROC-1153-A16-06.

[54] M. Python *et al.*, "Relation between substrate surface morphology and microcrystalline silicon solar cell performance," *Journal of Non-Crystalline Solids,* vol. 354, no. 19, pp. 2258 - 2262, 2008, doi: https://doi.org/10.1016/j.jnoncrysol.2007.09.084.

[55] R. Urbasolar *et al.*, "Window layer with p doped silicon oxide for high Voc thin-film silicon n-i-p solar cells," *Journal of Applied Physics,* vol. 110, 2011, doi: 10.1063/1.3669389.

[56] H. Sai, T. Matsui, K. Matsubara, M. Kondo, and I. Yoshida, "11.0%-Efficient Thin-Film Microcrystalline Silicon Solar Cells With Honeycomb Textured Substrates," *IEEE Journal of Photovoltaics,* vol. 4, p. 1349, 2014.

[57] S. Hänni *et al.*, "High-efficiency microcrystalline silicon single-junction solar cells," *Progress in Photovoltaics Research and Applications,* vol. 21, pp. 821-826, 2013, doi: 10.1002/pip.2398.